

## **General Disclaimer**

### **One or more of the Following Statements may affect this Document**

- This document has been reproduced from the best copy furnished by the organizational source. It is being released in the interest of making available as much information as possible.
- This document may contain data, which exceeds the sheet parameters. It was furnished in this condition by the organizational source and is the best copy available.
- This document may contain tone-on-tone or color graphs, charts and/or pictures, which have been reproduced in black and white.
- This document is paginated as submitted by the original source.
- Portions of this document are not fully legible due to the historical nature of some of the material. However, it is the best reproduction available from the original submission.

(NASA-CR-175334) ROTATIONAL CARS  
APPLICATION TO SIMULTANEOUS AND  
MULTIPLE-POINT TEMPERATURE AND CONCENTRATION  
DETERMINATION IN A TURBULENT FLOW Final  
Report, 1 Mar. 1980 - 28 (Yale Univ., New

N84-16489

Unclassified  
G3/34 15302

for the period

March 1, 1980 - February 28, 1983

John F. Dray, Robert V. Morris, and Richard A. Sorenson

Yale University  
Section of Applied Physics, 60 Old Campus Road  
New Haven, Connecticut 06520

**Final Report**

**Submitted to the**

**National Aeronautics and Space Administration**

**ROTATIONAL CARS APPLICATION TO SIMULTANEOUS AND MULTIPLE-POINT  
TEMPERATURE AND CONCENTRATION DETERMINATION IN A TURBULENT FLOW**

**NASA Grant No. NAG1-37**

**for the period**

**March 1, 1980 - February 28, 1983**

**by**

**Judith B. Snow, Daniel V. Murphy, and Richard K. Chang**

**Yale University  
Section of Applied Physics and Center for Laser Diagnostics  
New Haven, Connecticut 06520**

## TABLE OF CONTENTS

	Page
<b>Abstract</b>	<b>1</b>
<b>1. Introduction</b>	<b>1</b>
<b>2. Three-Dimensional Phase Matching</b>	<b>19</b>
<b>3. Experimental Implementation of Broadband CARS</b>	<b>26</b>
<b>4. Calculation of Rotational CARS Spectra and Intensity Distributions</b>	<b>49</b>
<b>5. Experimental Results</b>	<b>63</b>
<b>6. Phase-Matching for Multipoint CARS</b>	<b>106</b>
<b>7. Experimental Design and Implementation of Multipoint CARS</b>	<b>112</b>
<b>8. Experimental Results for Single-Shot Multipoint CARS</b>	<b>126</b>
<b>9. Conclusion</b>	<b>142</b>
<b>10. List of Symbols</b>	<b>146</b>
<b>11. References</b>	<b>149</b>

## ABSTRACT

Coherent anti-Stokes Raman scattering (CARS) from the pure rotational Raman lines of  $N_2$  is employed to measure the instantaneous ( $\sim 10$  ns) rotational temperature of  $N_2$  gas at room temperature and below with good spatial resolution ( $0.2 \times 0.2 \times 3.0$  mm $^3$ ). A broad-bandwidth dye laser is used to obtain the entire rotational spectrum from a single laser pulse; the CARS signal is then dispersed by a spectrograph and recorded on an optical multichannel analyzer. A best-fit temperature is found in several seconds with the aid of a computer for each experimental spectrum by a least squares comparison with calculated spectra. The model used to calculate the theoretical spectra incorporates the temperature and pressure dependence of the pressure-broadened rotational Raman lines, includes the nonresonant background susceptibility, and assumes that the pump laser has a finite linewidth. Temperatures are fit to experimental spectra recorded over the temperature range of 135 to 296 K, and over the pressure range of .13 to 15.3 atm. Emphasis is placed on the quantitative evaluation of single-pulse rotational CARS as a temperature measurement technique. The simultaneous measurement of temperature and pressure (or concentration) from a single laser pulse cannot be done straightforwardly. It is necessary to know the gas temperature in order to deduce the pressure. A possible solution is the use of an iterative technique which derives the parameters from an initial estimate. We have investigated the feasibility of determining temperature in a flame from the pure rotational spectrum of  $N_2$  using CARS. Although the CARS

signal generated at flame temperatures is quite weak compared to that produced at room temperature, our results indicate that it may provide an attractive alternative to the widely used vibrational CARS technique.

In addition to the spatially resolved single point work, we have used multipoint CARS to obtain information from many spatially resolved volume elements along a cylindrical line ( $0.1 \times 0.1 \times 2.0 \text{ mm}^3$ ). For this case, a large-angle, phase-matching geometry was used in which the dye laser probe beam and one of the pump beams intersect a sheet of pump radiation at an angle of  $90^\circ$ . The CARS signal is dispersed by a spectrograph and detected by the vidicon in such a way that spectral information is obtained in one dimension and spatial information in the other. The CARS signal generated in this manner is extremely weak since the CARS intensity is proportional to the square of the interaction length, which is  $0.1 \text{ mm}$  in the large-angle case as compared to  $3 \text{ mm}$  in the small-angle geometry. By using an image intensifier with the SIT vidicon, we were able to obtain single-shot multipoint spectra of  $\text{N}_2$  and  $\text{O}_2$  at room temperature.

We obtained qualitative information on the instantaneous species concentration and temperature at 20 spatially resolved volume elements ( $0.1 \times 0.1 \times 0.1 \text{ mm}^3$ ) along a line. Coflowing gases of either different species or different temperatures were observed. We used combinations of  $\text{N}_2$ ,  $\text{O}_2$  (which has a rotational spectrum in the same spectral region as  $\text{N}_2$ ), Ar, and freon (neither of which has a spectrum in this region). We also used coflowing hot and cold  $\text{N}_2$ , although the results from this were not nearly as striking since we found significant mixing of the two flows. The boundaries were much more clear-cut in the case of different species at the same temperature. Two major difficulties

remain in using the multipoint CARS technique to obtain quantitative information on temperature and concentration. First, the CARS signal must be adequately normalized to take into account random intensity fluctuations in the dye laser spectrum and in the spatial profiles of the input beams. Second, various distortions in spatial position and in intensity are introduced in both the optical path and in the detection system (spectrograph, image intensifier, and vidicon). The potential of the multipoint CARS technique to quantitatively determine temperature and concentration will depend on the degree to which the difficulties with normalization and distortion can be overcome.

## 1. INTRODUCTION

The measurement of temperature and concentration in a gas is an important problem in turbulence and combustion research. Accurate measurements are required both for diagnostic work in complex systems of technological importance (e.g., jet and internal combustion engines) and to provide data on simpler systems to aid the development of accurate theoretical models. Optical measurement techniques in general are very attractive for these applications because they do not require the placement of a mechanical probe in the medium; they are therefore inherently non-intrusive and are potentially applicable in hostile environments such as the interior of combustors. Spontaneous Raman scattering in particular is recognized as a useful diagnostic technique because Raman spectra can be interpreted to yield the temperature and concentration of individual components in the scattering medium (Lapp and Penney, 1974). Unfortunately, Raman scattering suffers from several drawbacks that prevent it from being useful in many applications of interest. The most serious difficulties are its low scattering efficiency, which makes temporally and spatially resolved measurements difficult, and the fact that the Raman-shifted signal is isotropically scattered, which results in the weak Raman signals being easily swamped by unwanted background light. Coherent anti-Stokes Raman spectroscopy (CARS) is a relatively new type of Raman spectroscopy that is not subject to these disadvantages and at the same time retains many of the best features of spontaneous Raman scattering.

CARS is a nonlinear optical process that was first discussed and

demonstrated not long after the implementation of the first laser in 1964 (Maker and Terhune, 1965), but has only become a viable diagnostic technique in gaseous media in the past several years, due largely to the development of reliable high power solid-state and tunable dye lasers. Very briefly, CARS is a nonlinear mixing process in which laser beams at two different frequencies are combined to produce a Raman signal at a new frequency. The CARS process is characterized by high conversion efficiency (many orders of magnitude greater than spontaneous Raman scattering) and by the coherent, laser-like quality of the output signal. These features make CARS applicable to systems in which time-resolved measurements are required and to systems with high levels of background illumination, since the collimated signal beam can easily be spatially filtered to reject the unwanted background light. Like spontaneous Raman scattering, the CARS technique generates spectra that can be interpreted to yield the temperature and concentration of a specific species (Tolles et al., 1977).

The goal of the work presented in this report was to apply the CARS technique to the instantaneous measurement of temperature in nitrogen gas with good spatial resolution. The primary temperature range of interest was room temperature and below, which is important in wind tunnel and shock-tube diagnostic work where large temperature variations can be found in regions of rapid expansion. Although CARS is currently being widely applied to the measurement of temperature and pressure in gaseous systems, most of the work is being done with the large frequency shifts associated with the rotational-vibrational Raman lines (e.g., the Q-branch in  $N_2$  with a shift of  $2331\text{ cm}^{-1}$ ) for application to high temperature (1000 to 2500 K) combustion systems (Eckbreth et al.,

1979). At room temperature, however, there is virtually no population outside the ground vibrational state, so all temperature information must come from the distribution of population among the rotational levels. In the present work the rotational populations were deduced from the CARS spectra of the pure rotational Raman lines. In principle, the same information could be obtained from the rotational lines in the first Q-branch, but the pure rotational lines are better resolved and have larger Raman scattering cross sections. Extension of the CARS technique to the small shifts associated with the rotational Raman lines introduces experimental problems not encountered with large shifts, so that until recently the only rotational CARS work reported was done on the  $J = 3 \rightarrow 5$  transition in  $H_2$  at a Raman frequency of  $1033.4\text{ cm}^{-1}$  (Barrett, 1976) and in air down to shifts of  $40\text{ cm}^{-1}$  (Beattie et al., 1978). Very recently, there have been reports of rotational CARS spectra in the range of 0 to  $200\text{ cm}^{-1}$  (Goss et al., 1980; Shirley et al., 1980), although no extensive attempts to deduce the rotational temperature from the spectra have been reported.

### 1.1 General CARS Theory

Coherent anti-Stokes Raman spectroscopy is based on a nonlinear optical effect more generally known as four-wave mixing, which is one of many nonlinear phenomena that are derived from the third-order, nonlinear susceptibility,  $\chi^{(3)}$ . Other third-order effects include third-harmonic generation, self-focusing and stimulated Raman scattering. All of these can be effectively described from a semiclassical viewpoint in which optical frequency fields are treated classically with Maxwell's equations, and the macroscopic, classical optical properties (e.g., the susceptibility) of the nonlinear medium are derived from microscopic

ORIGINAL PAGE IS  
OF POOR QUALITY

calculations utilizing quantum mechanics (Bloembergen, 1965). This section presents a review of the theory of the CARS effect.

### 1.1.1 Macroscopic Nonlinear Optics

The polarization induced in a dielectric medium can be written as a power series in the applied electric field as follows:

$$\vec{P}(\vec{r}, t) = \chi^{(1)} : \vec{E}(\vec{r}, t) + \chi^{(2)} : \vec{E}(\vec{r}, t) \vec{E}(\vec{r}, t) + \chi^{(3)} : \vec{E}(\vec{r}, t) \vec{E}(\vec{r}, t) \vec{E}(\vec{r}, t) + \dots \quad (1.1)$$

$\vec{P}(\vec{r}, t)$  is the macroscopic polarization induced at position  $\vec{r}$ , and  $\chi^{(i)}$  is a complex,  $(i + 1)^{\text{th}}$  rank tensor. Rather than work in the time domain with the nonlinear polarization given in Eq. (1.1), it is customary to work in the frequency domain with the Fourier transform. The third-order polarization is then written (Anderson and Hudson, 1978).

$$P_i^{(3)}(\vec{r}, \omega_4) = D \chi_{ijkl}^{(3)}(\omega_4; \omega_1, \omega_2, \omega_3) E_j(\vec{r}, \omega_1) \times E_k(\vec{r}, \omega_2) E_l(\vec{r}, \omega_3) \delta(\omega_4 - \omega_1 - \omega_2 - \omega_3), \quad (1.2)$$

where we have used  $E(\vec{r}, t) = \int_{-\infty}^{\infty} E(\vec{r}, \omega) e^{-i\omega t} d\omega$  and have assumed that the input electric field  $E(\vec{r}, \omega)$  is composed of three discrete frequency components. Equation (1.2) presents the usual definition of the third-order, nonlinear susceptibility,  $\chi^{(3)}$ .  $D$  is a degeneracy factor that takes on the values 6, 3, or 1, depending on whether none, two, or all of the frequencies  $\omega_1, \omega_2, \omega_3$  are degenerate. For the type of four-wave mixing that is responsible for CARS, the nonlinear polarization

of interest has frequency  $\omega_4 = \omega_1 + \omega_2 - \omega_3$  and is written

$$P_i^{(3)}(\vec{r}, \omega_4) = 6\chi_{ijkl}^{(3)}(\omega_4; \omega_1, \omega_2, -\omega_3) E_j(\vec{r}, \omega_1) E_k(\vec{r}, \omega_2) \\ \times E_l^*(\vec{r}, \omega_3) \delta(\omega_4 - \omega_1 - \omega_2 + \omega_3). \quad (1.3)$$

Because  $\chi^{(3)}$  is a fourth-rank tensor, it must in general contain 81 elements. In isotropic media, it can be shown that  $\chi^{(3)}$  contains only 4 unique nonzero elements,  $\chi_{1111}^{(3)}$ ,  $\chi_{1212}^{(3)}$ ,  $\chi_{1221}^{(3)}$ ,  $\chi_{1122}^{(3)}$ , 3 of which are independent since  $\chi_{1111}^{(3)} = \chi_{1212}^{(3)} + \chi_{1221}^{(3)} + \chi_{1122}^{(3)}$ . The two polarization cases usually of interest in practical CARS applications are:

Case (1) (1)  $\vec{E}(\omega_1) \parallel \vec{E}(\omega_2) \parallel \vec{E}(\omega_3)$ , in which

$$P_i^{(3)}(\omega_4) = 6\chi_{1111}^{(3)}(\omega_4; \omega_1, \omega_2, -\omega_3) E_i(\omega_1) E_i(\omega_2) E_i^*(\omega_3); \quad (1.4)$$

Case (2) (2)  $\vec{E}(\omega_1) \parallel \vec{E}(\omega_2) \perp \vec{E}(\omega_3)$ , in which

$$P_i^{(3)}(\omega_4) = 6\chi_{1221}^{(3)}(\omega_4; \omega_1, \omega_2, -\omega_3) E_j(\omega_1) E_j(\omega_2) E_j^*(\omega_3). \quad (1.5)$$

Although other polarization conditions in which  $\vec{E}(\omega_1)$  and  $\vec{E}(\omega_2)$  are not parallel are sometimes employed to increase the CARS detectivity (Oudar et al., 1979; Rahn et al., 1979), the only polarization condition used in the present work is that given in case (2).

If the electric fields are assumed to be plane waves propagating along the z-axis, the Maxwell's wave equation can be reduced to the form

$$\frac{\partial \vec{E}'(\vec{r}, \omega_4)}{\partial z} = i \frac{2\pi k_4}{n_4^2} \vec{P}(\vec{r}, \omega_4), \quad (1.6)$$

where we have used  $\vec{E}(\vec{r}, t) = \vec{E}'(\vec{r}, \omega)e^{-i(\omega t - k_z z)}$  and have assumed that  $\vec{E}'(\vec{r}, \omega)$  is a slowly varying function of  $\vec{r}$  (constant over distances  $\sim \lambda$ ). Assuming undepleted (constant) input fields  $E(\omega_1)$ ,  $E(\omega_2)$  and  $E(\omega_3)$ , Eq. (1.6) can be integrated directly using Eq. (1.5) to obtain

$$\begin{aligned} E_i'(\vec{r}, \omega_4) &= \frac{2\pi k_4}{n_4^2} [6\chi_{1221}^{(3)}(\omega_4; \omega_1, \omega_2, -\omega_3)] E_j(\vec{r}, \omega_1) E_j(\vec{r}, \omega_2) \\ &\quad E_i^*(\vec{r}, \omega_3) \left( \frac{e^{i\Delta kz} - 1}{\Delta k} \right), \end{aligned} \quad (1.7)$$

where  $\Delta k \equiv k_4 - (k_1 + k_2 - k_3)$ . A more general treatment in which the fields are not assumed to be copropagating yields the usual vector phase-matching relation  $\Delta \vec{k} = \vec{k}_4 - (\vec{k}_1 + \vec{k}_2 - \vec{k}_3)$ . The detected intensity  $I(\omega_4)$  is therefore given by (using  $I = nc/8\pi |E|^2$ )

$$\begin{aligned} I(\omega_4) &= \frac{(8\pi)^2}{n_1 n_2 n_3 n_4} \left( \frac{\omega_4}{c} \right)^4 |6\chi_{1221}^{(3)}|^2 I(\omega_1) I(\omega_2) I(\omega_3) \\ &\quad \times \ell^2 \left[ \frac{\sin(\Delta k \ell / 2)}{\Delta k \ell / 2} \right]^2, \end{aligned} \quad (1.8)$$

where  $\Delta k \ell = \Delta \vec{k} \cdot \vec{\ell}$  and  $\vec{\ell}$  is the vector defining the path of signal propagation through the nonlinear medium. The integral along the direction  $\vec{\ell} \parallel \vec{k}_4$  [assumed to be along the  $z$ -axis in deriving Eq. (1.7)] is simply interpreted as the summation of the fields radiated by the polarizations at different sites. When the summation is performed in the phase-matched direction the fields constructively interfere, yielding a large, highly directional signal. For perfect phase matching,  $[\sin(\Delta k \ell / 2) / (\Delta k \ell / 2)]^2 = 1$ , and the signal intensity increases quadratically with pathlength through the medium. The important features

exhibited by Eq. (1.8) are summarized here:

$$\omega_4 = \omega_1 + \omega_2 - \omega_3$$

$$\vec{k}_4 = \vec{k}_1 + \vec{k}_2 - \vec{k}_3$$

$$I(\omega_4) = I(\omega_1)I(\omega_2)I(\omega_3)$$

$$I(\omega_4) \propto |\chi^{(3)}|^2$$

$$I(\omega_4) \propto \ell^2 \quad (\Delta k \ell = 0).$$

### 1.1.2 Nonlinear Susceptibility Due to Raman-Type Resonances

The nonlinear susceptibility can be written as a sum of resonant and nonresonant terms. The resonant terms are responsible for the Raman-like features in a CARS spectrum and are discussed more fully below. The nonresonant term arises from the mixing of the optical fields due to the nonlinear response of the electrons in the medium. The nonresonant signal generated at  $\omega_4$  is spectrally featureless and is usually small compared to the resonantly enhanced signals. An energy level diagram that illustrates the mixing process is shown in Fig. 1.1(a); note that none of the indicated transitions terminate in real excited states and that the initial and final states of the medium are identical. This diagram clearly indicates that the four-wave mixing responsible for CARS is a parametric process in which energy is transferred among the optical fields but is not added to or removed from the medium. The nonresonant susceptibility ( $\chi_{NR}^{(3)}$ ) is, therefore, a real quantity, since an imaginary component would imply some loss or gain.

Resonant enhancement of the susceptibility can occur whenever one of the frequencies  $\omega_1$ ,  $\omega_2$ ,  $\omega_3$  or any combination of them corresponds to a real transition in the medium. The CARS process results when a difference frequency corresponds to a Raman transition in the material. The appropriate energy level diagram is shown in Fig. 1.1(b), where  $\omega_{\text{RAM}} = \omega_2 - \omega_3$  has been assumed for definiteness.

Following the general arguments of the Placzek polarizability approximation (Weber, 1973), the electronic polarizability of an individual molecule (the following development implicitly assumes that the nonlinear medium is a gas) is written (Giordmaine and Kaiser, 1966)

$$\alpha_{ij} = (\alpha_0)_{ij} + \left( \frac{\partial \alpha}{\partial q} \right)_{ij} q ,$$

where  $(\alpha_0)_{ij}$  is the polarizability of a molecule with fixed nuclei and  $(\partial \alpha / \partial q)_{ij}$  is the change in electronic polarizability due to a change in the nuclear conformation  $q$  ( $q$  can be interpreted as the amplitude of the nuclear motion corresponding to a rotational-vibrational transition). Thus, the microscopic induced polarization in the presence of an applied field  $\vec{E}$  is

$$\vec{p} = \vec{\alpha} \vec{E} = \left( \frac{\vec{\alpha}}{\partial q} \right) \langle q \rangle \vec{E} , \quad (1.9)$$

where  $\alpha_0$ , which leads to elastic scattering, has been neglected. By a simple, semiclassical calculation for a two-level system in which  $q$  is assumed to be driven at frequency  $\omega_2 - \omega_3$  by the applied fields at  $\omega_2$  and  $\omega_3$ , it can be shown that (Maier, 1976)

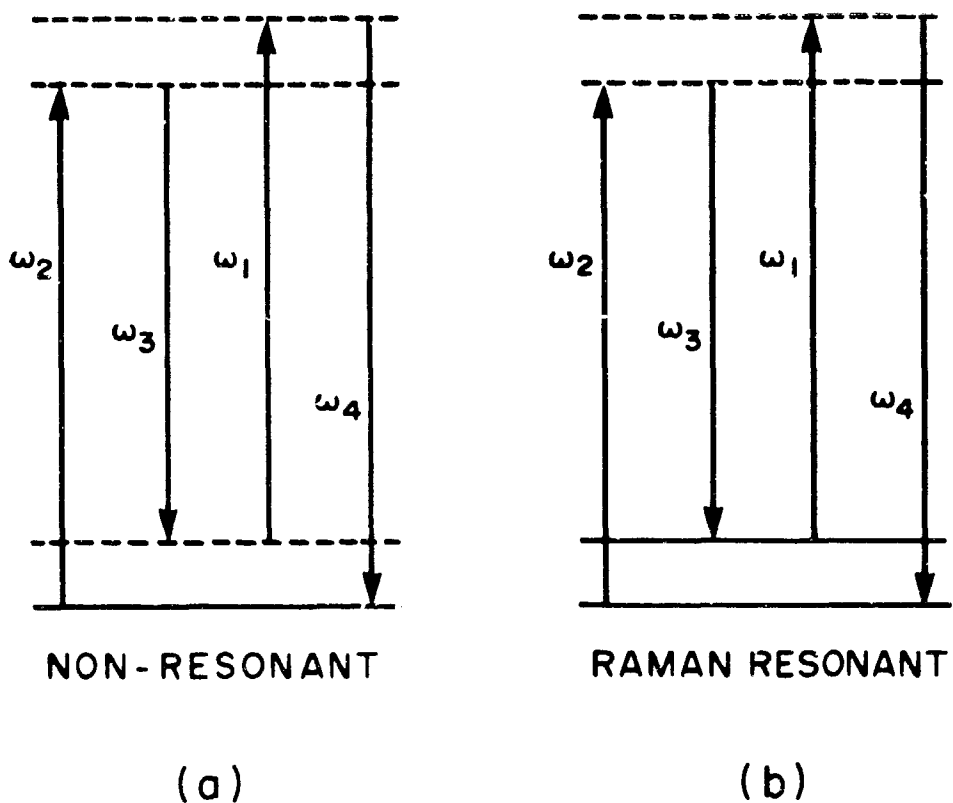


Fig. 1.1. Energy level diagrams for nonresonant (a) and Raman-resonant (b) four-wave mixing. Real and virtual states are indicated by solid and dashed lines, respectively.

$$\langle q \rangle = \frac{\left( \frac{\omega_{\text{rov}}}{\hbar} \right) q_{01}^2 \left( \frac{\partial \alpha}{\partial q} \right)_{ij} E_i^2(\vec{r}, t) E_j^{3*}(\vec{r}, t) \Delta}{\omega_{\text{rov}}^2 - (\omega_2 - \omega_3)^2 - i\Gamma(\omega_2 - \omega_3)} . \quad (1.10)$$

The meanings of the various terms are as follows:

$\omega_{\text{rov}}$  = transition frequency between the upper and lower rotational-vibrational states.

$\Delta$  = difference in the occupational probability between the lower and upper levels (pop. lower - pop. upper)

$q_{01}^2$  = square of matrix element of operator  $q$  coupling the two states.

$\Gamma$  = damping term; corresponds to the inverse of the dephasing time ( $1/T_2$ ) in the Bloch equations.

The induced polarization at  $\omega_4 = \omega_1 + (\omega_2 - \omega_3)$  is obtained by using  $E(\omega_2)$  in Eq. (1.9) to obtain

$$P_\ell(\vec{r}, t) = \left( \frac{\partial \alpha}{\partial q} \right)_{lm} \langle q \rangle E_m^1(\vec{r}, t) . \quad (1.11)$$

Recalling that the electric fields are  $\vec{E}_i^1(\vec{r}, t) = E_i(\vec{r}, \omega_i) e^{i(k_i z - \omega_i t)}$ ,

and using Eq. (1.10) for  $\langle q \rangle$ , yields

$$P_\ell(\vec{r}, \omega_4) = \frac{N \left( \frac{\omega_{\text{rov}}}{\hbar} \right) q_{01}^2 \left( \frac{\partial \alpha}{\partial q} \right)_{ij} \left( \frac{\partial \alpha}{\partial q} \right)_{lm} \Delta E_i(\vec{r}, \omega_2) E_j^*(\vec{r}, \omega_3) E_m(\vec{r}, \omega_4)}{\omega_{\text{rov}}^2 - (\omega_2 - \omega_3)^2 - i\Gamma(\omega_2 - \omega_3)} \quad (1.12)$$

$$\times e^{i(k_1 + k_2 - k_3 - k_4)z} .$$

Eq. (1.12) gives the macroscopic polarization and was obtained from

Eq. (1.11) by multiplying by the molecular density  $N$ ; in a solid or liquid it would also be necessary to include local field corrections.

Comparison of Eq. (1.12) with the nonlinear polarization derived using the  $\chi^{(3)}$  formalism [Eq. (1.3)] yields an expression for the Raman-resonance enhanced susceptibility. Recalling that  $\chi^{(3)}(\omega_4, \omega_1, \omega_2, -\omega_3) = \chi_{NR}^{(3)} + \chi_{RAM}^{(3)}(\omega_4; \omega_1, \omega_2, -\omega_3)$ , we find that

$$(\chi_{RAM}^{(3)}(\omega_4; \omega_1, \omega_2, -\omega_3))_{ijkl} = \frac{N \left( \frac{\omega_{rov}}{6\hbar} \right) q_{01}^2 \left( \frac{\partial \alpha}{\partial q} \right)_{ij} \left( \frac{\partial \alpha}{\partial q} \right)_{kl} \Delta}{\omega_{rov}^2 - (\omega_2 - \omega_3)^2 - i\Gamma(\omega_2 - \omega_3)}. \quad (1.13)$$

Equation (1.11) can be reconciled with the corresponding expression obtained in a quantum mechanical treatment by replacing some of the classical quantities with their quantum mechanical analogues. First of all, the perturbation theory calculation yields a true Lorentzian lineshape function (Nibler and Knighten, 1979) which differs slightly from that in Eq. (1.13); in the remainder of this work the substitution

$$\frac{2\omega_{rov}}{\omega_{rov}^2 - (\omega_2 - \omega_3)^2 - i\Gamma(\omega_2 - \omega_3)} \rightarrow \frac{1}{\omega_{rov} - (\omega_2 - \omega_3) - i\Gamma} \quad (1.14)$$

will be used. Here,  $\Gamma$  is recognized as the half-width at half-maximum of the Raman line. Also, the polarizability matrix elements  $(\alpha_{lm})_{if}$  between the initial and final levels coupled by the Raman transition are easily identified with the polarizability derivative

$$(\alpha_{lm})_{if} = \langle i | \alpha_{lm} | f \rangle \leftrightarrow \left( \frac{\partial \alpha}{\partial q} \right) q_{if}. \quad (1.15)$$

The population difference factor,  $\Delta$ , that appears in Eq. (1.13) indicates that the intensity of a CARS peak depends on the difference in population between the initial and final rovibrational states. This is quite different from ordinary Raman scattering where the intensity is proportional to the initial state population only; the difference between the two types of spectra is particularly pronounced in the case of pure rotational scattering. This leads to a possible source of error in CARS spectra because  $\Delta$  may change during the course of a laser pulse (Tolles et al., 1977). Away from exact resonance ( $\omega_2 - \omega_3 \neq \omega_{\text{rov}}$ ) the nonlinear susceptibility is composed of  $\chi_{\text{NR}}^{(3)}$  and the off-resonant tail of the Lorentzian line due to  $\chi_{\text{RAM}}^{(3)}$ . Thus,  $\chi^{(3)}$  is almost entirely real and no real transitions in the medium can occur. In this case, the CARS process is purely parametric [see Fig. 1.1(a)] and the population difference associated with  $\chi_{\text{RAM}}^{(3)}$  is constant. As  $\omega_2 - \omega_3$  is tuned to resonance, however, there is a possibility of real transitions between the upper and lower rovibrational states. Although the CARS process is still strictly parametric, there are other nonlinear processes (e.g., stimulated Raman scattering) that occur simultaneously with the CARS and can result in the transfer of population from the lower to upper state, thus decreasing  $\Delta$ . This saturation effect causes a loss of signal intensity and distorts  $\Delta$  away from the initial value determined by the population distribution at thermal equilibrium. This must be avoided if an accurate temperature is to be inferred from a CARS spectrum.

In the CARS process the rovibrational transitions are driven by the coherent fields  $E(\omega_2)$  and  $E(\omega_3)$ , and the values of  $\langle q \rangle$  at different molecular sites are related in phase by the factor  $\exp[i(k_2 - k_3)z]$ . As before, the detected intensity is given by the square of the sum

of the scattered fields from all sites,

$$I(\omega_4) \propto \left| \sum_i E_i(\vec{r}, \omega_4) e^{i[(\vec{k}_4 - \vec{k}_1 - \vec{k}_1 + \vec{k}_3) \cdot \vec{r} - \omega_4 t]} \right|^2.$$

If the summation is performed along the phase-matched direction, the phase factor is zero, the scattered fields interfere constructively and the cross terms do not vanish. This results in a large, highly directional signal, since for any other direction the fields experience destructive interference which prevents the build-up of a large amplitude scattered field. The detected signal in the phase-matched direction is therefore given by

$$\begin{aligned} I(\omega_4) &\propto \left| \sum_i (\chi_{\text{RAM}}^{(3)})^i E(\omega_1) E(\omega_2) E^*(\omega_3) \right|^2 \\ &\propto \left| \sum_i (\chi_{\text{RAM}}^{(3)})^i \right|^2 I(\omega_1) I(\omega_2) I(\omega_3) . \end{aligned} \quad (1.16)$$

Using Eqs. (1.13) and (1.14) in Eq. (1.16) yields

$$\left| \sum_i (\chi_{\text{RAM}}^{(3)})^i \right|^2 = \left| \frac{N(-\frac{1}{12h}) (\frac{\partial \alpha}{\partial q})_{ij} (\frac{\partial \alpha}{\partial q})_{kl} q_{01}^2 \Delta}{\omega_{\text{rov}} - (\omega_2 - \omega_3) - i \Gamma} \right|^2 . \quad (1.17)$$

Since  $\chi_{\text{RAM}}^{(3)}$  depends on the square of the polarizability derivative, it can be related to the ordinary Raman scattering cross section,

$$\left( \frac{\partial \sigma}{\partial \Omega} \right) = \left( \frac{\omega_s}{c} \right)^4 \left| \left( \frac{\partial \alpha}{\partial q} \right) \langle q \rangle \right|^2 .$$

$$\left| \sum_i \chi_{\text{RAM}}^{(3)} \right|^2 = \left| \frac{\frac{N}{12h} \left( \frac{c}{\omega_s} \right)^4 \left( \frac{\partial \sigma}{\partial \Omega} \right) \Delta}{\omega_{\text{rov}} - (\omega_2 - \omega_3) - i \Gamma} \right|^2 ,$$

and the detected CARS intensity is seen to depend upon the square of the ordinary Raman scattering cross section.

In addition to summing over all molecular sites in Eq. (1.17) it is also necessary to include the nonresonant susceptibility and resonant terms from neighboring Raman lines in the sum. Because the detected signal depends on the square of the sum of the scattered fields, it is possible to have interferences between nearby resonances and between the resonant and nonresonant contributions. Therefore, the net nonlinear susceptibility is given by

$$\chi^{(3)} = \chi_{\text{NR}}^{(3)} + \sum_i \left\{ \frac{\frac{N}{12h} \left( \frac{c}{\omega_s} \right)^4 \left( \frac{\partial \sigma}{\partial \Omega} \right)_i \Delta_i}{\omega_i - (\omega_2 - \omega_3) - i \Gamma_i} \right\} , \quad (1.18)$$

where the sum is now over all Raman resonances. Interference between the various terms of Eq. (1.18) is a major source of difficulty with CARS and will be discussed more fully for pure rotational spectra in Section 4.

1.2 Nonlinear Susceptibility due to Rotational Raman Resonances inNitrogen Gas

The general expression for the resonant nonlinear susceptibility developed in the previous section will now be specialized to the case of pure rotational Raman transitions in nitrogen gas. The intensity factors for the Raman transitions are derived from the polarizability matrix elements introduced in Eq. (1.15). The exact form of the temperature dependent population difference,  $\Delta$ , is derived, including the nuclear spin degeneracy factor. The final expression obtained for  $\chi_{\text{RAM}}^{(3)}$  will be directly applicable to the interpretation of the experimental, temperature dependent CARS spectra generated in this work.

1.2.1 Evaluation of the Raman Matrix Elements in N<sub>2</sub>

The contribution to the nonlinear susceptibility due to the rotational Raman transition  $J \rightarrow J + 2$  can be written using Eq. (1.19)

$$(\chi_{ijk\ell}^{(3)})_{J,J}^{\text{RAM}} = \left\{ \frac{\left( \frac{N}{12h} \right) \Delta_J \left( \frac{\partial \alpha}{\partial q} \right)_{ij} \left( \frac{\partial \alpha}{\partial q} \right)_{k\ell} q_{01}^2}{\omega_J - (\omega_2 - \omega_3) - i \Gamma_J} \right\}$$

where  $\omega_J = [E(J+2) - E(J)]/h$ ,  $\Delta_J$  = population of level  $J$  minus population of level  $J+2$ , and  $\Gamma_J$  is the HWHM of the  $J \rightarrow J+2$  Raman line.

A given  $J$  rotational level is  $(2J+1)$ -fold degenerate in the magnetic quantum number  $M$  (assuming no applied magnetic field). Therefore, in order to obtain the susceptibility for the entire  $J$  to  $J+2$  Raman transition, it is necessary to sum over all degenerate  $M$  levels, leading to the substitution:

$$N\Delta_J \left| \langle vJM | \alpha_{ij} | v'J'M' \rangle \right|^2 \rightarrow \frac{N}{(2J+1)} \sum_{M,M'} \left| \langle vJM | \alpha_{ij} | v'J'M' \rangle \right|^2 \Delta_{JM}^{J'M'} .$$

where the initial and final states are specified by their vibrational ( $v$ ) and rotational ( $J, M$ ) quantum numbers. The population factor is written to explicitly show that it is associated with the individual matrix elements; since all  $M$  states are degenerate, however, it can be pulled out of the summation. The sums of these matrix elements have been evaluated (James and Klemperer, 1959) using the fact that the vibrational and rotational contributions to the polarizability can be separated for diatomic molecules, as follows:

$$\sum_{MM'} |\langle vJM | \alpha_{ij} | v'J'M' \rangle|^2 = |\langle vJ | \alpha_{ij} | v'J' \rangle|^2 \sum_{MM'} |\langle JM | \alpha_{ij} | J'M' \rangle|^2 .$$

The results of the calculation for S-branch scattering, including the orientational average, are:

$$\sum_{MM'} |\langle vJM | \alpha_{11} | v'J'M' \rangle|^2 = \frac{2}{15} K(J+1) |\langle vJ | \gamma | v'J' \rangle|^2$$

$$\sum_{MM'} |\langle vJM | \alpha_{12} | v'J'M' \rangle|^2 = \frac{1}{10} K(J+1) |\langle vJ | \gamma | v'J' \rangle|^2 ,$$

where  $K(J) = J(J+1)/(2J+1)$  and  $\gamma$  is the anisotropy of the molecular polarizability. As expected, the isotropic part of the polarizability tensor does not play a role in pure rotational scattering, and the pure rotational lines are therefore completely depolarized (the isotropic part of the polarizability tensor only contributes to  $\Delta J = 0$  transitions). The vibrational matrix elements do show a mild  $J$  dependence, but for the low  $J$  values used in this work these terms can be neglected.

### 1.2.2 The Population Difference Factor

The population of a rotational state in thermal equilibrium is determined by Boltzmann statistics and by nuclear spin statistics. Specifically, the population of a particular state characterized by quantum numbers  $J, M$  is:

$$P(JM) = g_J \frac{e^{-E(J)hc/KT}}{Q} \quad (1.20)$$

where

$g_J$  = nuclear spin weighting factor

$Q$  = rotational partition function

$$= \sum_{J=0}^{\infty} g_J (2J + 1) e^{-E(J)hc/kT} .$$

Therefore, the population difference factor  $\Delta_{JM}^{J'M'}$  is

$$\Delta_{J,M}^{J+2,M'} \equiv \Delta_J = P(J, M) - P(J + 2, M')$$

$$= g_J \frac{e^{-E(J)hc/KT}}{Q} \frac{(1 - e^{-\omega_J hc/KT})}{(1 - e^{-\omega_{J+2} hc/KT})} ,$$

where  $\Delta_J$  is now written to show that it is independent of  $M$ . For the  $N_2$  molecule in which states with even  $J$  are (+), s, and states with odd  $J$  are (-), a, we find that the above argument requires that  $g_J = 2$  for  $J$  even and  $g_J = 1$  for  $J$  odd.

The final expressions for the nonlinear susceptibility elements used in this work are as follows:

$$(\chi_{1111}^{(3)})_{J \text{ RAM}} = \frac{\frac{4N}{360\hbar} |\gamma_{vJ, v'J'}|^2 S(J) P(J) (1 - e^{-\omega_J hc/kT})}{\omega_J - (\omega_2 - \omega_3) - i\Gamma_J}$$

$$(\chi_{1221}^{(3)})_{J \text{ RAM}} = \frac{\frac{3N}{360\hbar} |\gamma_{vJ, v'J'}|^2 S(J) P(J) (1 - e^{-\omega_J hc/kT})}{\omega_J - (\omega_2 - \omega_3) - i\Gamma_J},$$

where  $S(J) = (J + 1)(J + 2)/(2J + 1)(2J + 3)$  and  $P(J)$  is as given in Eq. (1.20). These expressions can be rewritten in terms of the ordinary Raman scattering cross section for the  $J^{\text{th}}$  Raman line as

$$(\chi_{1111}^{(3)})_{J \text{ RAM}} = \frac{\frac{N}{12\hbar} \left(\frac{c}{\omega_s}\right)^2 \left(\frac{\partial \sigma}{\partial \Omega}\right)_J P(J) (1 - e^{-\omega_J hc/kT})}{\omega_J - (\omega_2 - \omega_3) - i\Gamma_J}$$

$$(\chi_{1221}^{(3)})_{J \text{ RAM}} = \frac{\frac{3N}{48\hbar} \left(\frac{c}{\omega_s}\right)^2 \left(\frac{\partial \sigma}{\partial \Omega}\right)_J P(J) (1 - e^{-\omega_J hc/kT})}{\omega_J - (\omega_2 - \omega_3) - i\Gamma_J}.$$

## 2. THREE-DIMENSIONAL PHASE MATCHING

The phase-matching requirement derived in Section 1.1.1 is

$$\vec{k}_4 = \vec{k}_1 + \vec{k}_2 - \vec{k}_3$$

where

$$|\vec{k}_1| = 2\pi n_i / \lambda = n_i \frac{\omega}{c}$$

$n_i$  = refractive index at  $\lambda_i$ .

$N_2$  has no strong absorption lines in the visible region of the spectrum, so  $n$  is nearly constant and can be ignored. The simplest phase-matching geometry, then, is one in which the three input beams and the signal beam are colinear, since  $|\vec{k}_3| + |\vec{k}_4| = |\vec{k}_1| + |\vec{k}_2|$ . This geometry is perfectly phase-matched for all Raman shifts and is easily implemented experimentally, but it suffers from two serious drawbacks. First, it offers inherently poor spatial resolution since the CARS signal is generated over the entire region of overlap of the beams. Although the colinear beams are generally brought to a focus, at which point the signal conversion efficiency is the highest, significant mixing can still occur over a region several centimeters in length. Second, it can be difficult to separate the relatively weak signal at  $\omega_4$  from the high power input beams at frequencies  $\omega_1$ ,  $\omega_2$ , and  $\omega_3$ . In rotational-vibrational CARS, the shifts are large and it is possible to separate the beams with dichroic beamsplitters, but this approach is impossible in pure rotational CARS where the Raman shifts are very small ( $\gtrsim 10 \text{ cm}^{-1}$ ).

## 2.1 Calculation of Phase-Matching Angle

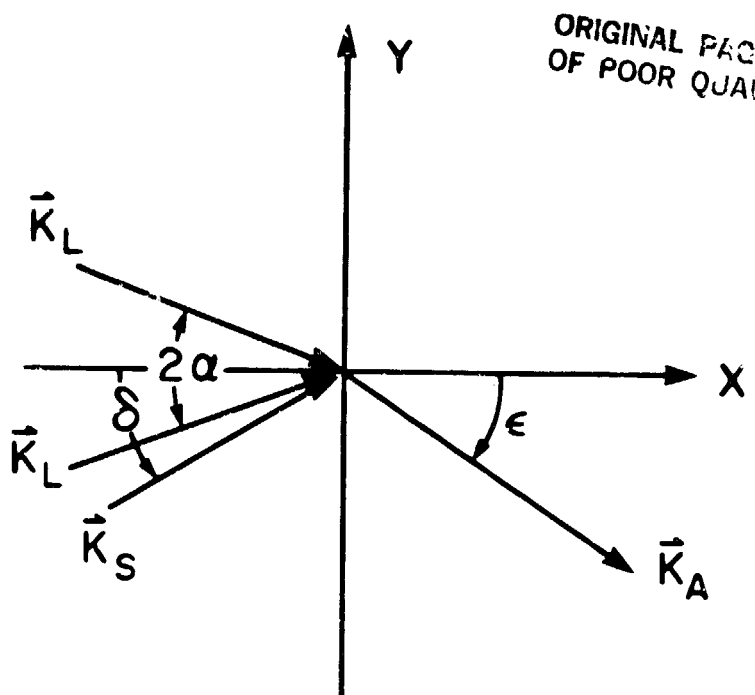
There is no general requirement for colinear phase-matching and several years ago a scheme was proposed in which the three input beams are slightly separated in angle (Eckbreth, 1978). Because signal is generated only from the region in which the beams overlap, this approach offers greatly improved spatial resolution over the colinear case. This geometry is shown in Fig. 2.1 along with the appropriate phase-matching equations. If a particular value of  $\alpha$  is chosen, the equations can be solved for  $\delta$  and  $\epsilon$ :

$$\cos\delta = \frac{k_L \cos^2\alpha - \theta}{k_S \cos\alpha}$$

$$\sin\epsilon = \frac{k_S \sin\delta}{k_A}$$

where we have used the usual assignments  $k_1 = k_2 = k_L$ ,  $k_3 = k_S$ , and  $k_4 = k_A$ . The important point to note from these equations is that for small shifts ( $\theta$ ), the angular separation of the beams is insignificant, since  $k_L \sim k_S \sim k_A$  and  $\theta \sim 0$  imply that  $\cos\delta \sim \cos\alpha$  and  $\sin\epsilon \sim \sin\delta$ . As a numerical example, choose  $\theta = 50 \text{ cm}^{-1}$  and  $\alpha = 5^\circ$ ; then  $\delta = 5.01^\circ$  and  $\epsilon = 4.99^\circ$  assuming a pump laser wavelength of 532 nm.

Because angular separation of the beams is required in pure rotational CARS, it is necessary to use a three-dimensional phase-matching geometry in which the dye laser beam is directed to be at an angle out of the plane formed by the two pump beams (Prior, 1980; Shirley et al., 1980). The geometry and phase-matching equations are shown in Fig. 2.2. Because there are 5 angles and only 3 equations, it is necessary to choose two angles and

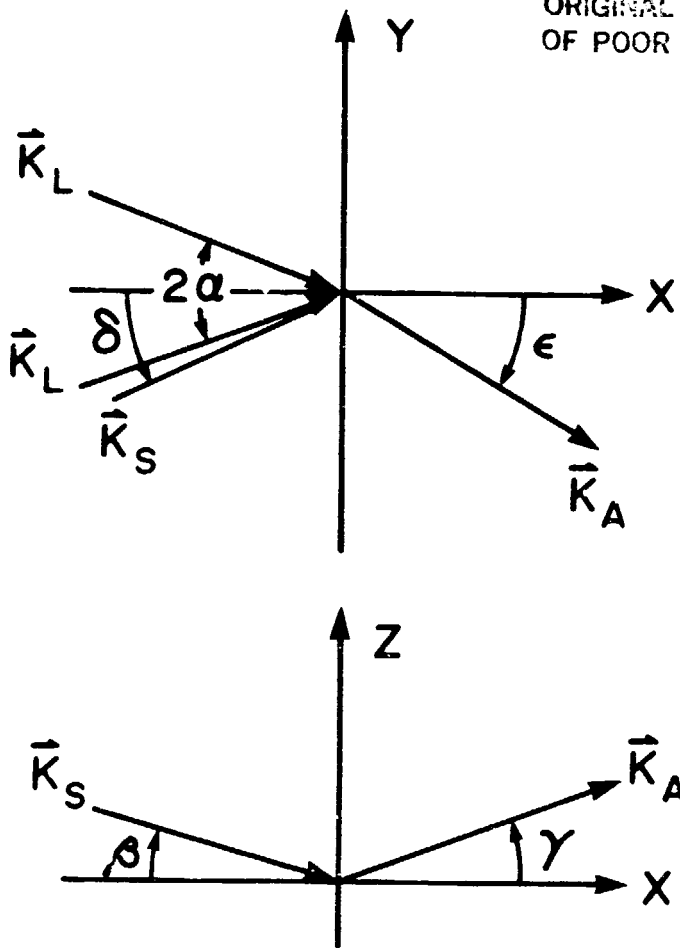


$$x: k_L \cos\alpha + k_L' \cos\epsilon - k_S \cos\delta = k_A \cos\epsilon$$

$$y: k_L \sin\alpha - k_L' \sin\alpha - k_S \sin\delta = -k_A \sin\epsilon$$

Fig. 2.1. The BOXCARS phase-matching diagram and equations.

ORIGINAL PAGE IS  
OF POOR QUALITY



$$x: k_L \cos\alpha + k_L \cos\alpha - k_S \cos\delta \cos\beta = k_A \cos\epsilon \cos\gamma$$

$$y: k_L \sin\alpha - k_L \sin\alpha - k_S \sin\delta \cos\beta = -k_A \sin\epsilon \cos\gamma$$

$$z: k_S \sin\beta = k_A \sin\gamma$$

Fig. 2.2. Three-dimensional phase-matching diagrams and equations.

solve for the remaining three. Choosing  $\alpha$  and  $\beta$  yields

$$\cos\delta = \frac{k_L}{k_S} \frac{\cos^2\alpha - \theta}{\cos\alpha\cos\beta}$$

$$\sin\gamma = \frac{k_S \sin\beta}{k_A}$$

$$\sin\epsilon = \frac{k_S \sin\beta\cos\delta}{k_A \cos\gamma} .$$

A particularly simple geometry results when  $\delta = 0$ , in which case one finds

$$\cos\beta = \frac{k_L}{k_S} \frac{\cos^2\alpha - \theta}{\cos\alpha}$$

$$\sin\gamma = \frac{k_S \sin\beta}{k_A}$$

$$\epsilon = 0 .$$

This geometry is shown in Fig. 2.3 and corresponds to that used in the present work, with  $\alpha$  chosen to be  $1.5^\circ$ , so  $\beta = 1.50^\circ$  and  $\gamma = 1.496^\circ$  assuming a shift  $\theta = 50 \text{ cm}^{-1}$ .

## 2.2 Calculation of Coherence Length

A potential source of error that arises in this geometry and not in a colinear geometry is the possibility of phase mismatch over the bandwidth of the dye laser. The values of  $\beta$  and  $\gamma$  calculated above were

ORIGINAL PAGE IS  
OF POOR QUALITY

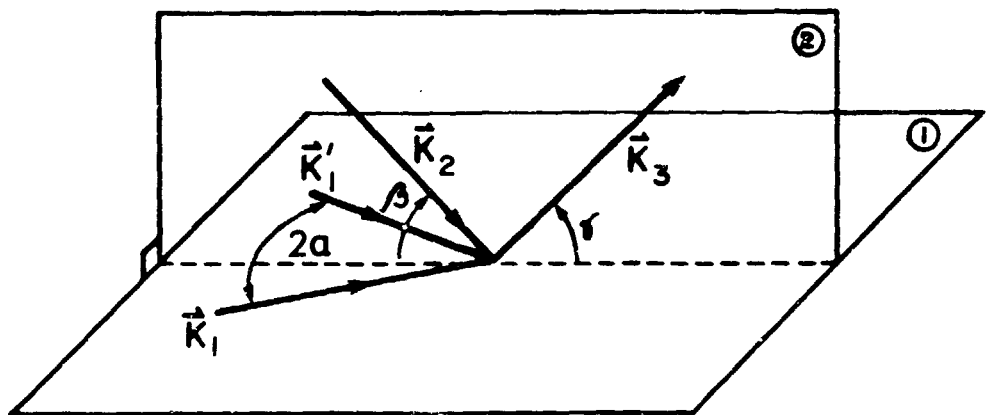


Fig. 2.3. The three-dimensional phase-matching geometry used in the experiment.

based on a Raman shift of  $50 \text{ cm}^{-1}$ , while the desired broadband CARS spectrum may cover the range from 0 to  $100 \text{ cm}^{-1}$ . Calculation of the phase mismatch as a function of the mistuning away from a shift of  $50 \text{ cm}^{-1}$  yields

$$\frac{d(\vec{\Delta k} \cdot \vec{\ell})}{d\mu} = \ell(\cos(\beta + \gamma) - 1)$$

where  $\mu$  is the difference between the actual Raman shift and the value of  $\theta$  for which  $\beta$  and  $\gamma$  were calculated. For a maximum mistuning of  $\mu = \pm 50 \text{ cm}^{-1}$  and the values of  $\beta$  and  $\gamma$  calculated above,  $(\vec{\Delta k} \cdot \vec{\ell}) = \pm \ell \cdot 0.068$ , which yields a coherence length of  $\ell_{coh} = 46 \text{ cm}$  ( $\ell_{coh}$  is defined such that  $\Delta k \ell_{coh} = \pi$ ). Clearly, for an expected interaction length of only a few millimeters, there will be no significant loss of signal due to phase mismatch. If  $\alpha$  were chosen to be quite large for greater spatial resolution, however, the phase mismatch could become a significant source of error. Choosing  $\alpha = 45^\circ$  and  $\theta = 50 \text{ cm}^{-1}$  yields  $\beta = 45.2^\circ$  and  $\gamma = 44.8^\circ$ , in which case the coherence length for a  $100 \text{ cm}^{-1}$  bandwidth is only  $\ell_{coh} = 628 \mu\text{m}$ .

### 3. EXPERIMENTAL IMPLEMENTATION OF BROADBAND CARS

A CARS spectrum contains useful information in both the relative amplitudes of spectral features and in their absolute intensities. The intensity distribution among the Raman features in a given spectrum indicate the temperature of the scattering medium, while the overall signal intensity is a measure of the density. Although absolute density measurements are impractical, the ratio of signal intensities from different media can be used to determine their relative density. Unfortunately, it is difficult to produce experimental spectra that are free of spectral distortions and overall amplitude errors. It is important to record and analyze the experimental spectra in such a way as to correct these errors, if CARS is to be useful as a quantitative diagnostic technique. This chapter is concerned with the problem of obtaining quantitatively correct spectral information from experimental CARS spectra; it contains a discussion of various methods for correcting errors in the spectra as well as a detailed description of the experimental apparatus used in this work.

#### 3.1 Broadband CARS with Multichannel Detection

In a typical CARS experiment, the fields at frequencies  $\omega_1$  and  $\omega_2$  are provided by a single pump laser beam, the field at frequency  $\omega_3$  is provided by a dye laser beam shifted in frequency by  $\theta$  to the Stokes side of the pump frequency, and the signal is generated at frequency shift  $\theta$  to the anti-Stokes side of the pump frequency. In this case the following frequency assignments are used:

$$\omega_1 = \omega_2 \equiv \omega_L$$

$$\omega_3 = \omega_L - \theta \equiv \omega_S$$

$$\omega_4 = \omega_L + \theta \equiv \omega_A .$$

The most commonly used method for generating a CARS spectrum is to hold the pump laser frequency ( $\omega_L$ ) constant and to slowly tune the frequency of the narrow-bandwidth, Stokes-shifted dye laser ( $\omega_S$ ) over the spectral range of interest, thus mapping out the CARS spectrum point by point. Because the CARS signal is produced only at frequency  $\omega_L + \theta_i$ , no monochromator is required to disperse the scattered light which can be directly detected with a photomultiplier tube. In this case the spectral resolution is determined by the bandwidths of the pump and Stokes-shifted lasers, which can be made very narrow with relatively little power loss. Spectra have been obtained with a resolution of  $0.012 \text{ cm}^{-1}$  (Boquillon and Breger, 1979), which greatly exceeds that achievable in conventional Raman spectroscopy.

The single-channel scanning technique is not applicable to making time-resolved measurements in dynamic systems, because several minutes may be required to scan the entire spectral range of interest. Accurate time-resolved measurements require that a complete CARS spectrum be generated in a time that is short compared to that required for the system characteristics (temperature and/or density) to change. Although these times may be as long as many microseconds, most pulsed lasers operate at maximum repetition rates of 10's of pulses per second, which means that the entire spectrum must be generated by a single laser pulse ( $\sim 10 \text{ ns}$  duration for the laser used in this work).

A broad, single-shot CARS spectrum can be generated simply by deriving the Stokes-shifted beam from a dye laser which has a frequency bandwidth comparable to the desired spectral interval to be covered (Roh, et al., 1976). In this case, a particular spectral component of the dye output at frequency  $\omega_S = \omega_L - \theta_i$  will be directly mapped into the anti-Stokes spectrum according to the usual mixing rule  $\omega_A = 2\omega_L - \omega_S = \omega_L + \theta_i$ .

Thus, for a monochromatic pump laser there is a one-to-one correspondence between the dye laser and CARS spectra. The broad-bandwidth CARS signal generated in this way can then be dispersed by a spectrograph and detected with an optical multichannel analyzer (OMA). The spectral resolution in this case will be determined by the dispersion of the spectrograph, by the signal spot size at the spectrograph entrance slit, and by the spatial resolution of the OMA. For a nonmonochromatic pump laser, however, the ultimate resolution of the CARS spectrum will be limited by the pump laser linewidth.

The most important source of error in spectra produced by the single-channel scanning method is the shot-to-shot fluctuation in the intensity of the CARS signal, due to pulse-to-pulse variations in the input laser intensities. Signal fluctuations as large as  $\pm 30\%$  are common, so that the signal from many laser pulses must be averaged at each dye laser setting in order to generate spectra that are free of amplitude errors and spectral distortion. Other sources of error that cannot be overcome simply by averaging many shots are long term drift in the pump and dye laser intensities, and the variation of dye laser efficiency with frequency ( $\omega_S$ ). Long term intensity drift affects both the relative and absolute magnitude of the spectral features, while the dye laser efficiency variation distorts individual spectra without affecting their overall amplitude. All of these difficulties can be ameliorated by use of a reference normalization scheme, but even the most carefully designed scanning systems still require that the signals from several shots be averaged to produce a single point in the spectrum.

The broad-bandwidth, multichannel detection technique is not susceptible to spectral distortion due to shot-to-shot intensity fluctuations or to long

term drift in the laser intensities since an entire spectrum is recorded in a single laser firing. The broad-bandwidth dye laser introduces a new source of spectral error, however, due to the sharp, random variations of laser intensity with frequency. Figure 3.1(a) shows the spectrum of a single dye laser pulse; the sharp structures are due to mode beating among the many weakly coupled cavity modes present in the dye laser output. These structures are directly mapped into the CARS signal, making quantitative interpretation of a CARS spectrum virtually impossible without detailed knowledge of the spectrum of the corresponding dye laser pulse. The spectra are also distorted by the roll-off of average dye laser power at the edges of the bandwidth. Amplitude errors are introduced into the multichannel spectra by the same mechanisms as in the single-channel technique; i.e., shot-to-shot intensity fluctuations and long term drift.

For non-time-resolved measurements in which it is possible to average the signal from many pulses, multichannel detection is superior to the single-channel technique for moderate resolution work. The sharp structures in the dye laser spectrum tend to average out after many pulses, as shown in Fig. 3.1(b), and since the CARS signal is linear in the dye laser intensity, so do the structures in the CARS spectrum. At the same time, averaging many pulses reduces the overall amplitude error due to shot-to-shot intensity fluctuations, just as is the case with scanned spectra. Although both methods of obtaining the spectra are susceptible to errors due to the variation of dye laser efficiency with  $\omega_S$ , only the scanned spectra exhibit spectral distortions due to laser intensity drift. Finally, the multipoint technique is much faster than the single-channel technique because of the usual multiplex advantage of being able to generate an entire, averaged, broadband spectrum in about the same time required to generate a single, averaged point in a scanned spectrum.

ORIGINAL RECORDS  
OF POOR QUALITY

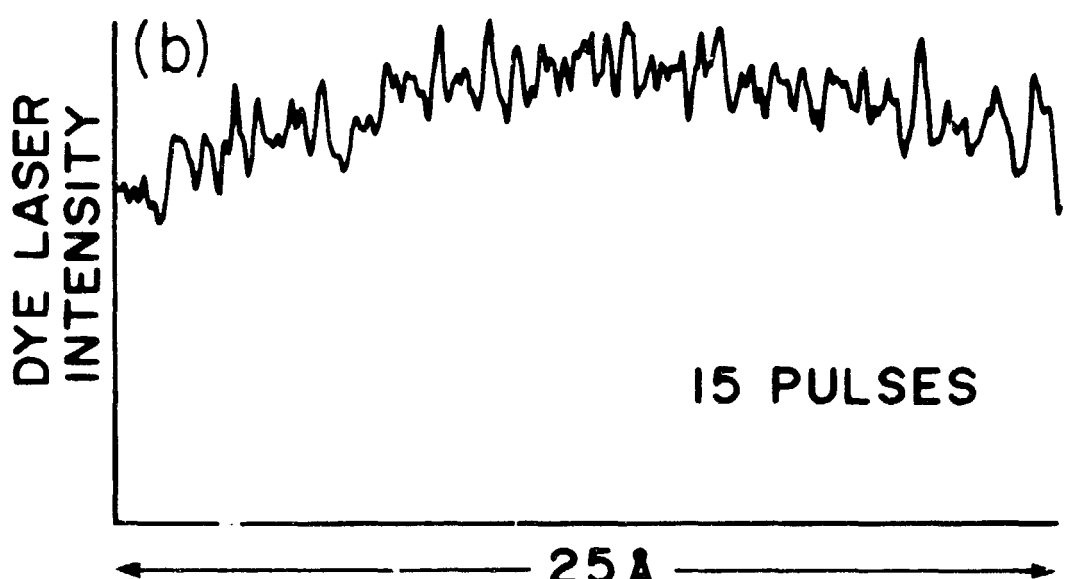
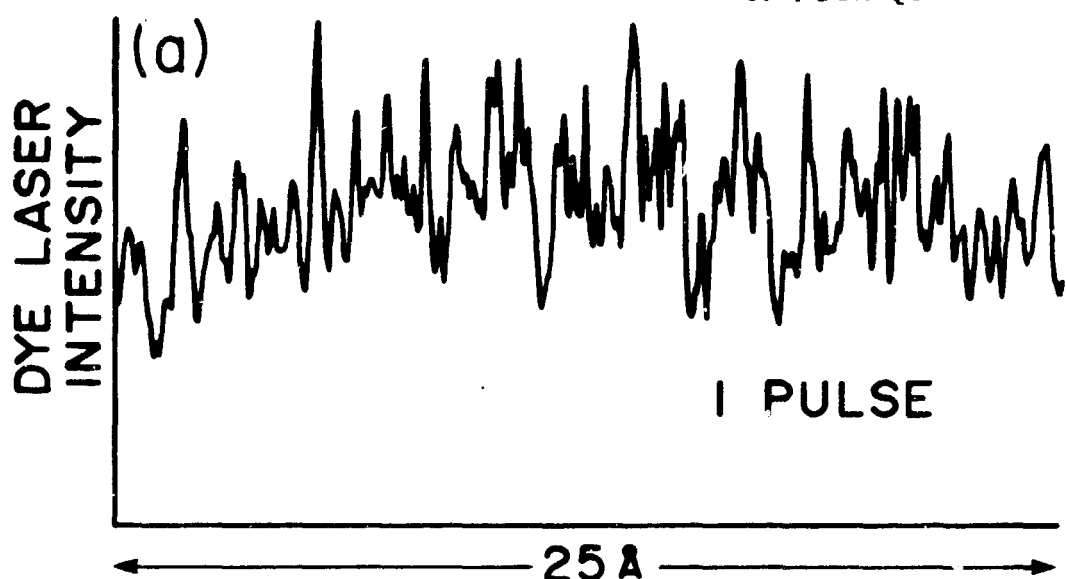


Fig. 3.1. Dye laser spectra recorded by the OMA for 1 pulse (a), and for average of 15 pulses (b).

### 3.2 Normalization by a Reference

Although averaging the CARS signals from a large number of successive laser pulses corrects many of the spectral and amplitude errors in single- and multichannel CARS spectra, it does not account for systematic errors caused by laser intensity drift and the dye laser efficiency dependence on  $\omega_S$ . In addition, averaging is time consuming in the scanning technique and is impossible where time-resolved measurements are required. An attractive alternative is to normalize the signal from each shot in such a way as to make it independent of both the intensities and spectral characteristics of the input laser beams. Several different normalization schemes will be discussed in this section, and a complete description of the normalization done in this work will be presented.

The most straightforward approach to normalizing a CARS signal is to record the pump and dye laser intensities for each shot, and then divide the CARS signal by the appropriate product. For single-channel scanning, the normalized CARS signal is

$$I_A^{\text{norm}}(\omega_L + \theta) = \frac{I_A(\omega_L + \theta)}{I_L^2(\omega_L) \cdot I_S(\omega_L - \theta)},$$

where  $I_A(\omega_L + \theta)$  is the uncorrected, single-shot CARS intensity at shift  $\theta$ , and  $I_L(\omega_L)$  and  $I_S(\omega_L - \theta)$  are the intensities of the pump laser and narrow-bandwidth dye laser, respectively. In the multichannel technique the entire dye laser spectrum must be recorded in a single pulse, in which case the normalized signal is

$$I_A^{\text{norm}}(\omega_L + \theta_i) = \frac{I_A(\omega_L + \theta_i)}{I_L^2(\omega_L) \cdot I_S(\omega_L - \theta_i)},$$

where  $I_A(\omega_L + \theta_i)$  and  $I_S(\omega_L - \theta_i)$  are the intensities of the spectral elements corresponding to a Raman shift of  $\theta_i$  in the broad-band CARS and dye laser spectra, respectively. This normalization must be performed on the signal from each resolution element of the OMA. The pump laser intensity is the same for all  $\theta_i$  and can be neglected if only spectral information is required; if accurate intensities are also desired it must be included.

Although this normalization procedure is fairly straightforward, experience has shown that it is inadequate when dealing with nonlinear interactions. The output of most lasers consists of many modes that fluctuate in intensity during the course of a single pulse and are therefore difficult to resolve using conventional techniques. The exact temporal, spectral, and spatial relationships between these modes are of critical importance in determining the efficiency of a nonlinear mixing process, however, so that division by time-averaged (over the duration of the pulse) signal intensities fails to account for the observed signal intensity fluctuations.

A better, commonly used approach to the normalization problem is to pick off a portion of the input laser beams and mix them in another nonlinear medium. Thus, any inter-mode mixing that takes place in the sample should be accurately reproduced in the reference as well. If the reference medium is chosen to have no resonant features in or near the spectral range of interest, the CARS signal will be generated entirely by the nonlinear response of the electrons to the applied fields, so that

$$I_A^{\text{ref}}(\omega_L + \theta) \propto |x_{\text{NR}}^{(3)}|^2 I_L^2(\omega_L) I_S(\omega_L - \theta),$$

where  $\chi_{NR}^{(3)}$  is the nonresonant susceptibility and is independent of  $\theta$ . An atomic gas such as argon makes a good reference medium; although the nonresonant susceptibility is small compared to the resonantly enhanced Raman susceptibility, adequate signal can be generated by increasing the pressure of the gas. With a reference of this type, the normalized signals are

$$I_A^{\text{norm}}(\omega_L + \theta) = \frac{|\chi^{(3)}(\theta)|^2 I_L^2(\omega_L) I_S(\omega_L - \theta)}{|\chi_{NR}^{(3)}|^2 I_L^2(\omega_L) I_S(\omega_L - \theta)}$$

for single-channel scanning, and

$$I_A^{\text{norm}}(\omega_L + \theta_i) = \frac{|\chi^{(3)}(\theta_i)|^2 I_L^2(\omega_L) I_S(\omega_L - \theta_i)}{|\chi_{NR}^{(3)}|^2 I_L^2(\omega_L) I_S(\omega_L - \theta_i)}$$

for multichannel detection.

This type of normalization is easily performed in single-channel experiments, since one simply divides the signal generated in the sample by that generated in the reference. With multichannel detection, however, this is complicated by the necessity of exactly aligning the signal and reference spectra so that the spectral component in a given channel of the signal spectrum is divided by the same spectral component of the reference spectrum. Two types of spatial error in the detected spectra occur to make this task nearly impossible: (1) there may be a slight registration error between the two spectra, so that one is shifted by a few channels with respect to the other; and (2) spatial distortions within the spectra occur due to errors introduced by the concave diffraction

ORIGINAL IMAGE  
OF POOR QUALITY

grating and OMA so that, even if there is exact alignment between the two spectra at one place in the field, they are mismatched in frequency elsewhere. In addition to these registration errors, spatial errors in the optics and camera also distort the CARS lineshapes. In practice, the normalization that is performed is

$$I_A^{\text{norm}}(\omega_L + \theta_i) = \frac{[I_A(\omega_L + \theta_i)]_k}{[I_A^{\text{ref}}(\omega_L + \theta_j)]_k},$$

where  $[I_A(\omega_L + \theta_i)]_k$  is the signal from the  $k^{\text{th}}$  channel of the OMA and corresponds to Raman shift  $\theta_i$ . Spatial distortions make it difficult to ensure that  $i = j$  and, for a dye spectrum with features as sharp as in Fig. 3.1(a), errors of only a few channels will be important.

Because the goal of the present work is to measure the temperature of a specific gas rather than to produce rigorously accurate spectra, it is possible to use a different type of normalization procedure in which the nonresonant reference gas is replaced by the same resonant gas used in the sample region. Thus, for identical conditions of temperature and pressure, two identical spectra should be produced, one from the sample and one from the reference. Instead of performing a channel-by-channel normalization, the spectra are simply compared on the basis of the integrated signal from corresponding Raman lines. Spatial distortions and registration errors do not constitute a problem in this scheme because the individual rotational Raman lines in each spectrum are well resolved. The ratio of signals from

CHECK FOR  
OF POOR QUALITY

a particular line will be

$$F_J(P, T) = \frac{\int I_A^J(\omega_L + \theta) d\theta}{\int [I_A^J(\omega_L + \theta)]^{ref} d\theta} .$$

Any departure of  $F_J(P, T)$  from unity should reflect differences in the pressure and/or temperature of the sample and reference gases. The integrated CARS signal from a particular line is

$$\int I_A^J(\omega_r + \theta) d\theta \approx \int_{\omega_J-x}^{\omega_J+x} I_L^2(\omega_L) I_S(\omega_L - \theta) |x^{(3)}(\omega_J - \theta)|^2 d\theta ,$$

where  $\omega_J$  = frequency of the  $J^{\text{th}}$  rotational Raman line and  $x \gg \Gamma_J$ . Depending on the relative widths of the Raman line and spectral structure in the dye laser,  $I_S(\omega_L - \theta)$  may show strong fluctuations over the range of integration or may be relatively constant. By comparing only the integrated line strengths of the sample and reference spectra, however, it becomes unnecessary to obtain detailed information about the dye spectrum, since this is taken care of in the nonlinear mixing process itself.

The procedure for determining the sample gas temperature is as follows: The reference gas is held at fixed temperature and pressure, for which the theoretical integrated line-intensity distribution is calculated. The single shot experimental reference spectrum will, in general, differ from the calculated distribution because of the nonuniform dye laser spectrum. Therefore, each of the Raman lines in the experimental reference spectrum is multiplied by the appropriate factor to bring it into agreement with the intensity of the corresponding calculated line.

These same correction factors are then applied to the sample spectrum, since a given Raman line in both spectra will depend on the same dye laser spectral structure. The corrected, integrated line-intensity distribution of the sample gas can then be fit to calculated distributions to find the temperature. The principal difficulty with this approach is the variation of the Raman linewidth with temperature and pressure; this will be discussed in Section 4.

### 3.3 Optical Arrangement and Alignment

The pump laser beam at frequency  $\omega_L$  and the broadband, Stokes-shifted dye laser beam at frequency  $\omega_S$  are both derived from a high power, pulsed Nd:YAG laser. The laser consists of an oscillator and single amplifier stage which emit fundamental radiation at  $1.06 \mu\text{m}$  in 15 nsec pulses with a maximum energy of 750 mJ per pulse when operating at the design repetition rate of 10 Hz. The  $1.06 \mu\text{m}$  radiation is frequency doubled via a second-order nonlinear process in a KD<sup>\*</sup>P crystal to produce up to 250 mJ/pulse at 532 nm. This second-harmonic radiation is mixed with the residual fundamental in a second nonlinear crystal to produce the third-harmonic radiation at 355 nm. The full-power energy distribution in the second- and third-harmonic beams is about 160 mJ/pulse and 110 mJ/pulse, respectively.

The second harmonic of the YAG laser is used as the pump beam in the CARS experiment, and its linewidth therefore determines the resolution of the experiment. For the present work the Nd:YAG oscillator was operated without an intra-cavity etalon, so many longitudinal cavity modes could oscillate simultaneously; in this case the manufacturer specifies a fundamental linewidth of  $0.5 \text{ cm}^{-1}$  FWHM. This parameter was not measured in the present work and is likely to vary from pulse to pulse, but a

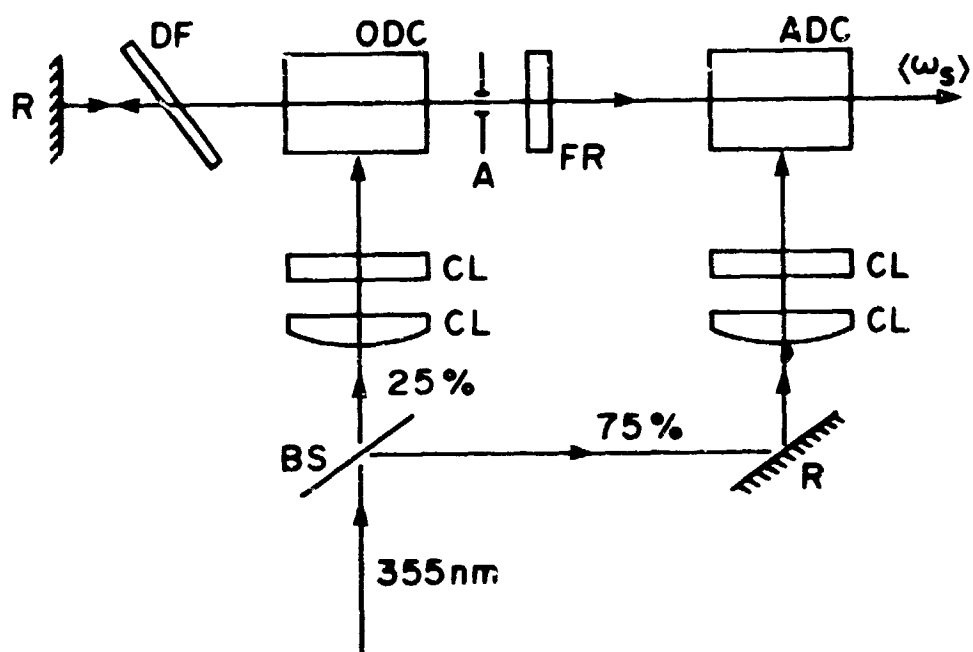


Fig. 3.2. Schematic lay-out of the broadband dye laser constructed for the experiment. The symbol code is: BS, beamsplitter; R, 100% reflector; CL, cylindrical lens; DF, dielectric filter; ODC, oscillator dye cell; ADC, amplifier dye cell; A, aperture; FR, front reflector of dye laser cavity.

value in this range is consistent with the experimental results.

The third harmonic is used to pump a broad-bandwidth dye laser that was constructed for this project. The dye laser consists of a transversely pumped oscillator and single-stage, transversely pumped amplifier and is shown schematically in Fig. 3.2. Two separate flow systems were used to circulate the coumarin 500 dye (in ethanol) through the dye cells since the oscillator and amplifier stages require different dye concentrations. The bandwidth of the emission was unrestricted by any of the usual line narrowing devices (prisms, diffraction gratings, etalons, etc.), while the center frequency of the band was adjusted by angle tuning a sharp, edge-cut, multilayer dielectric filter placed inside the cavity. When tuned to a center wavelength near 532 nm, the bandwidth was approximately 40 Å at the half-power points. The pulse duration of the dye laser was about 10 nsec and the maximum attainable energy was ~10 mJ/pulse.

The experimental arrangement is shown in Fig. 3.3. The horizontally polarized dye laser beam, denoted  $\langle\omega_S\rangle$ , and the vertically polarized pump beams ( $\omega_L$ ) are focused by a 30 cm focal length lens into the sample region (S). The input beams, along with the CARS beam generated in the sample, are recollimated by the second 30 cm lens. The CARS beam is picked off and directed into the spectrograph, while the pump and Stokes-shifted beams are refocused into the reference region where the second CARS signal is generated. The two horizontally polarized CARS signals are directed through polarizers that reject scattered 532 nm light and are then focused to pass side by side through the 100 μm wide horizontal entrance slit of the spectrograph. The two signals are vertically dispersed in the spectrograph and are imaged side by side onto the OMA.

Alignment of the beams to the correct phase-matching angles is

ORIGINAL PAGE IS  
OF POOR QUALITY

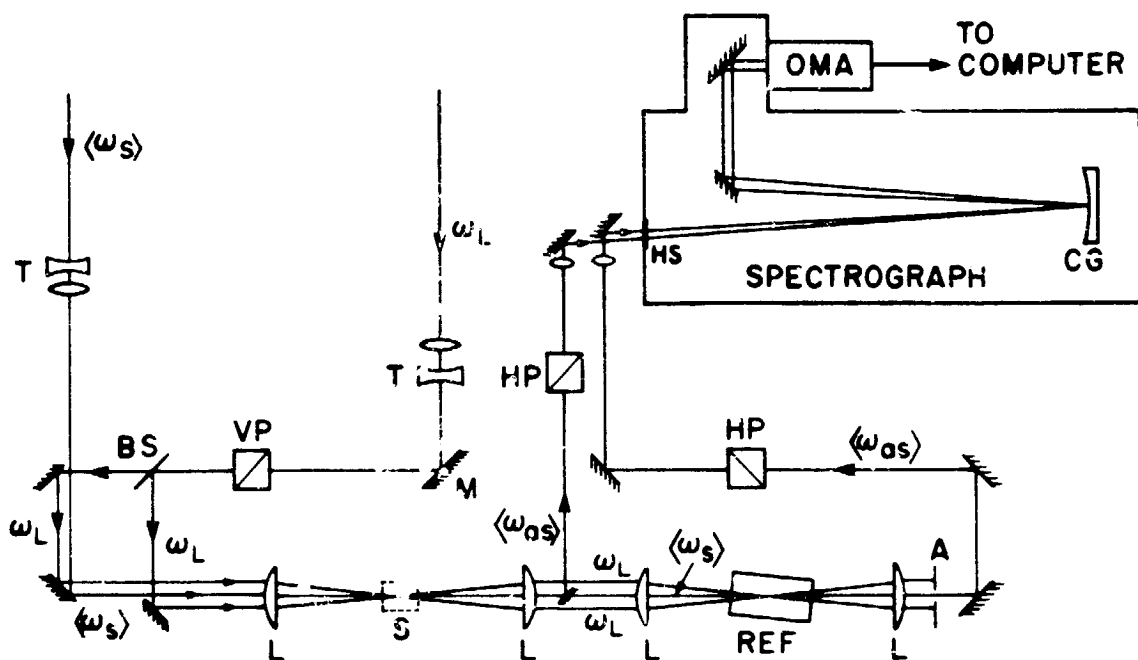


Fig. 3.3. Schematic lay-out of the experimental apparatus. The symbol code is: T, telescope; BS, beamsplitter; VP, vertical-pass polarizer; L, lens; HP, horizontal-pass polarizer; HS, horizontal slit; CG, concave grating; S, sample gas region; REF, reference gas region.

achieved by making sure that the beams are parallel and properly spaced before the 30 cm lenses are installed. With the lenses in place, the beams are checked for spatial overlap at the foci with a 100  $\mu\text{m}$  diameter pinhole. The telescopes, T, are used to bring the dye and pump beams to the same diameter ( $\sim 7$  mm) and to make fine adjustments on the beam divergences to ensure that all three beams are brought to focus at the point of overlap. Although the alignment is normally done at low power, it is adequate to ensure that a signal will appear when the power is increased, at which point the signal intensity can be maximized by making fine angular adjustments on the beams. When properly aligned, the signals from the sample and reference regions can be maximized simultaneously even though there is no provision for individual alignment.

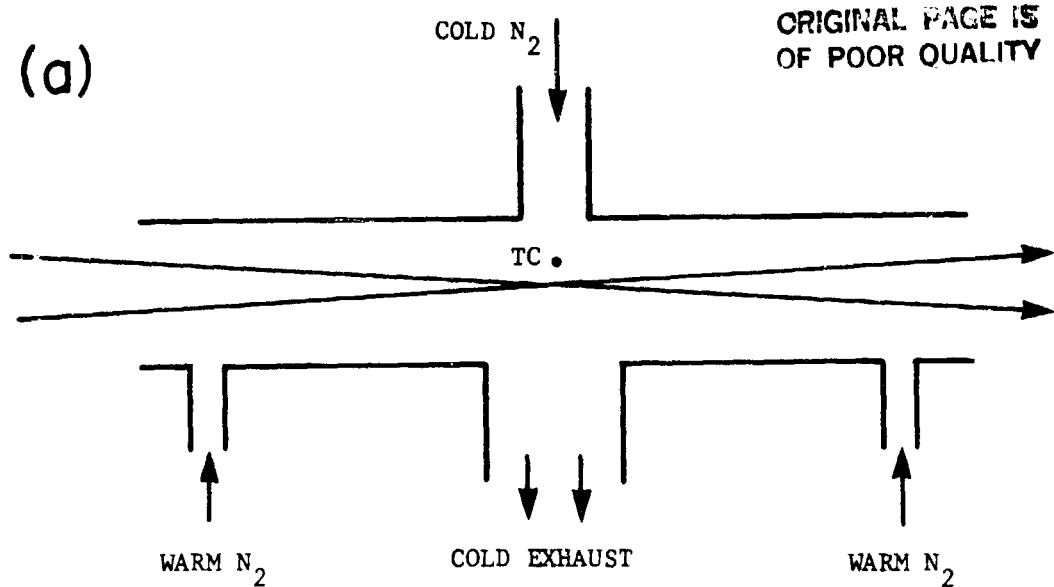
The series configuration for the sample and reference regions was chosen over the parallel approach in which portions of the input beams are separated from the main beams and focused separately into the reference cell to avoid the loss of signal brought about by splitting the beams. When a nonresonant reference is used, only a small fraction of the input beams need be focused into the reference cell since the signal can be boosted by increasing the pressure in the cell; this is undesirable with a resonant reference because the Raman linewidth increases linearly with pressure, making comparison to the atmospheric pressure sample difficult. Splitting the beams evenly between the signal and reference regions would mean a loss of signal by a factor of 8 compared to the series approach. In principle, there is a danger of the dye laser spectrum being perturbed by the mixing in the signal region, resulting in a distorted CARS spectrum from the reference, but in practice the beam energies are kept low enough so that this is not a significant effect (CARS signal intensity is  $< 10^{-7}$  of the input dye laser intensity).

The spectrograph used for the room and low temperature work consists of a single 1 m focal length, concave, holographically ruled grating. It has a dispersion of  $1530 \text{ cm}^{-1}/\text{m}$  in the focal plane in the spectral region of interest. The spectra could be imaged 1:1 onto the OMA or magnified by a factor of two, depending on the desired range of coverage. The grating in this instrument is not optimized for use as a spectrograph and is probably responsible for most of the distortion observed in the spectra on the OMA. Fortunately, use of the resonant reference eliminates this as a serious source of difficulty.

All of the experimental spectra were taken with the sample and reference regions flooded with pure  $\text{N}_2$  gas. Although strong signals were easily obtained in air, interference from neighboring  $\text{O}_2$  Raman lines made quantitative interpretation of the  $\text{N}_2$  CARS spectra difficult. An additional difficulty with an air environment is the presence of dust particles that drift into the laser focal volumes and spark, resulting in a bright, broad-band signal at the detector. In order to maintain dust-free, 100%  $\text{N}_2$  environments, open-end tubes were placed coaxially with the laser beams at the sample and reference mixing regions. Clean  $\text{N}_2$  was then flowed gently into each tube at its center, thus maintaining a steady outward flow of  $\text{N}_2$  from the tube ends. Thermocouples were mounted in each tube near the laser beam waists to monitor the gas temperature. For the room temperature measurements, the sample and reference gas temperatures agreed to within 1 K without any temperature control.

An open-end cell was also used in the low temperature measurements to avoid the use of double windows that would have been required with a sealed cell. A schematic of the cell is shown in Fig. 3.4(a).  $\text{N}_2$  gas

(a)



(b)

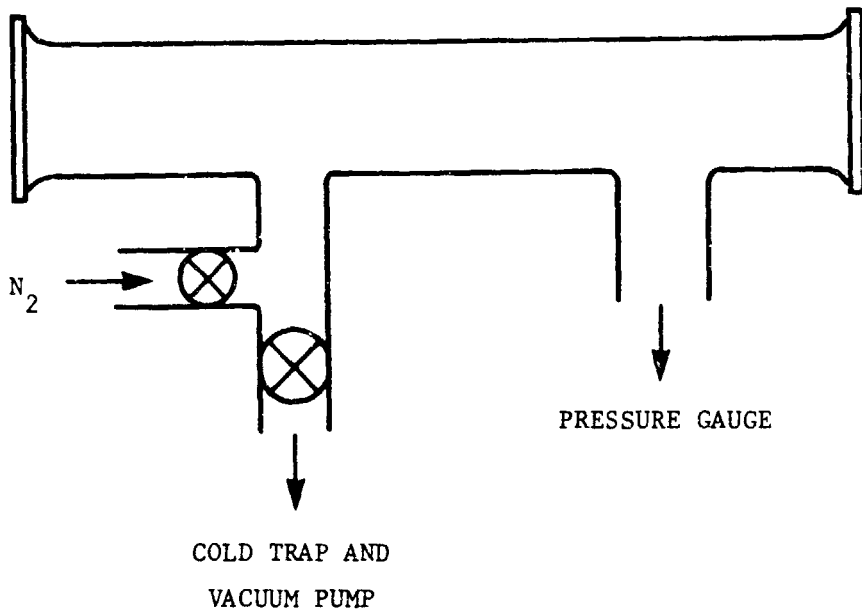


Fig. 3.4. The optical cells used in recording the CARS spectra of N<sub>2</sub> at low temperature (a) and low pressure (b).

from a high pressure tank was passed through copper coils immersed in LN<sub>2</sub>, through a 1 m insulated plastic tube, and was then blown across the cell and out the opposing port. The cell was constructed of copper tubing and fittings and was wrapped in foam rubber to alleviate the problem of water condensation at low temperature. A 100% N<sub>2</sub> atmosphere was maintained in the cell by flooding the ends of the tubes with room temperature N<sub>2</sub> gas. Without this N<sub>2</sub> purge, air was drawn into the tube ends and resulted in scattering of the laser beams from frozen water vapor at low temperatures. A copper/constantan thermocouple (3 mil wire) was mounted in the cell to monitor the N<sub>2</sub> temperature. The cell position was adjusted so that the thermocouple junction was ~1 mm above the focal point of the beams (closer positioning resulted in spurious readings due to the laser beams). The temperature at the mixing region was adjusted by varying the gas flow rate. Although this system does not provide any means of active temperature control, the temperature reading from the thermocouple was found to stabilize at a given flow rate long enough to make a series of measurements. Data in the range of 135 to 250 K were obtained with this system.

The low pressure measurements were made with the 19.5 cm long optical cell shown in Fig. 3.4(b). Single-shot spectra could be obtained down to a total pressure of about 40 Torr, so the pressure over the entire range of interest was conveniently measured with a mercury manometer. The high pressure measurements were made with a stainless-steel cell having an optical path length of 100 cm. Pressures above 1 atm were measured with a single gauge calibrated in 5 psig increments from 0 to 200 psig.

### 3.4 The Optical Multichannel Analyzer

The optical multichannel detector (OMA) used in this project is a digitally controlled television camera (silicon diode array vidicon) with a single-stage intensifier. The maximum scanned area is  $1.25 \times 1.25 \text{ cm}^2$  and the highest resolution pixel size is  $25 \mu\text{m}$  in diameter, although any number of adjacent pixels can be grouped together to establish scan formats of lower resolution. The video output is converted to digital form by a 14 bit analog-to-digital converter and is passed on to a microcomputer that is used to establish the desired scan format as well as to collect and display the data.

In the present experiment the camera is scanned in two one-dimensional tracks of 499 channels each, as shown in Fig. 3.5. Each channel consists of a horizontal strip 150 to 200 pixels wide and 1 pixel tall. The integrated signal from each channel represents a single point in the one-dimensional track. This format provides maximum resolution in the vertical direction of dispersion and still collects all of the signal spread out in the horizontal direction due to astigmatism in the concave grating. The  $499 \times 1$  channel arrays from each track are stored separately as independent pictures. The scanning rate selected for most of this work was  $40 \mu\text{sec}/\text{channel}$ , so the time required for one complete sweep of both tracks (corresponding to a single frame) is 39.9 msec, for a rate of 25 frames per second.

The characteristic of the OMA that is most troublesome for pulsed instantaneous measurements is image lag, an inherent problem with many types of television tubes whereby the optical signal impressed upon the target is not fully erased by a single sweep of the read beam. This characteristic gives rise to two problems: signal holdover and nonlinear

ORIGINAL PAGE IS  
OF POOR QUALITY

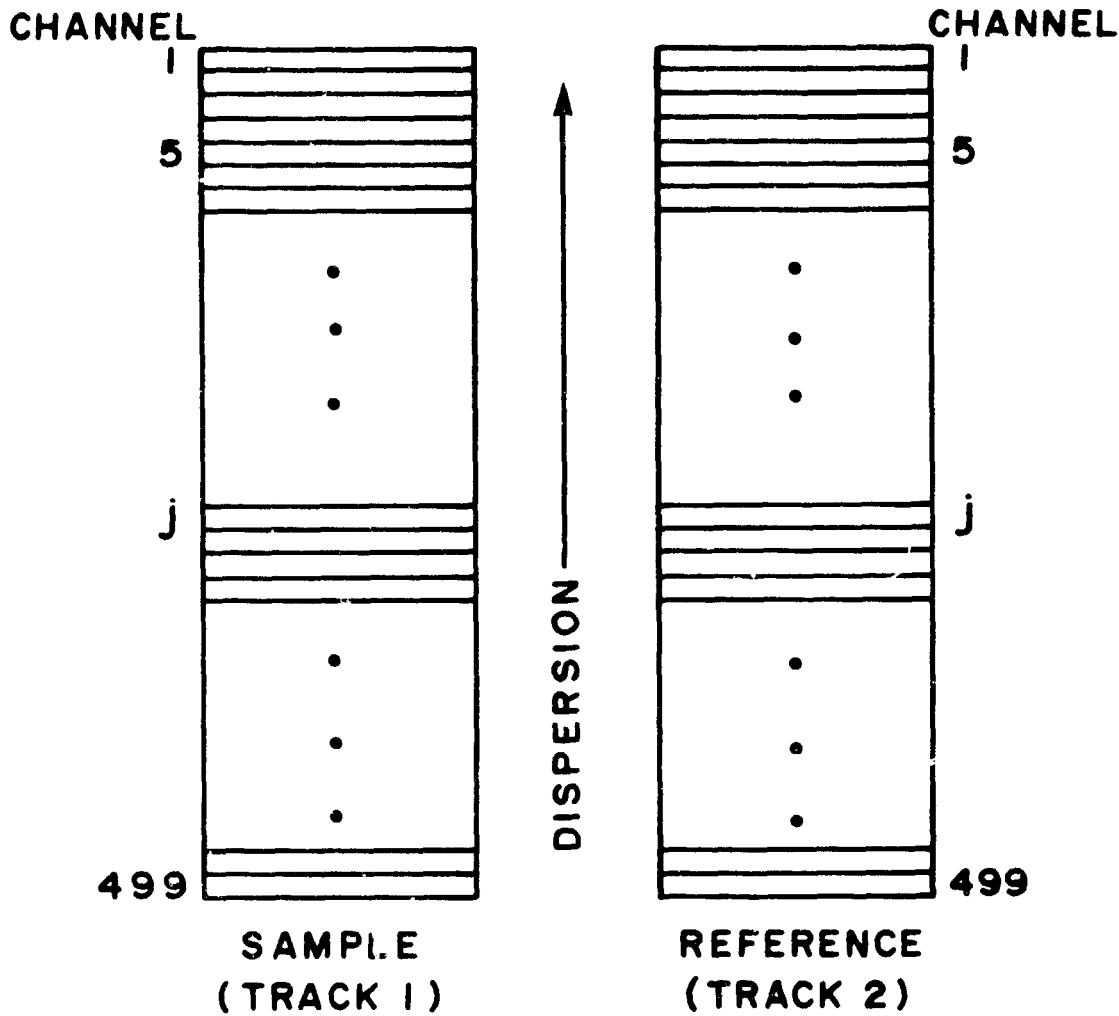


Fig. 3.5. The two-track scan format used with the OMA to simultaneously record the sample gas and reference gas spectra. Each track consists of 499 channels spaced on  $25 \mu$  centers.

response (Crowell and Labuda, 1971). Because the signal is not completely erased in one or even several sweeps, the signal recovered from any scan will contain contributions from several preceding optical pulses. With the laser operating at 10 Hz and the OMA scanning at a rate of 25 frames/s, there will be only 2.5 scans between laser pulses and significant signal hold over does occur. Thus, the signal from any shot does not represent a truly instantaneous spectrum. The second problem has to do with the fact that the signal is not read off the target linearly; it is a common feature of vidicons that the brighter signals tend to come off faster than the weak signals, so that after a given number of scans there will be an error in the intensity ratio of a strong spectral line to a weak line. This shows up dramatically in the CARS spectrum of N<sub>2</sub> in which the intensities of alternate peaks are in the ratio of 4:1. Figure 3.6(a) shows the integrated signal from a single line as a function of intensity with the laser operating at 10 Hz. For these conditions it should be noted that the signal holdover from previous shots tends to offset the inherent nonlinearity so that the overall response is fairly linear over an entire decade; without this accidental cancellation, the nonlinearity would be considerably worse.

The solutions to these two problems are easily implemented but tend to degrade the overall performance of the system. The problem of signal holdover can be eliminated by increasing the time between laser pulses until no significant signal overlap occurs. Although the laser flash lamps must fire at a steady 10 Hz rate because of thermal lens effects in the laser rods, it is possible to gate the Pockels cell so that lasing action only occurs for every N<sup>th</sup> lamp discharge. It was found that allowing the laser to pulse only every 1.6 s (N = 16) was

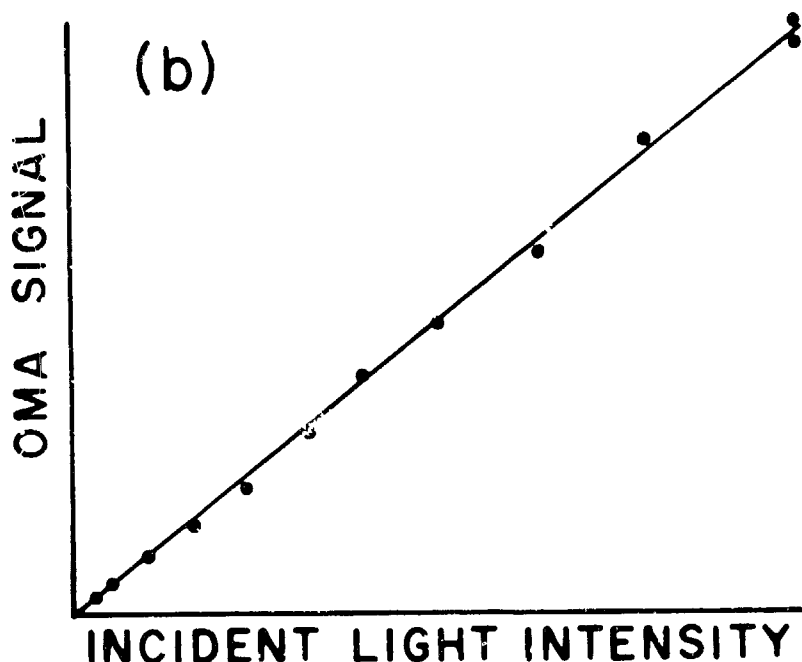
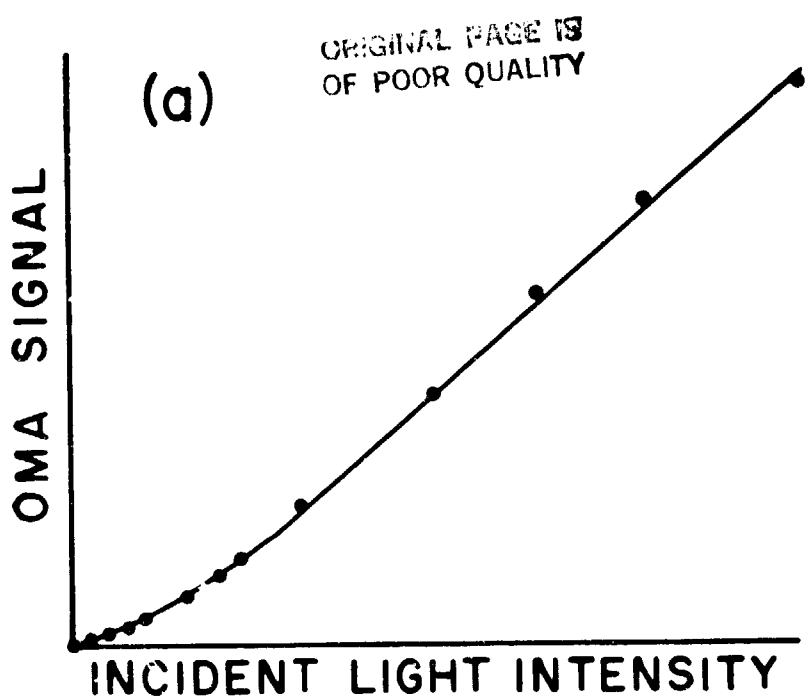


Fig. 3.6. OMA signal as a function of incident light intensity. In (a), the OMA was scanned once after each laser pulse; the laser repetition rate was 10 Hz. In (b), the OMA was scanned 10 times after each laser pulse; the laser repetition rate was .63 Hz.

adequate to ensure that all the signal from one pulse was erased before the next pulse arrived. The nonlinearity problem was solved by scanning the target many times following the arrival of a signal pulse, and summing the signal from successive scans to form a single data array for each track. It was found that scanning the target 10 - 15 times was adequate to ensure that all the signal was read off the target. The camera linearity was greatly improved by employing this scan format, as seen in Fig. 3.6(b), which shows the integrated detected signal strength as a function of incident light intensity and was obtained using 10 reread frames.

The price paid for linear, single-shot detection is a slower data acquisition rate and noisier signals. The reread frames ensure linear response by extracting all the signal from the target but tend to accumulate background counts due to the thermally generated dark noise in the target and due to electronic noise introduced by the A/D conversion process. Although much of this can be subtracted away, there is still a noticeable degradation in the signal/noise of the final spectra.

#### 4. CALCULATION OF ROTATIONAL CARS SPECTRA AND INTENSITY DISTRIBUTIONS

The temperature-fitting procedure used to analyze the CARS spectra requires comparison of the distribution of integrated power in the peaks of an experimental spectrum with the theoretical distributions calculated over a range of temperatures. Therefore, the desired calculated quantities are

$$A_J = \frac{\int I_A^J(\omega_A) d\omega_A}{\sum_J \int I_A^J(\omega_A) d\omega_A} = \frac{\overline{I_A^J}}{\sum_J \overline{I_A^J}}, \quad (4.1)$$

where  $I_A^J(\omega_A)$  is the CARS power as a function of frequency in the vicinity of the  $J^{th}$  Raman line, and the integration extends midway to the adjacent peaks on either side of the peak centered at  $\omega_J$ . The denominator is simply the total CARS power in all lines and is included as a normalization factor to allow comparison with experimental distributions. This chapter is primarily concerned with the calculation of the terms  $\overline{I_A^J}$ .

##### 4.1 Modification of the CARS Theory to Include a Pump Laser with

###### Finite Linewidth

In the CARS theory developed in Section 1.1, it was assumed that the applied electric field consisted of three discrete frequency components, e.g., the outputs of three perfectly monochromatic lasers.

ORIGINAL PAGE IS  
OF POOR QUALITY

In practice, however, lasers have finite spectral linewidths, in which case Eq. (1.8) must be modified as follows:

$$I(\omega_4) \propto \left| \int \int d\omega_1 d\omega_2 d\omega_3 |x^{(3)}(\omega_4; \omega_1, \omega_2, \omega_3)|^2 I_1(\omega_1) I_2(\omega_2) I_3(\omega_3) \times \delta(\omega_4 - \omega_1 - \omega_2 + \omega_3) , \quad (4.2)$$

where  $I_i(\omega_i)$  is the power distribution with frequency of laser i. A complete discussion of this equation is given in the literature (Yuratich, 1979; St. Peters, 1979; St. Peters, 1980), but the basic assumption is that the laser outputs consist of densely spaced, perfectly monochromatic, independent modes, in which case it is possible to write the total CARS intensity at  $\omega_4$  as the sum of intensities due to all combinations of  $\omega_1$ ,  $\omega_2$ , and  $\omega_3$  satisfying the condition  $\omega_4 = \omega_1 + \omega_2 - \omega_3$ . This assumption is not fulfilled in real lasers, but it is a useful working approximation; an exact treatment that takes into account the time-varying frequencies, divergences and degree of coherence of all the laser modes is impossible.

In the ideal broadband CARS experiment the dye laser is assumed to have a flat spectrum over the range of interest, so the integration over  $\omega_3$  can be performed in Eq. (4.2) using  $I_3(\omega_3) = I_3$  and the delta function to obtain

$$I_4(\omega_4) \propto I_3 \left| \int \int d\omega_1 d\omega_2 |x^{(3)}(\omega_4; \omega_1, \omega_2, \omega_4 - \omega_1 - \omega_2)|^2 I_1(\omega_1) I_2(\omega_2) . \quad (4.3)$$

ORIGINAL PAGE IS  
OF POOR QUALITY

For the special case in which a genuinely monochromatic pump laser provides the fields at  $\omega_1$  and  $\omega_2$  (laser linewidth  $\ll$  Raman linewidths), Eq. (4.3) can be evaluated using  $I_1(\omega_1) = I_1 \delta(\omega_1 - \omega_L)$  and  $I_2(\omega_2) = I_2 \delta(\omega_2 - \omega_L)$  to obtain

$$I(\omega_4) \propto I_1 I_2 I_3 |x^{(3)}(\omega_4; \omega_L, \omega_L, \omega_4 - 2\omega_L)|^2 ,$$

in which case the integrated CARS power is simply

$$\bar{I}_4 \propto I_1 I_2 I_3 \int d\omega_4 |x^{(3)}(\omega_4; \omega_L, \omega_L, \omega_4 - 2\omega_L)|^2 . \quad (4.4)$$

In general, however, the lasers are not monochromatic and the integrated CARS power is given by

$$\bar{I}_4 \propto I_3 \int d\omega_4 \left[ \int d\omega_1 d\omega_2 |x^{(3)}(\omega_4; \omega_1, \omega_2, \omega_4 - \omega_1 - \omega_2)|^2 I_1(\omega_1) I_2(\omega_2) \right] .$$

The nonlinear susceptibility at a given wavelength is the sum of all resonant and nonresonant terms, so that

$$x^{(3)}(\omega_4; \omega_1, \omega_2, \omega_4 - \omega_1 - \omega_2) = x_{NR} + \sum_J x_J^{(3)}(\omega_4; \omega_1, \omega_2, \omega_4 - \omega_1 - \omega_2) ,$$

where

$$\begin{aligned} x_J^{(3)}(\omega_4; \omega_1, \omega_2, \omega_4 - \omega_1 - \omega_2) &= K_J \left\{ \frac{1}{\omega_J - (\omega_4 - \omega_2) - i\Gamma_J} \right. \\ &\quad \left. + \frac{1}{\omega_J - (\omega_4 - \omega_1) - i\Gamma_J} \right\} . \end{aligned} \quad (4.5)$$

and

$$K_J = \frac{N}{12\pi} \frac{c^4 \Delta}{\omega_s^4} J \left( \frac{\partial \sigma}{\partial \Omega} \right)_J$$

This expression explicitly provides for the possibility of simultaneous Raman resonances in  $\omega_4 - \omega_2$  ( $= \omega_1 - \omega_3$ ) and  $\omega_4 - \omega_1$  ( $= \omega_2 - \omega_3$ ). The factors  $K_J$  contain temperature-dependent and  $J$ -dependent terms as well as all constants associated with  $\chi_{\text{RAM}}^{(3)}$ ; expressions for the  $K_J$ 's were derived from Eq. (1.18). In the case of a monochromatic pump laser,  $\omega_1 = \omega_2 = \omega_L$  and Eq. (4.5) collapses to a single term.

In a true four-color CARS experiment ( $\omega_1 \neq \omega_2 \neq \omega_3$ ) it is unlikely that both terms in Eq. (4.5) will be on or near resonance simultaneously, in which case the off-resonant term can be lumped in with  $\chi_{\text{NR}}$ . In a three-color CARS experiment, however,  $\omega_1$  and  $\omega_2$  are simply different spectral components within the bandwidth of the same pump laser and both terms may be near resonance simultaneously, since  $\omega_1 - \omega_2 \stackrel{<}{\sim} \Gamma_L$  ( $\Gamma_L = \text{FWHM}$  of the pump laser linewidth; 0.5 to 1.0  $\text{cm}^{-1}$  in this work). Several treatments of the effect of finite laser linewidths on CARS spectra have appeared in the literature (Yuratich, 1979; St. Peters, 1979; St. Peters, 1980), but they include only one of the two possible resonance terms, in which case the resonant susceptibility is simply

$$\chi_J(\omega_4; \omega_1, \omega_2, \omega_4 - \omega_1 - \omega_2) = \frac{K_J}{\omega_J - (\omega_4 - \omega_2) - i\Gamma_J} .$$

The integrated line strengths corresponding to these two cases are

$$\begin{aligned} \overline{I}_4 \propto I_3 & \left[ \int d\omega_4 \left[ \int d\omega_1 d\omega_2 \left| \chi_{\text{NR}} + \sum_J K_J \left\{ \frac{1}{\omega_J - (\omega_4 - \omega_2) - i\Gamma_J} \right. \right. \right. \right. \right. \\ & \left. \left. \left. \left. \left. \left. + \frac{1}{\omega_J - (\omega_4 - \omega_1) - i\Gamma_J} \right\} \right|^2 \times I_1(\omega_1) I_2(\omega_2) \right] \right] \end{aligned} \quad (4.6)$$

for the double-resonance theory and

$$\overline{I_4} \propto I_3 \left\{ d\omega_4 \left[ \int d\omega_1 d\omega_2 \left| \chi_{NR} + \sum_J \left\{ \frac{K_J}{\omega_J - (\omega_4 - \omega_2) - i\Gamma_J} \right\} \right|^2 I_1(\omega_1) I_2(\omega_2) \right] \right\} \quad (4.7)$$

for the single-resonance case. Since the  $\chi_J^{(3)}$ 's in Eq. (4.7) are independent of  $\omega_1$ , the integration over  $\omega_1$  can be performed and Eq. (4.7) can be reduced to the same expression obtained for the case of a monochromatic pump laser [Eq. (4.4)], so that

$$\overline{I_4} \propto I_1 I_2 I_3 \left\{ dx \left| \chi_{NR} + \sum_J \left\{ \frac{K_J}{\omega_J - x - i\Gamma_J} \right\} \right|^2 \right\} \quad (4.8)$$

Thus, according to the single-resonance theory, the finite pump laser linewidth broadens the detected CARS lines but does not affect their integrated area.

The theoretical integrated intensity distributions as well as complete rotational CARS spectra have been calculated on a computer using both the single-resonance [Eq. (4.8)] and double-resonance [Eq. (4.6)] theories. The calculated distributions obtained with the two theories are somewhat different, but not enough to significantly influence the results of the temperature fits of the experimental data. The two types of calculated spectra also show subtle differences, but both correspond closely to experimental spectra and it is not possible to definitively prefer one theory over the other. Because the present experiments are not able to discriminate between the two theories, and

because the computational times required for evaluation of the triple integrals in Eq. (4.6) are very long, the simpler, monochromatic theory was used to calculate the integrated intensity distributions used in fitting the data to temperature.

The CARS signal produced by a given combination of  $\omega_1$ ,  $\omega_2$ , and  $\omega_3$  contains contributions from the nonresonant background and from all Raman resonances. Because these terms are all summed coherently, it is possible to have interferences between on- and off-resonance Raman contributions and between the Raman terms and the real, nonresonant background. The susceptibility due to an individual Raman line can be broken into real and imaginary parts, as follows:

$$\frac{K_J}{\omega_J - x - i\Gamma_J} = K_J \left\{ \frac{(\omega_J - x)}{(\omega_J - x)^2 + \Gamma_J^2} + \frac{i\Gamma_J}{(\omega_J - x)^2 + \Gamma_J^2} \right\}.$$

The real and imaginary lineshapes are plotted in Fig. 4.1. Although the imaginary part of the susceptibility falls off rapidly away from line center, the tails of the real part die off slowly and can contribute to the real, nonresonant background at nearby lines. The effect of this real background is to distort the observed CARS lineshapes away from the Lorentzian shapes observed in spontaneous Raman scattering. The resulting asymmetric lineshapes can be observed in the experimental CARS spectra shown in Figs. 4.2(b) and 4.3(b).

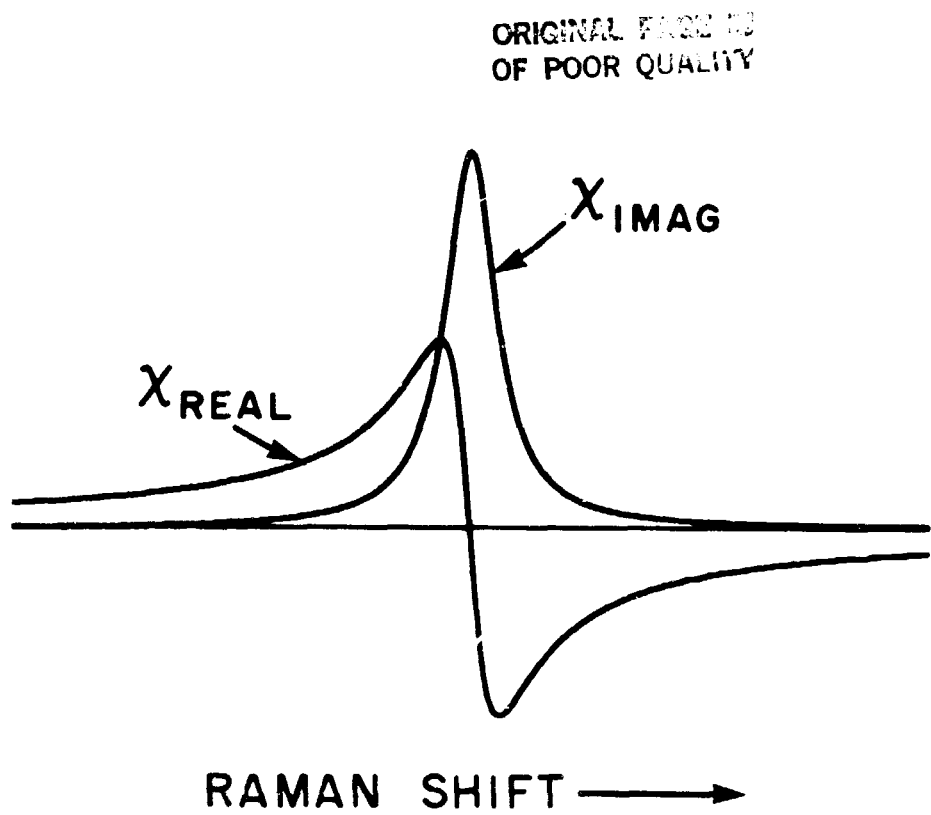


Fig. 4.1. Real and imaginary parts of the nonlinear susceptibility due to an isolated Raman resonance.

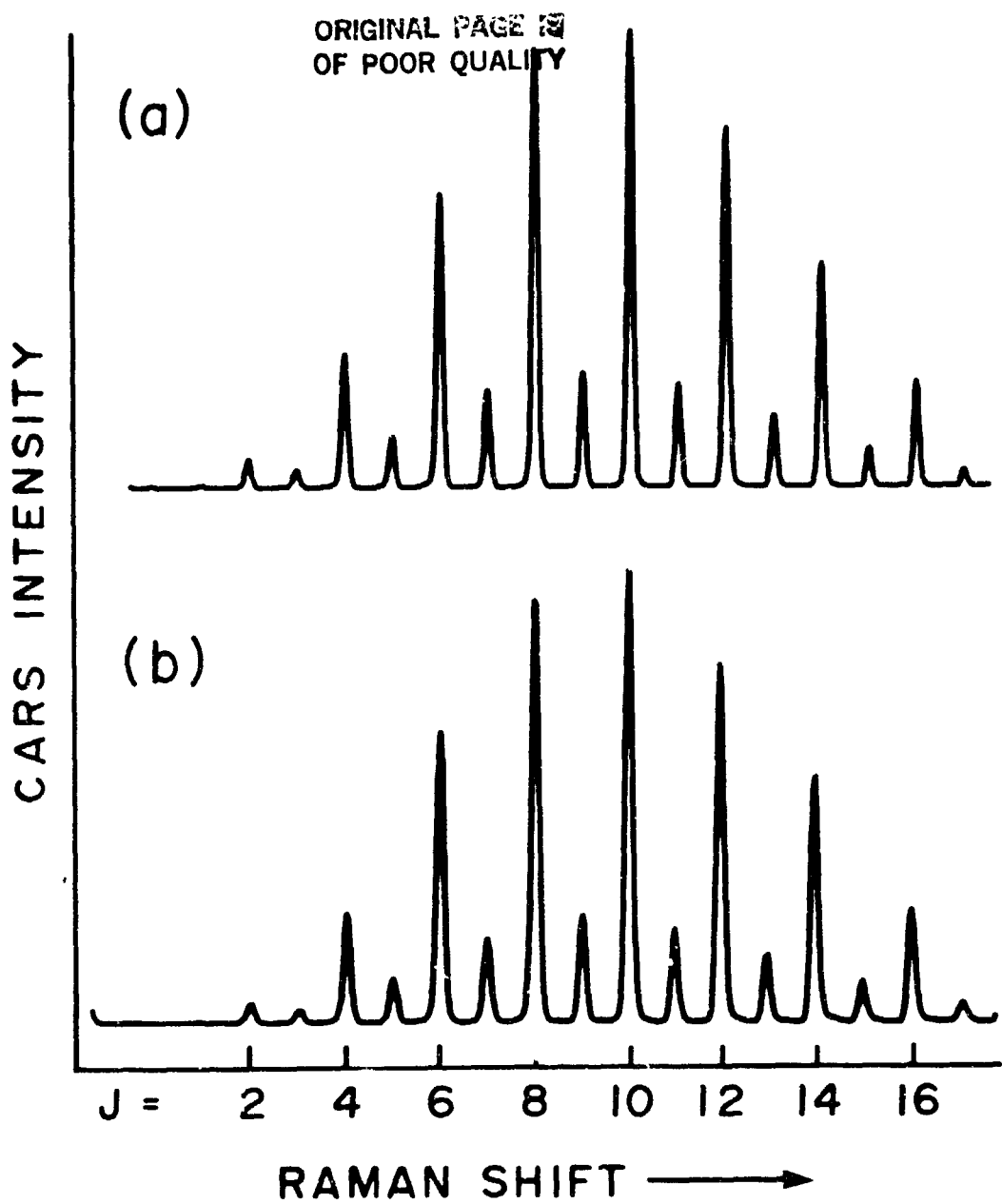


Fig. 4.2. Calculated (a) and experimental (b) CARS spectra of  $\text{N}_2$  at 296 K and 1 atm. The experimental spectrum is an average of the spectra from 200 consecutive laser firings.

ORIGINAL PAGE IS  
OF POOR QUALITY

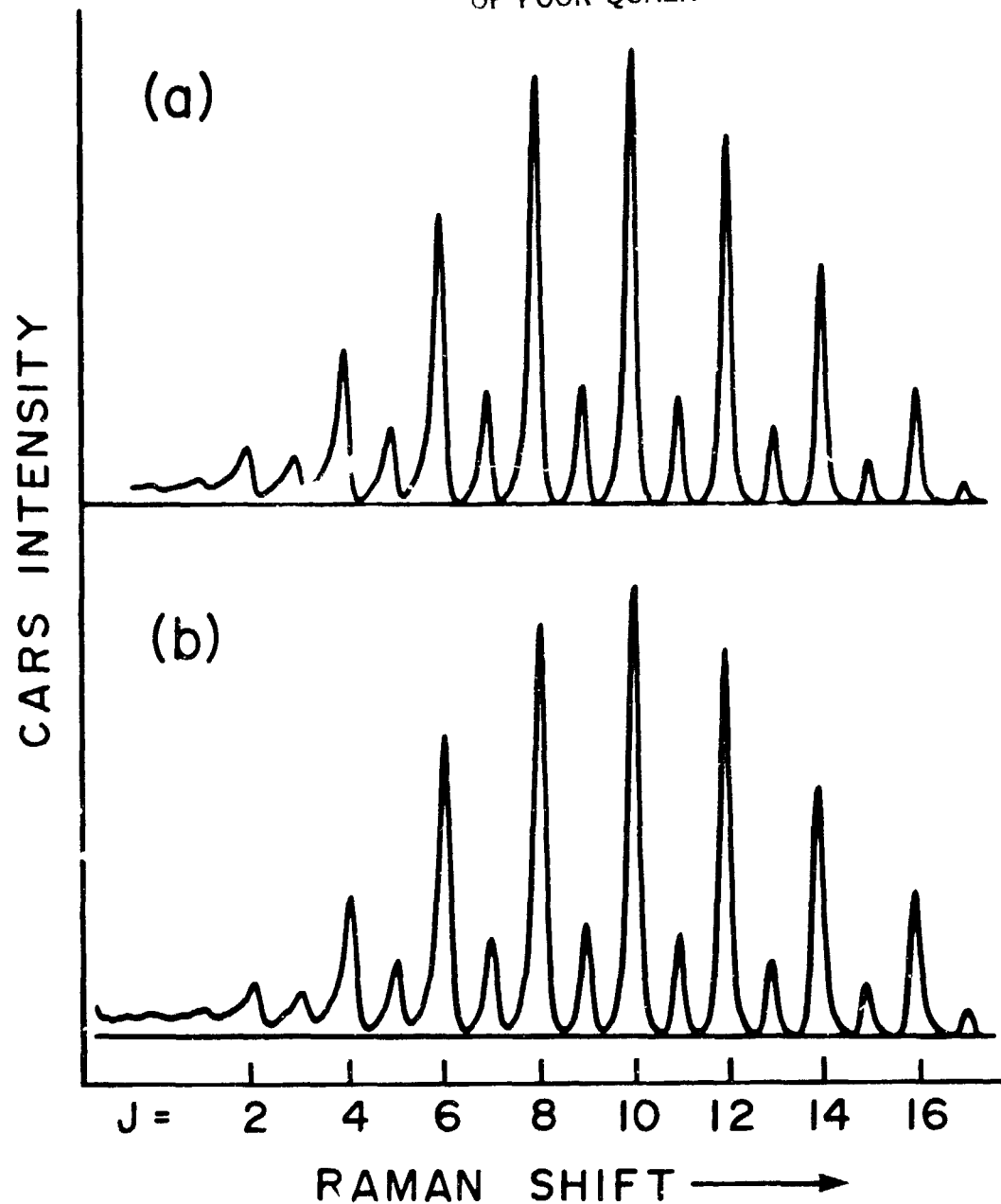


Fig. 4.3. Calculated (a) and experimental (b) CARS spectra of  $\text{N}_2$  at 296 K and 15 atm. The experimental spectrum is an average of the spectra from 100 consecutive laser firings.

#### 4.2 Calculation of Quantitatively Correct CARS Spectra

In order to calculate intensity distributions that are quantitatively correct, the values of  $K_J$ ,  $\Gamma_J$ , and  $X_{NR}$  must all be accurately known at the desired condition of temperature and pressure. The factors  $K_J$  [see Eq. (4.5)] are principally responsible for the temperature dependence of the rotational CARS spectra, since they include both the number density,  $N$ , and the population difference,  $\Delta$ . The linewidths  $\Gamma_J$  vary with temperature and pressure; they are important parameters because they determine the degree of interference between the various susceptibility terms. The nonresonant susceptibility is constant but its effect on a CARS spectrum does depend on the pressure and temperature of the gas.

The rotational Raman lines in  $N_2$  are pressure-broadened down to below 100 Torr and  $\Gamma_J$  therefore scales linearly with the inverse of the mean time between molecular collisions. This implies that the pressure and temperature dependence of  $\Gamma_J$  are

$$\begin{aligned}\Gamma_J &\propto P \\ &\propto 1/T^{1/2}.\end{aligned}\tag{4.9}$$

In addition to being functions of  $T$  and  $P$ , the Raman linewidths also depend on  $J$ . Table 4.1 lists the measured broadening parameters for the pure rotational Raman lines of  $N_2$  at 300 K (Jammu *et al.*, 1966). Since the  $N_2$  lines are pressure-broadened at one atmosphere, these parameters are simply the linewidths  $\Gamma_J$  (HWHM) at STP. The  $J$ -dependence of the  $\Gamma_J$ 's is also a function of temperature due to the change in the rotational state populations with temperature. Unfortunately, this

Table 4.1

<u>Rotational Quantum Number, J</u>	<u>Broadening Coefficient (cm<sup>-1</sup>/atm)</u>
0	.058*
1	.055*
2	.052
3	.051
4	.048
5	.048
6	.046
7	.042
8	.041
9	.040
10	.038
11	.037
12	.035
13	.034
14	.032
15	.032
16	.031

\*These values were not reported; they are obtained by extrapolation the data from Jammu et al., (1966).

dependence has not been experimentally measured or theoretically calculated for the low  $J$  levels in cold  $N_2$ . [Some experimental and theoretical work on this problem has been done recently for Q-branch lines in  $N_2$  gas at combustion temperatures (Rahn *et al.*, 1980; Hall, 1980)]. Therefore, this dependence was ignored in this work and the linewidths at non-STP conditions of temperature and pressure were calculated from the values given in Table 4.1 using only Eq. (4.9).

The remaining quantity required in evaluating Eq. (4.8) is the nonresonant susceptibility; in fact, since absolute signal amplitudes are not required, it is sufficient to know only the ratio  $\chi_{NR}/K_J$ . From Eq. (1.18) it can be seen that this is essentially a matter of knowing  $\chi_{NR}/(d\sigma/d\Omega)$ . Although  $\chi_{NR}$  was measured in  $N_2$  several years ago (Rado, 1967), no recent measurements are available and no absolute measurements of the Raman cross sections of the pure rotational lines in  $N_2$  have been reported. Therefore, the value of  $\chi_{NR}$  used in this work was chosen on the basis of the best visual fit between experimental and calculated spectra, judging largely by the asymmetry of the rotational lineshapes arising from the interference between  $\chi_{NR}$  and  $\chi_{RAM}$ . The value of  $\chi_{NR}/(d\sigma/d\Omega)$  obtained in this way is about 3.5 times larger than that obtained using the value of  $\chi_{NR}$  reported by Rado (1967) and assuming that the pure rotational Raman cross section is about 10 times larger than the vibrational Q-branch cross section. This is in fair agreement with the finding by other workers that the value of  $\chi_{NR}$  given by Rado (1967) is too small by a factor of 2.5 (A. C. Eckbreth, United Technologies Research Center, East Hartford, CT, personal communication).

Spectra calculated using the double-resonance theory for  $N_2$  at room temperature and pressures of 1 atm and 15 atm are shown in Figs. 4.2(a)

and 4.3(a), respectively. For comparison, experimental spectra recorded at corresponding conditions of temperature and pressure are shown in Figs. 4.2(b) and 4.3(b). The experimental spectra are averages of the signals from 200 consecutive laser pulses and have been corrected for the variation of dye laser efficiency with wavelength. The pump laser linewidth used in calculating the theoretical spectra was  $1.0 \text{ cm}^{-1}$  FWHM.

The sensitivity of the rotational CARS spectra to a small change in temperature is shown in Fig. 4.4. The percentage change in the integrated intensity of individual rotational lines for a 1 K change in temperature at 300 K is plotted as a function of  $J$ . For comparison, the integrated intensity distribution at 300 K is also shown. The small change in the distribution with temperature and the fact that the strongest CARS lines are not the most sensitive to temperature changes indicate the difficulty of making accurate temperature fits of the experimental spectra. In order to minimize the errors introduced by noise in the data, it is therefore desirable to include as many rotational CARS peaks as possible in the fitting routine in the hope that the noise will average out.

ORIGINAL PAGE IS  
OF POOR QUALITY

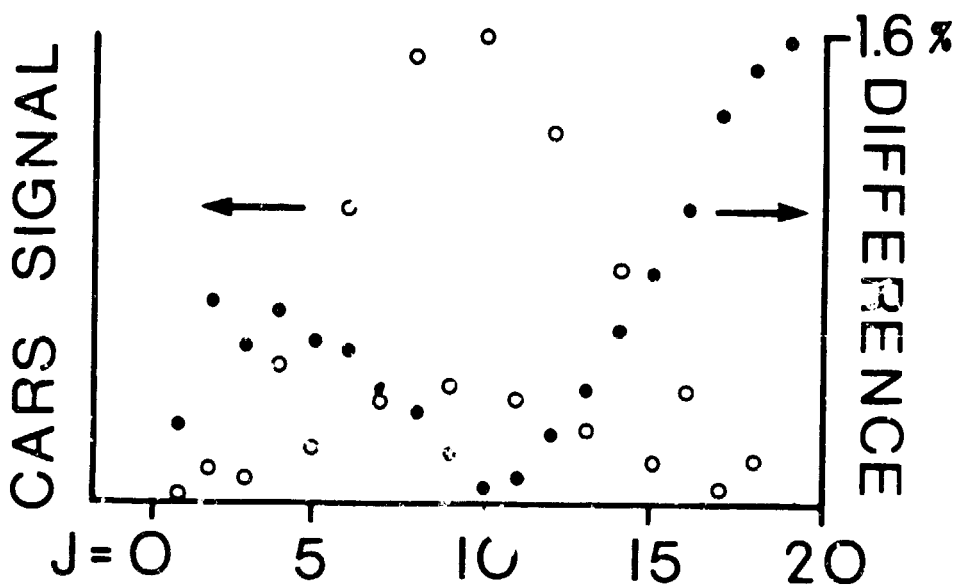


Fig. 4.4. The absolute value of the change in integrated signal of the individual rotational CARS lines for a 1 K change in temperature at 300 K (solid circles). Also shown is the integrated signal distribution at 300 K (open circles).

## 5. EXPERIMENTAL RESULTS

The results of the single-point CARS experiments are presented in this section. The results of the experimental investigation of CARS thermometry for room temperature and cold  $N_2$  are presented in Section 5.1. The experimental comparison between rotational and vibrational CARS thermometry for  $N_2$  at flame temperatures is presented in Section 5.2. The simultaneous observation of rotational CARS and CSRS for air and room temperature  $N_2$  is presented in Section 5.3.

### 5.1 Room Temperature and Cold $N_2$

This section presents the experimental results for room temperature and cold  $N_2$ . We outline the reduction of the signals recorded on the OMA to accurate representations of CARS spectra that can be compared to theory. The reduction procedures include several corrections that compensate for the nonideal characteristics of the detection system. The results of determining temperature from spectra recorded as a function of temperature or pressure are summarized. This section contains estimates of the dimensions of the mixing region, i.e., the spatial resolution of the measurements, and of the absolute magnitude of the scattered light.

#### 5.1.1 Reduction of Experimental Spectra for Comparison with Theory

A typical single-shot CARS spectrum of room temperature  $N_2$  as it was recorded by the OMA is shown in Fig. 5.1(a). The large, uneven background is due to a combination of dark noise from the camera target and electronic noise associated with the readout and analog-to-digital conversion processes. The first correction applied to the raw data is the subtraction of this background to obtain a spectrum with a flat baseline. This is accomplished by recording a "no light" frame for which the OMA

scan parameters are identical to those used in recording the experimental spectrum; this no light frame is then subtracted from the signal frame. It is impractical to record a background frame for each signal frame, but because of constant drift in the background, it is necessary to record a new background correction frame every few minutes. The background-corrected spectrum corresponding to Fig. 5.1(a) is shown in Fig. 5.1(b). Although this correction appears to the eye to work extremely well, it does introduce baseline errors that lead directly to errors in the temperatures deduced in the fitting routine. For example, a single series of CARS spectra analyzed using two consecutively recorded background frames can yield average temperatures differing by more than the rms error.

The second correction that must be applied to the data is one that compensates for the nonuniform response of the system as a function of position in the image plane. The major contributions to this response error are nonuniform throughput of the spectrometer and imaging optics and the nonuniform response of the detector itself. These errors are eliminated by dividing the background-corrected CARS spectra by a response frame consisting of a background-corrected white light spectrum obtained by placing the filament of a tungsten lamp at the sample region focus in the CARS set-up (see Fig. 3.3). White light from the lamp is directed along the same optical paths traversed by the sample and reference CARS signals, is dispersed by the spectrograph, and is imaged onto the OMA. The white light response frame therefore reflects nonuniformities in both the throughput of the entire optical system and the OMA response. Because the camera response is not strongly time or temperature dependent, a single response frame can be used with all data taken with a given optical alignment. A typical response spectrum is shown in Fig. 5.1(c).

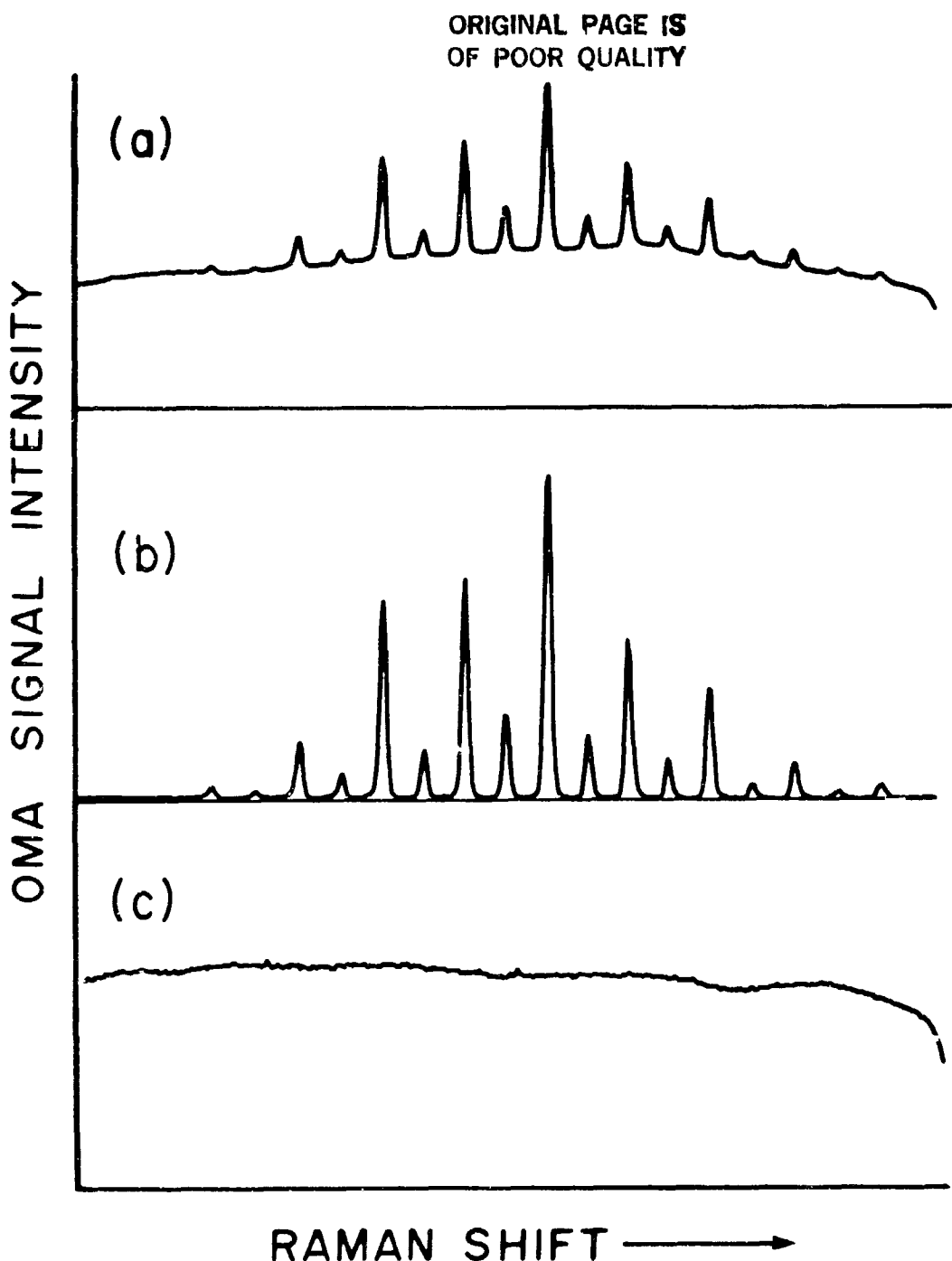


Fig. 5.1. (a) Single-shot, uncorrected CARS spectrum as recorded by the OMA. (b) Same spectrum as shown in (a), with background subtracted. (c) Typical white light spectrum used to correct the CARS spectra for nonuniform system response.

The integrated CARS power in a particular rotational line of a background- and response-corrected spectrum is obtained by summing the signals from all OMA channels in the vicinity of the line. The range of the summation should ideally be equal to the spacing between adjacent lines and should be centered on the line of interest. The full range of integration was employed for averaged spectra in which the baseline noise is small, but the range was reduced for single-shot spectra in order to avoid errors introduced by the noisy baseline between peaks where the signal is indistinguishable from the background. The final integrated-intensity distribution corresponding to a given experimental spectrum is obtained by dividing the integral of each CARS line by the total CARS signal from all lines. The resulting normalized distribution indicates what fraction of the total CARS intensity appears in each rotational line and can easily be compared to the calculated distributions.

Spectra were recorded over a range of temperatures (135 to 296 K) at atmospheric pressure and over a range of pressures (100 Torr to 15 atm) at room temperature. Both single-shot and averaged spectra were recorded as a function of temperature, while all pressure-dependent spectra reported here are averaged over 10 or 15 laser firings. A series of 5 or 10 spectra were recorded at each condition of temperature and pressure, and an average temperature and rms deviation were calculated for each series. Each experimental spectrum was compared with a series of theoretical distributions calculated at 1 K increments over the appropriate temperature range and at the appropriate pressure. The comparison was performed by calculating for each theoretical

distribution a sum of squares error parameter defined by

$$\epsilon(T) \equiv \sum_J \left( \frac{A_J^{\text{exp}} - A_J^{\text{cal}}}{A_J^{\text{exp}}} \right)^2 ,$$

where  $A_J$  is defined in Eq. (4.1). For room temperature spectra, the sum was usually over  $J = 4$  to  $J = 14$ ; at colder temperatures the range of the sum was reduced. The temperature of the experimental spectrum was then taken to be that for which  $\epsilon(T)$  was minimized.

In order to fit all of the data, theoretical distributions were calculated from 100 to 330 K at atmospheric pressure, and from 270 to 340 K at each 100 Torr increment in pressure over the range of 100 to 600 Torr and at higher pressures of 2.79, 4.57, 8.14, 11.71, and 15.29 atm. Calculation of a complete set of distributions using the single resonance theory [Eq. (4.8)] required tens of hours of processor time on a mainframe computer system--hundreds of hours would have been required had the double resonance theory [Eq. (4.6)] been used. Once the distributions were available, however, an experimental spectrum could be background- and response-corrected and fit to yield a temperature in several seconds using a microcomputer.

### 5.1.2 Temperature and Intensity Measurements in N<sub>2</sub> at STP

A large number of spectra were recorded with the sample and reference gases at room temperature in order to determine the accuracy of the overall fitting procedure, including the background and response corrections, the reference normalization and the comparison with theory. Figure 5.2 shows the room temperature sample (b) and reference (a) spectra

ORIGINAL PAGE IS  
OF POOR QUALITY

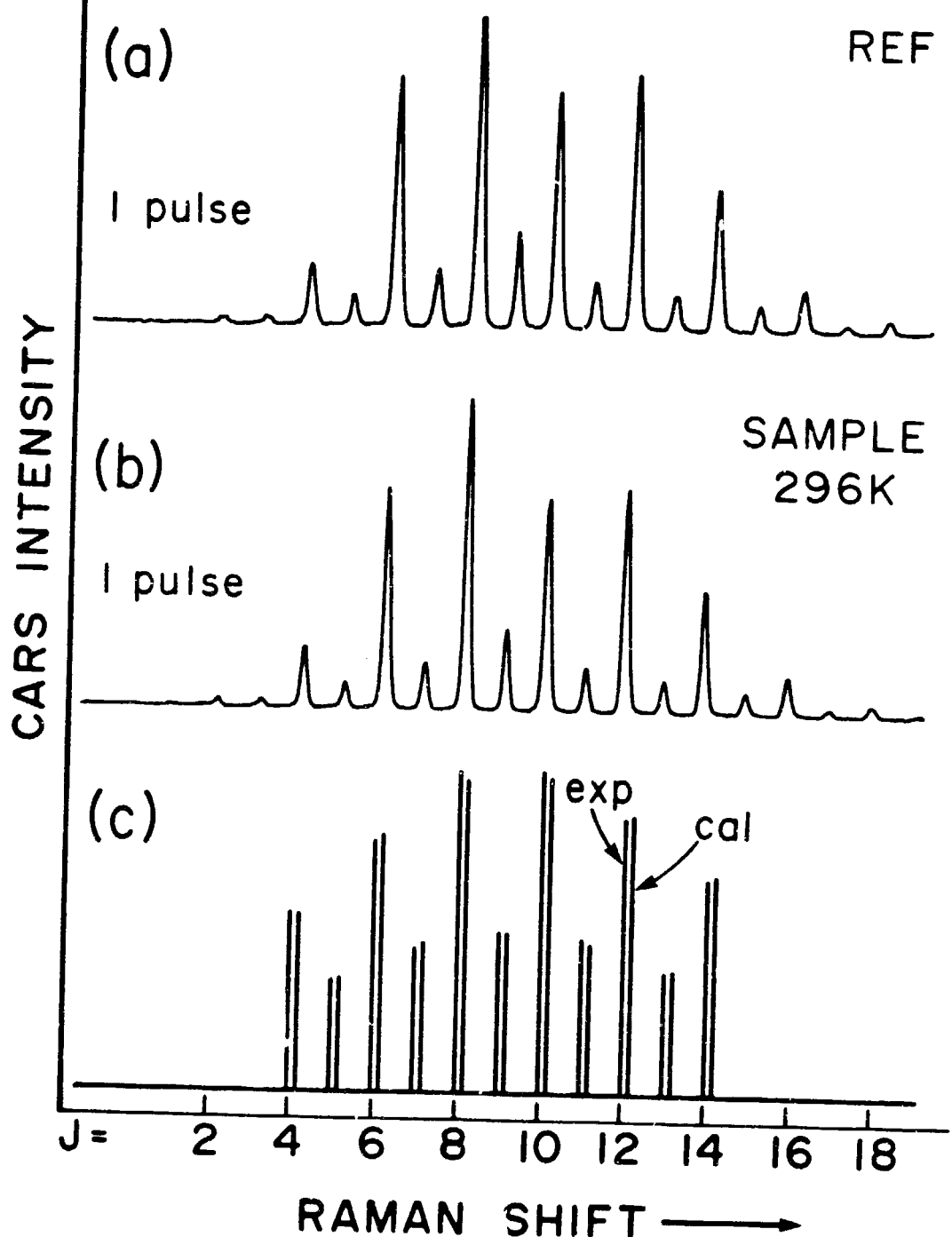


Fig. 5.2. Single-shot spectra of room temperature sample gas (b) and reference gas (a). The distribution of signal among the rotational lines used to fit the temperature is shown in (c) for the reference-normalized sample spectrum and for the best-fit calculated spectrum.  $T_{TC} = 296$  K,  $T_F = 293$  K.

obtained from a single laser firing. Neither resembles the calculated spectrum at 296 K [Fig. 4.2(a)] because of the spectral structure in the dye laser. Figure 5.2(c) shows the integrated intensity distributions corresponding to the reference-normalized sample spectrum and the best-fit calculated distribution. In this case, the thermocouple temperature was  $T_{TC} = 296$  K, the best-fit temperature was  $T_F = 293$  K, and the average temperature of the series was  $\langle T_F \rangle = 291.2 \pm 4.0$  K. Figure 5.3 is similar to Fig. 5.2, only in this case the experimental spectra are averages of the spectra from 10 consecutive laser shots; again  $T_{TC} = 296$  while  $T_F = 292$  K and  $\langle T_F \rangle = 291.1 \pm 0.7$  K.

The distribution of temperatures obtained from 100 consecutive single-shot spectra is shown in Fig. 5.4(a); the average temperature for this series was 297.0 K and the rms error was  $\pm 6.1$  K, as indicated. The scatter in temperature may be due either to actual differences in the sample and reference spectra or due to noise introduced in recovering the signals from the OMA. In order to determine the relative importance of these two sources of error, additional spectra were recorded with the pump and dye beams blocked after the sample region. The sample CARS signal was then split, and half was directed along its usual path to the sample track of the OMA, while the other half followed the usual path of the reference signal to the reference track of the OMA. The two identical spectra recorded in this way were then processed as independent sample and reference spectra, and a best-fit temperature was obtained for each "sample" spectrum. The resulting temperature distribution for 50 consecutive shots is shown in Fig. 5.4(b); the series average was  $295.6 \pm 6.0$  K. Since the sample and reference spectra were identical, the scatter can be attributed entirely to noise introduced by the OMA. The similar breadth of the distributions

in Figs. 5.4(a) and (b) suggests that this is the case even when separate sample and reference spectra are generated.

In addition to correcting spectral errors in the sample gas spectrum, the reference normalization should also reduce the shot-to-shot intensity fluctuations in the sample CARS signals. The effectiveness of this amplitude normalization can be inferred from Fig. 5.5, which shows the distribution of the integrated intensity of 100 single-shot sample spectra in (a), and the ratio of sample to reference integrated intensities for the same 100 shots in (b). For the unnormalized signals, the rms deviation from the mean intensity was  $\pm 21\%$ , while the rms deviation from mean of the normalized intensities was  $\pm 5.8\%$ . These results should be compared with those presented in Fig. 5.6, which shows the 50-shot distributions of the total sample signal intensity (a) and sample/reference intensity (b) obtained with a single spectrum divided into two parts, as above. The deviation from mean of the unnormalized signals was  $\pm 24\%$ , while the rms deviation of the normalized signals was  $\pm 2.6\%$ . Noise introduced by the OMA is responsible for the width of the distribution shown in Fig. 5.6(b), but the larger rms error observed in Fig. 5.5(b) indicates that there is significant intensity variation between the separate sample and reference signals apart from that introduced by the OMA. Thus, even with an ideal detector, attempts to determine the gas density from the normalized signal intensity will be limited to an accuracy of several percent; with the instrumentation used in this work, relative density measurements with better than  $\pm 10\%$  accuracy should be possible.

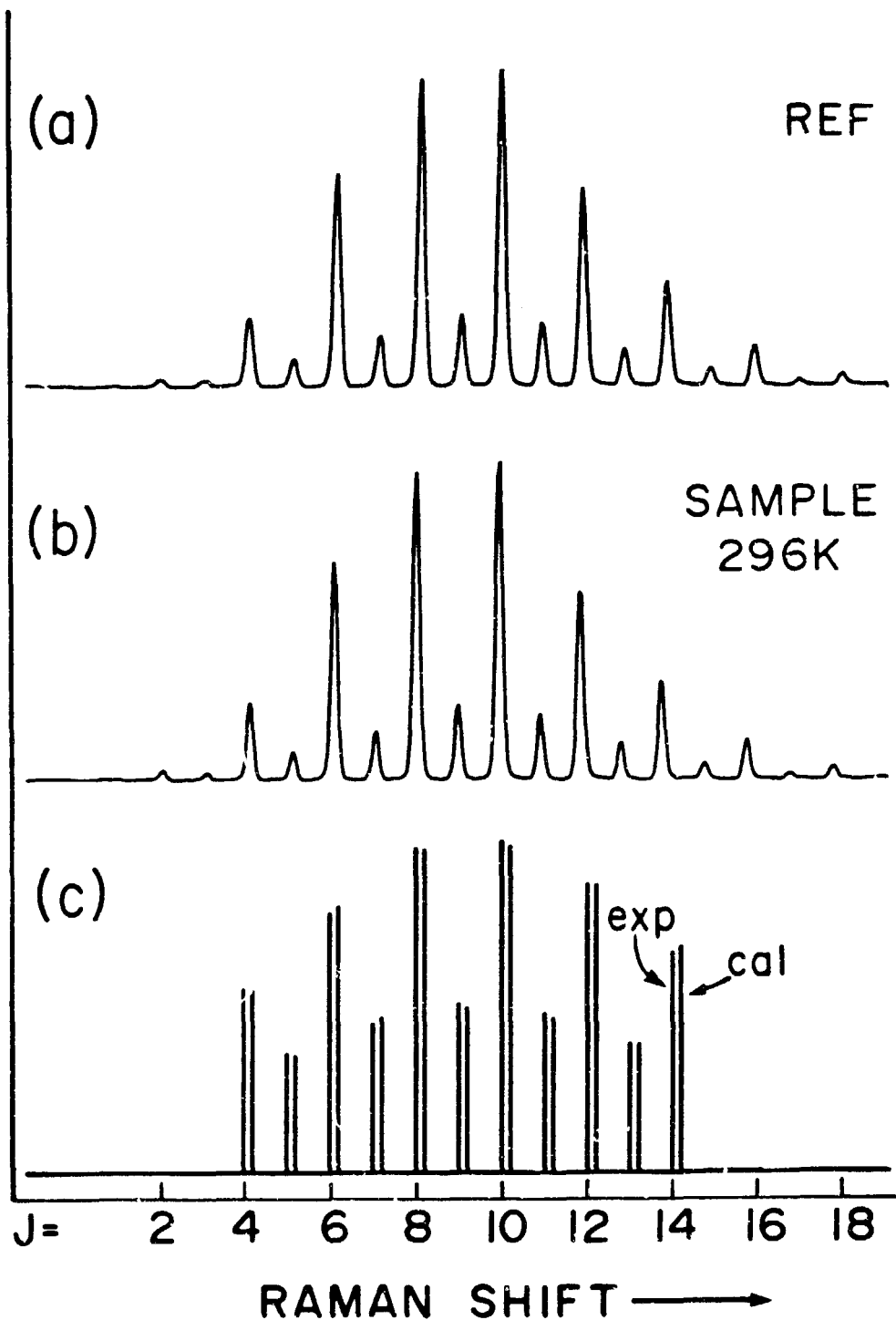


Fig. 5.3. Averaged spectra of room temperature sample gas (b) and reference gas (a). The distribution of signal among the rotational lines used to fit the temperature is shown in (c) for the reference-normalized sample spectrum and for the best fit calculated spectrum.  $T_{TC} = 296$  K,  $T_F = 292$  K; average is over 10 laser pulses.

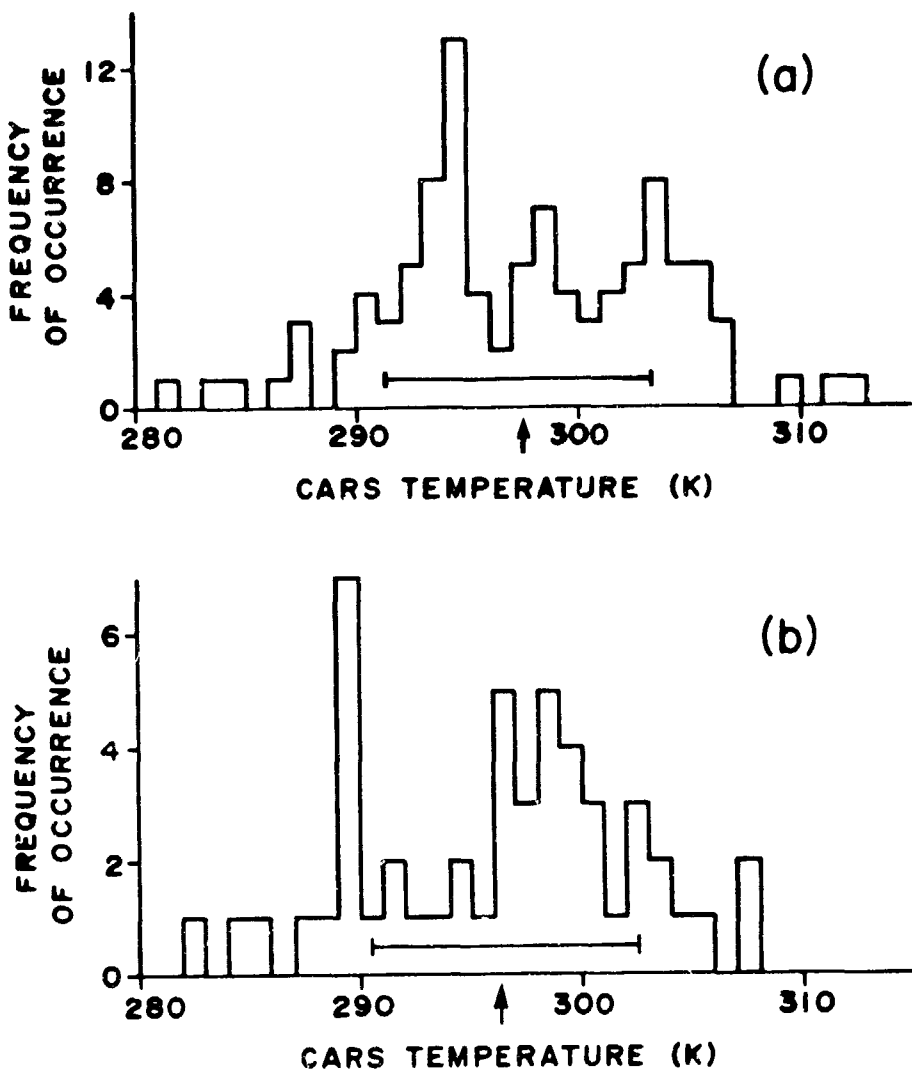


Fig. 5.4. (a) Distribution of temperatures obtained from 100 single-shot sample and reference spectra;  $T = 296$  K,  $\langle T_F \rangle = 297.0 \pm 6.1$  K. (b) Distribution of temperature obtained from 50 consecutive single-shot sample spectra split into two parts;  $T = 296$  K,  $\langle T_F \rangle = 295.6 \pm 6.0$  K. Arrows in (a) and (b) indicate  $\langle T_F \rangle$ , horizontal bars indicate rms deviations from the mean.

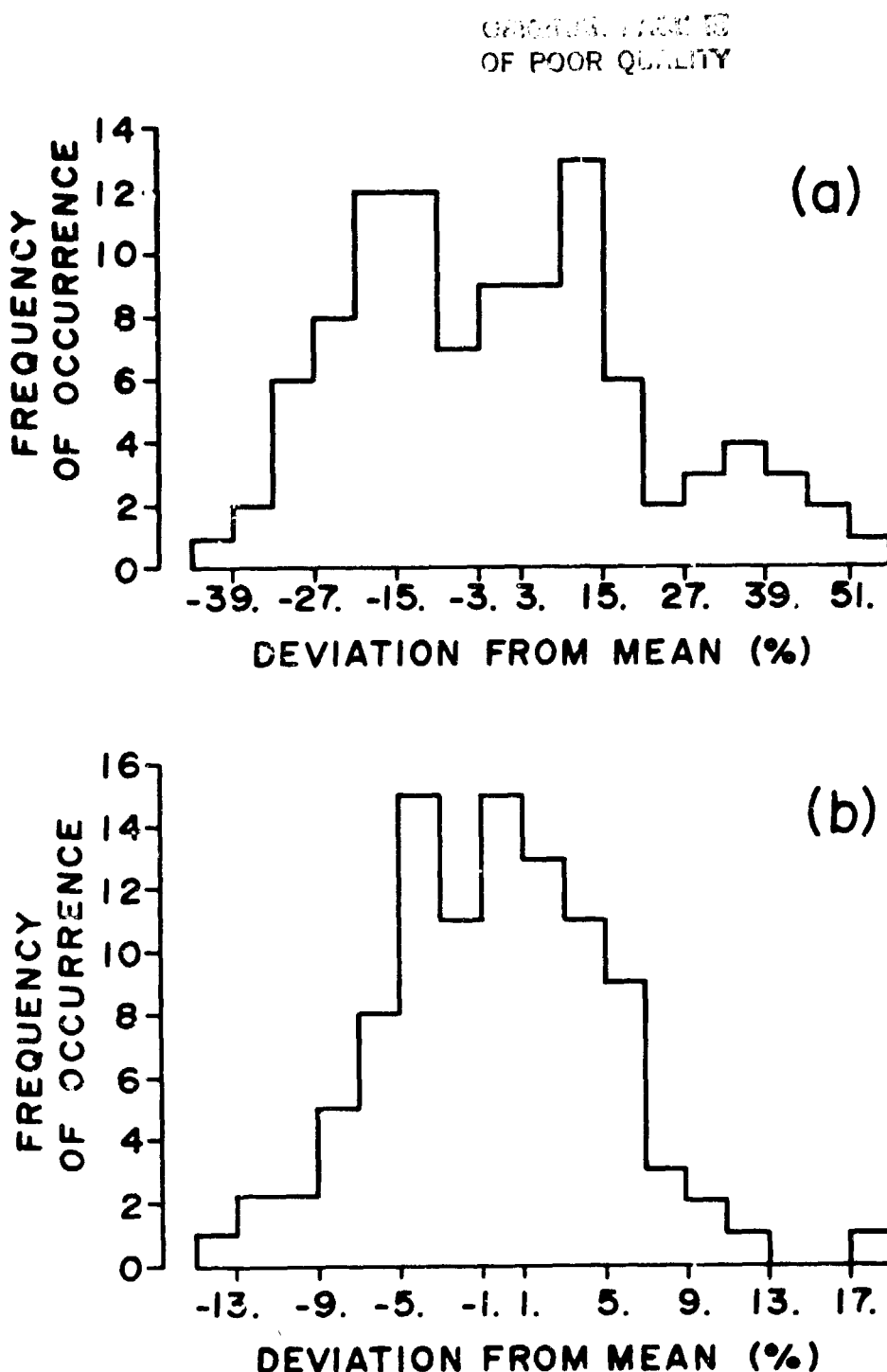


Fig. 5.5. Distributions of unnormalized (a) and reference-normalized (b) intensities of 100 consecutive single-shot CARS spectra of room temperature  $N_2$ . rms deviations from the mean are  $\pm 21\%$  for the unnormalized intensities and  $\pm 5.8\%$  for the normalized intensities.

ORIGINAL PAGE IS  
OF POOR QUALITY

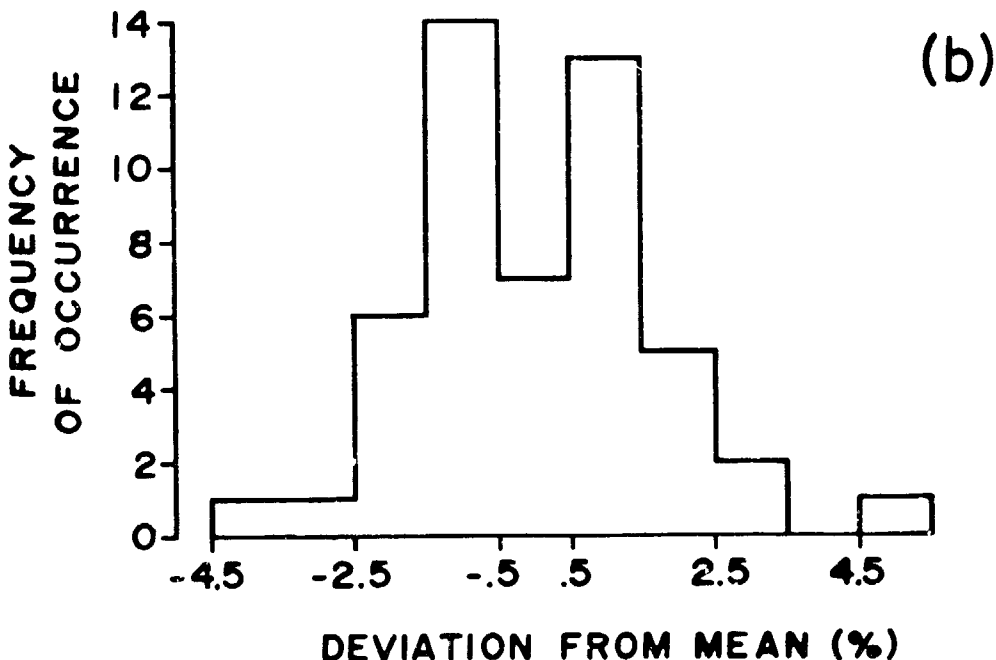
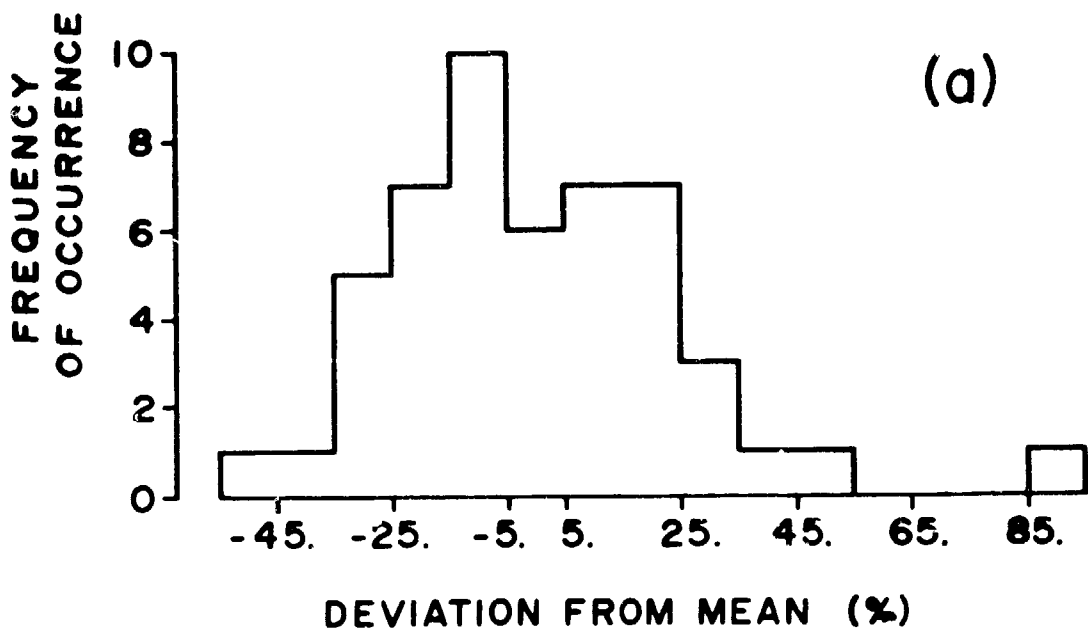


Fig. 5.6. Distributions of unnormalized (a) and reference-normalized (b) intensities of 50 consecutive single-shot CARS spectra of room temperature N<sub>2</sub>. Sample and reference spectra were obtained by splitting the sample spectrum and are identical. rms deviations from the mean are  $\pm 24\%$  for the unnormalized intensities and  $\pm 2.6\%$  for the normalized intensities.

### 5.1.3 Temperature Measurements in Cold N<sub>2</sub>

CARS spectra were recorded from N<sub>2</sub> at atmospheric pressure over the temperature range of 135 to 296 K. Two series of ten spectra each were recorded at each temperature point; one series consisted of consecutive single-shot spectra, while the spectra in the other series were averaged over ten shots. Figure 5.7 shows the cold sample gas and the room temperature reference gas spectra obtained in a single shot. The integrated-peak intensity distribution for the reference-normalized sample gas spectrum and the best-fit calculated distribution are shown in Fig. 5.7(c). Only those peaks with good signal/noise in both the room temperature and cold spectra were used in the fitting procedure. For the spectra shown in Fig. 5.7, the thermocouple temperature was T<sub>TC</sub> = 169 K, the fit temperature was T<sub>F</sub> = 173 K, and the average temperature of the series was <T<sub>F</sub>> = 170.2 ± 5.4 K. Figure 5.8 is similar to Fig. 5.7, except the sample and reference spectra were averaged over 10 shots; in this case T<sub>TC</sub> = 146 K, T<sub>F</sub> = 140 K, and <T<sub>F</sub>> = 141.8 ± 1.6 K.

The results of the measurements in cold N<sub>2</sub> gas are summarized in Fig. 5.9, which shows the CARS temperature plotted against the thermocouple temperature over the range 135 - 296 K. The error bars correspond to the rms deviation from mean of the single-shot measurements. The rms deviations from mean for the series of averaged spectra are not shown but are always smaller than the single-shot deviations.

Figure 5.9 indicates very good agreement between the CARS and thermocouple temperatures, but it should be compared with Fig. 5.10, which shows the temperatures obtained from the same data used in Fig. 5.9, also plotted as a function of thermocouple temperature.

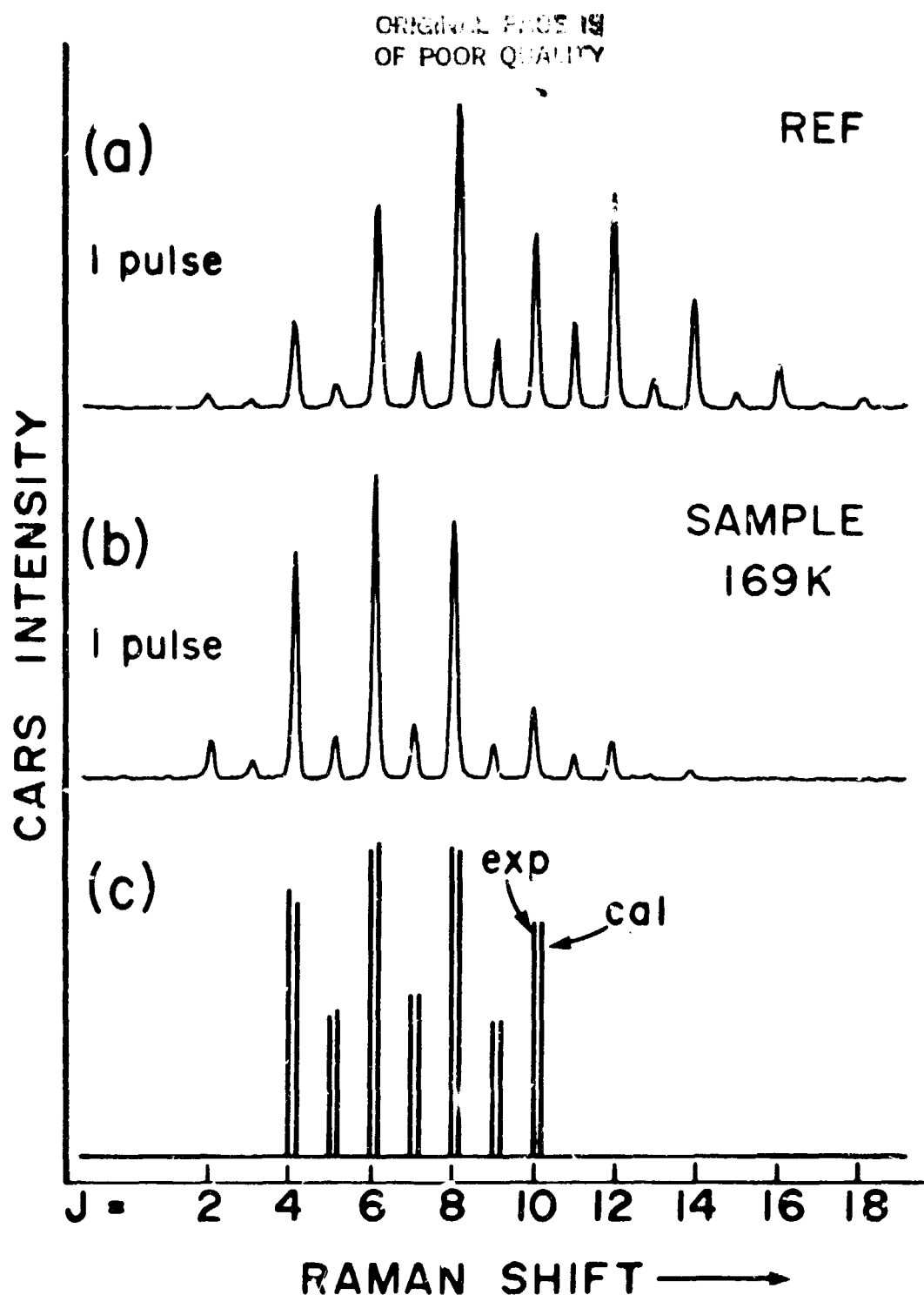


Fig. 5.7. Single-shot spectra of cold sample gas (b) and room temperature reference gas (a). The distribution of signal among the rotational lines used to fit the temperature is shown in (c) for the reference-normalized sample spectrum and for the best-fit calculated spectrum.  $T_{TC} = 169$  K,  $T_F = 173$  K.

ORIGINAL PAGE IS  
OF POOR QUALITY

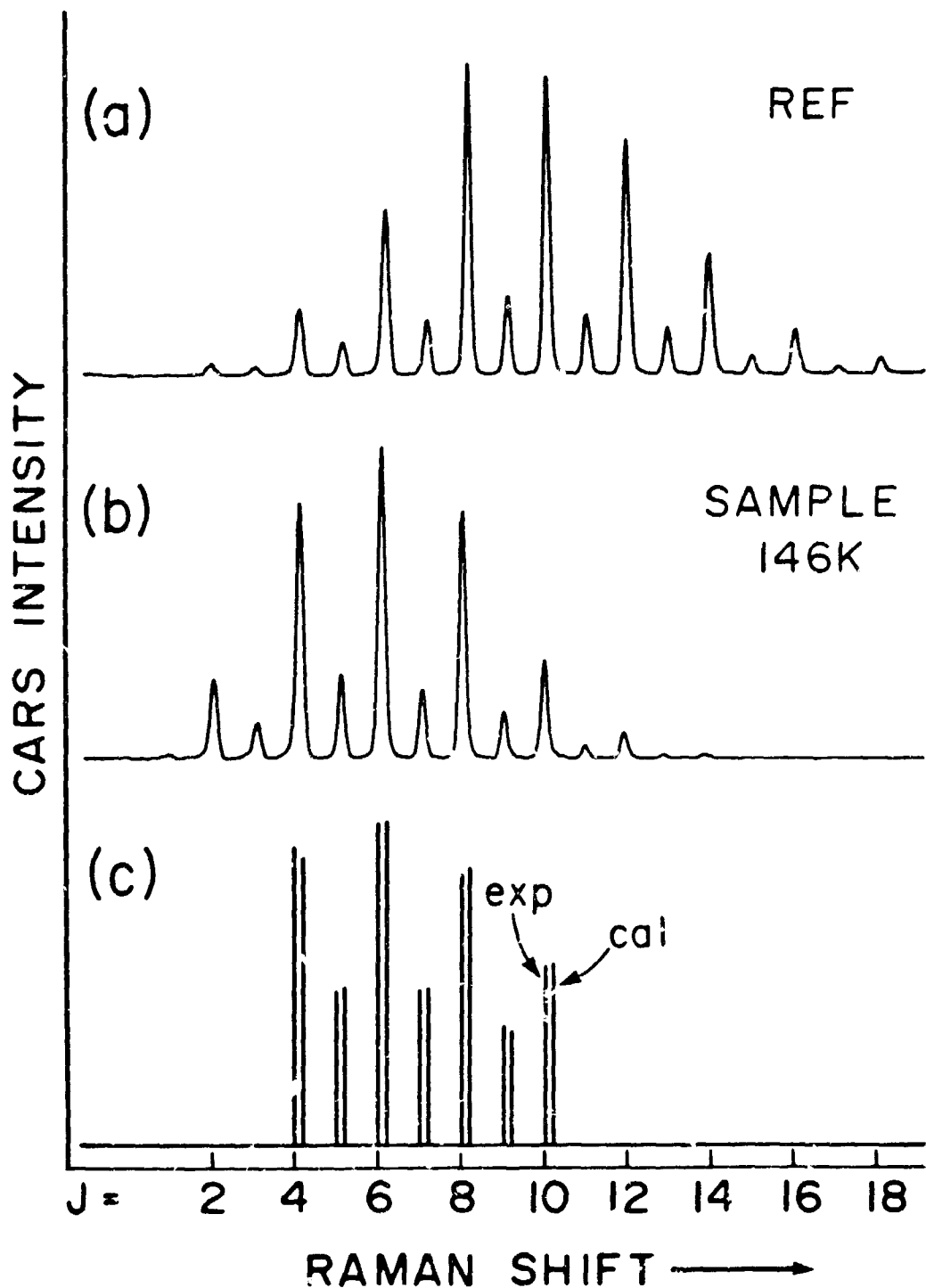


Fig. 5.8. Averaged spectra of cold sample gas (b) and room temperature reference gas (a). The distribution of signal among the rotational lines used to fit the temperature is shown in (c) for the reference-normalized sample spectrum and for the best-fit calculated spectrum.  $T_C = 146$  K,  $T_F = 140$  K; average is over 10 laser pulses.

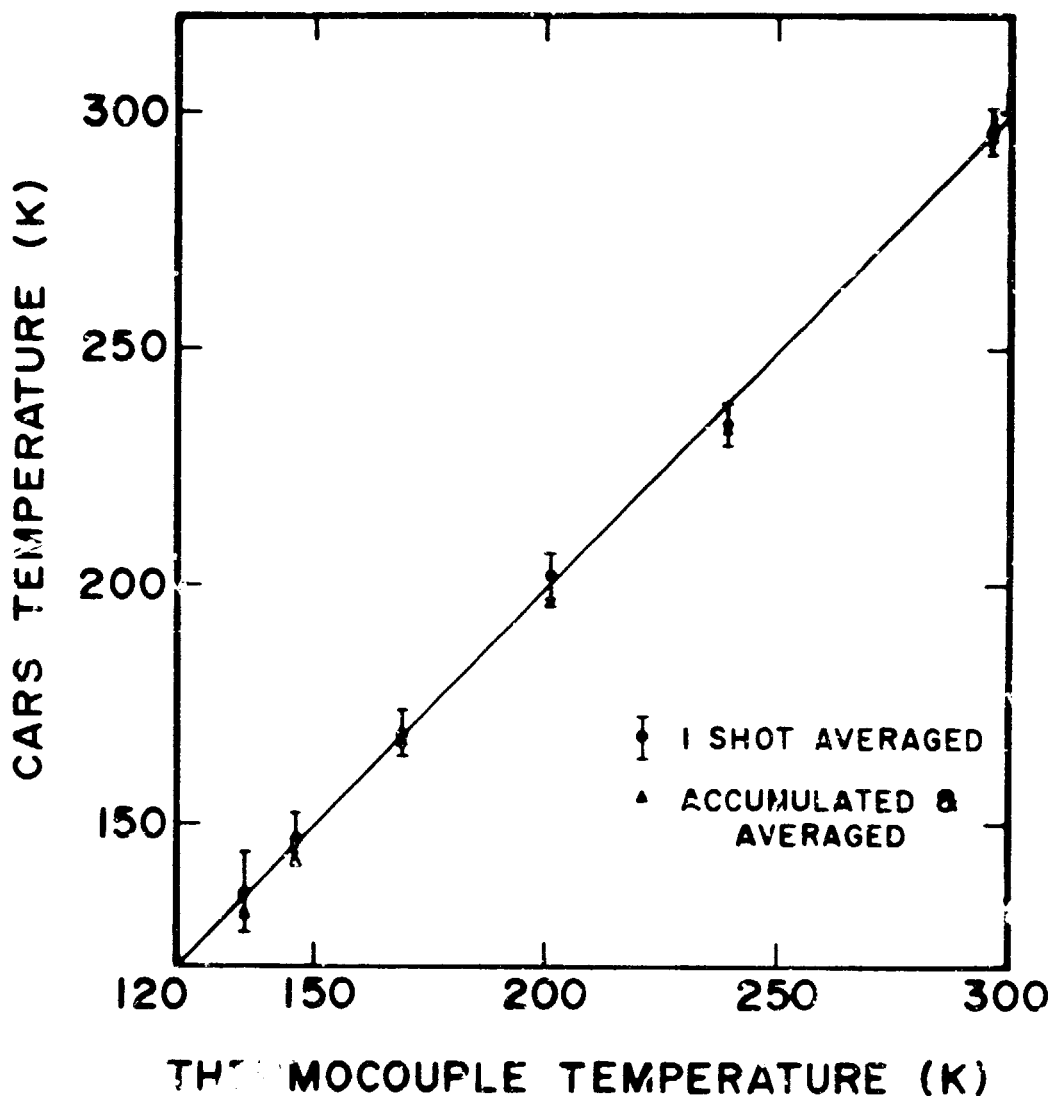


Fig. 5.9. Comparison of CARS temperature with thermocouple temperature over the range 135 to 296 K. The average and rms deviation from mean are indicated for a series of 10 single-shot spectra at each temperature. The average temperature for a series of 10 averaged spectra is also shown, where each spectrum is averaged over 10 laser pulses.

ORIGINAL PAGE IS  
OF POOR QUALITY

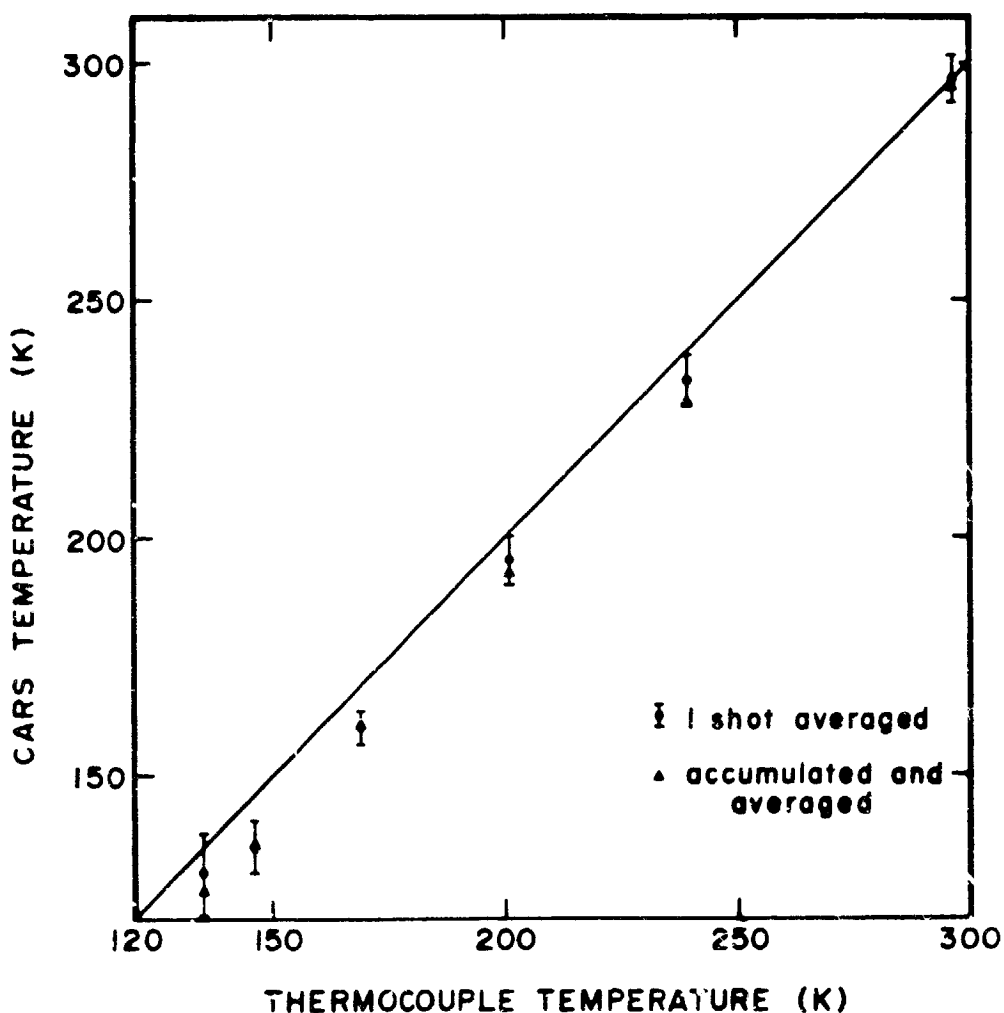


Fig. 5.10. Comparison of CARS and thermocouple temperatures for the same data as used in Fig. 6.9, but with an additional baseline correction used in the analysis.

The only difference between the two figures is in the way the background was subtracted from the raw spectra (see Fig. 5.1). The results in Fig. 5.9 were obtained by setting to zero the minimum of each spectrum once the background had been subtracted; the signal from each line was then integrated according to the procedure outlined earlier in this chapter. The correction used to obtain the results of Fig. 5.10 was similar, but in addition to setting the minimum of each background-subtracted spectrum to zero, an individual baseline was also subtracted from each peak, essentially setting to zero the local minimum in the vicinity of each rotational line. Although this step seems somewhat artificial, experience has shown that in many cases it does help to reduce the scatter in the temperature fits, and occasionally improves the accuracy at room temperature. Unfortunately, neither correction is successful in all cases, so it appears that the irreproducibility of the background of successive OMA frames is the principal limit to the accuracy of this temperature measurement technique.

The most important source of error in these measurements is the OMA. The disagreement between the thermocouple and CARS temperatures shown in Fig. 5.10 appears to be due to baseline errors caused by the inexact background subtraction on the OMA rather than to real spectroscopic effects or to inadequacies of the theory used for the calculation of the theoretical distributions. The scatter in the temperature measurements can also be attributed to noise introduced by the OMA; with a better detector there would probably still be some scatter due to real differences in the sample and reference spectra, but it is not possible to conclude from the present work what the ultimate limit would be.

#### 5.1.4 Temperature as a Function of N<sub>2</sub> Pressure

Room Temperature spectra were recorded over a wide range of pressures in order to illustrate the importance of the interferences between the individual resonant Raman lines. At low pressure, the pressure-broadened lines are very narrow ( $\sim 0.005 \text{ cm}^{-1}$  at 100 torr) and the peak resonant susceptibility is very high ( $\sim T^{-2}$ ), so the effect of the nonresonant background due to  $\chi_{NR}$  and the tails of other off-resonant lines is small. In this case the intensity distributions are very similar to those obtained assuming isolated lines with no  $\chi_{NR}$ . As the pressure, and therefore the linewidths, increase, however, the peak resonant susceptibility decreases and the influence of the real background becomes more pronounced. The effect on the integrated-intensity distributions is an increase in magnitude of the low J lines, since they have the broadest linewidths and are thus most susceptible to interference effects. The high J lines are also enhanced because they interact with the off-resonant (negative value) tails due to the lower level resonances, just as the low J lines see the sum of all of the off-resonant (positive value) tails due to the higher J resonances. The enhancement of the high J lines is less than that of the low J lines, however, because of the much narrower linewidths of the higher rotational resonances. The overall effect of these interferences is a shift toward lower J levels in the integrated CARS intensity distribution with increasing pressure at constant temperature. Thus, if spectra from two samples at the same temperature but different pressure are compared using the same calculated distributions, the higher pressure spectrum will appear to be colder than the lower pressure spectrum.

The experimental results that demonstrate this apparent change of temperature with pressure are summarized in Fig. 5.11, where the CARS temperature is plotted as a function of pressure. Each point is the average temperature of a series of 10 spectra, each of which is averaged over ten consecutive laser pulses. The spectra were recorded with the reference gas at 1 atm and 296 K, while the sample gas pressure was varied at constant temperature (296 K). The solid circles and squares represent the temperatures obtained using theoretical intensity distributions calculated for the appropriate sample gas pressure, while the open circles and squares represent the temperatures obtained by analyzing all the data with distributions calculated for 1 atm pressure. The 6 K offset at 1 atm is an experimental artifact--the low and high pressure spectra were recorded at different times, and the response correction used with the high pressure results systematically weighted the sample gas spectra toward higher temperature. The conclusion to be drawn from Fig. 5.11 is that it is necessary to know the Raman linewidths of the N<sub>2</sub> sample gas in order to accurately determine the temperature from its CARS spectrum.

The measurements of the temperature as a function of pressure are a good test of the effectiveness of the resonant reference normalization. The fundamental difficulty with the use of a resonant reference is that the normalization is not exact if the sample and reference gases have different Raman linewidths. Although the integration in Eq. (4.2) was performed by assuming that the dye laser spectrum is flat, it was recognized that the CARS process itself performs a similar integration over the exact structures that do exist in the dye laser spectrum. As long as the sample and reference gases have the same linewidths, the

ORIGINAL PAGE IS  
OF POOR QUALITY

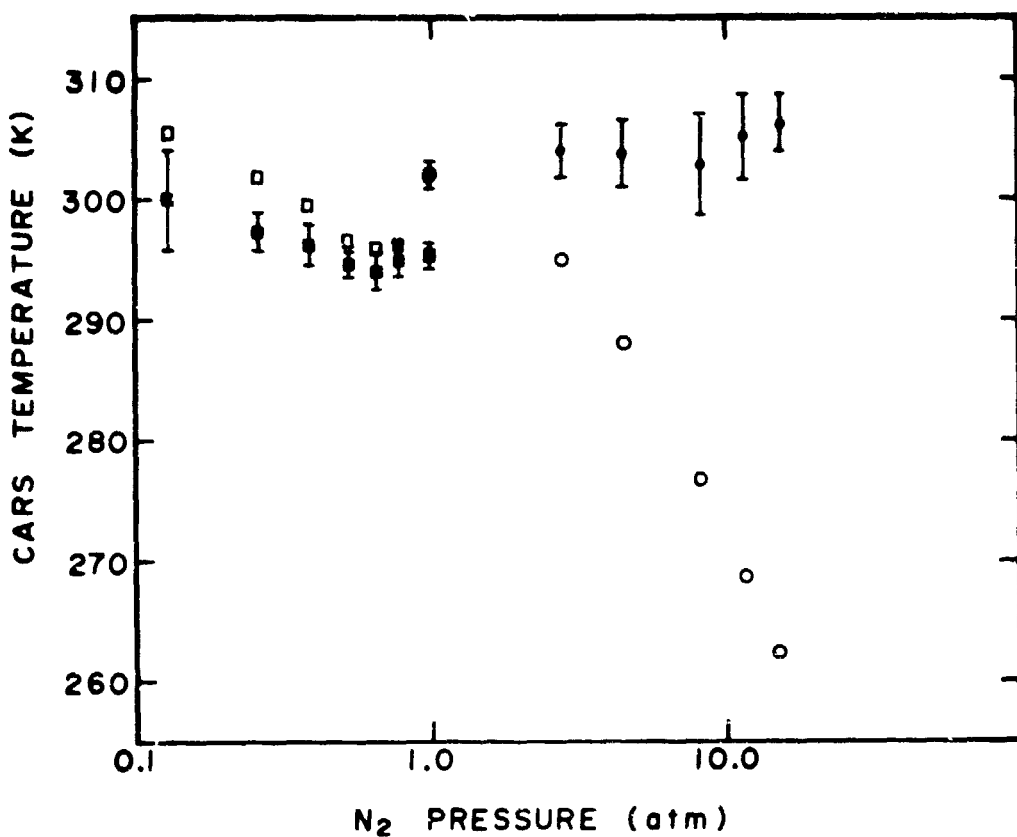


Fig. 5.11. CARS temperature as a function of sample gas pressure for room temperature sample and STP reference. Solid squares and dots indicate average temperatures obtained using theoretical distributions calculated for sample gas pressure; open squares and dots indicate average temperatures obtained using theoretical distributions calculated for 1 atm pressure. Error bars show the rms deviation from mean for a series of 10 averaged spectra at each pressure.

results of this physical integration will be the same in both media. If the linewidths are different, however, the integrand ( $|x^{(3)}|^2$ ) in Eq. (4.2) weights the same dye laser spectral component differently in the sample and reference spectra, leading to slightly different values for the two integrated signal strengths. The error introduced in this way should become more important as the difference between the pressures of the sample and reference gases increases. For example, the signal from a very broad rotational line may be significantly influenced by dye laser spectral components that are too far away to be of importance to the signal from a narrower line. However, this sort of error is not observed in this work; in fact, the results shown in Fig. 5.11 indicate that the normalization is successful even when the linewidths differ by a factor of 15. This may be attributed to the broad linewidth of the pump laser used in these experiments since even at a pressure of 15 atm, the Raman linewidths are still less than the laser linewidth. The CARS linewidths are therefore determined largely by the pump laser linewidth and, as a result, are relatively independent of pressure. The use of a pump laser with a large linewidth is therefore an advantage if measurements are to be made over a wide range of pressures.

Two new problems are encountered at pressures below 100 torr. The first is that the contribution to the Raman linewidths due to Doppler broadening becomes important, thus altering the shapes and pressure dependence of the rotational linewidths. The analysis presented in this work assumed Lorentzian lineshapes appropriate to homogeneous broadening and cannot be easily patched up to deal with the Voigt lineshapes appropriate when the Doppler and pressure broadened

linewidths are comparable. For the experimental geometry used in this work, the Doppler linewidth at room temperature is  $\sim 0.0012 \text{ cm}^{-1}$ ; the pressure-broadened linewidth of the  $J=10$  line reaches this value at  $\sim 10 \text{ Torr}$  so 100 Torr represents a safe lower limit to the range of pressures in which Doppler broadening can be neglected.

The second problem at low pressure is that the assumptions implicit in the theory used to calculate the rotational spectra break down. In evaluating the integrals in Eq. (4.2), it was assumed that the laser intensity is distributed continuously with frequency over the laser linewidths. This is not the case, however, since the laser outputs consist of many modes spaced  $\sim 0.003 \text{ cm}^{-1}$  apart in the YAG laser output and  $\sim 0.025 \text{ cm}^{-1}$  apart in the dye laser output. Equation (4.2) should be valid only in the limit that the Raman linewidths are broad compared to the laser mode spacing; this is true only for the YAG laser at atmospheric pressure ( $\Gamma_J \sim 0.05 \text{ cm}^{-1}$ ) and is true for neither laser at 100 torr ( $\Gamma_J \sim 0.006 \text{ cm}^{-1}$ ). In fact, the results shown in Fig. 5.11 do indicate that the temperature fitting routine is more successful with the sample pressure increased by a factor of 15 than it is with the pressure decreased by only a factor of 7.5.

### 5.1.5 Spatial Resolution

The spatial resolution of a CARS measurement is determined by the dimensions of the region in which the nonlinear mixing process takes place. In experiments employing colinear phase-matching, this interaction region is roughly cylindrical in shape; its length is determined principally by the speed of the focusing lens since the mixing efficiency is greatest in the region of tightest focusing. In experiments that use noncolinear phase-matching (BOXCARS,

three-dimensional phase-matching), the interaction region is also roughly cylindrical, but the length is determined by the phase-matching geometry since a signal can only be generated from the region of overlap of the three input laser beams. The transverse dimensions of the scattering region are difficult to measure directly, but they are generally determined by the focal waists of the laser beams which are on the order of 100  $\mu\text{m}$  in diameter. The longitudinal dimension [ $\sim\ell$  in Eq. (1.8)] can be measured directly and is usually much greater than the transverse dimensions, so that, in practice, the actual resolution is limited by the interaction length.

The interaction length was determined for the geometry used in this work by measuring the nonresonant CARS signal generated in a thin piece of microscope cover glass as a function of the longitudinal position of the glass in the focal region. The OMA was replaced by a photomultiplier tube in making this measurement because the nonresonant signal from the glass was quite small (the laser intensities had to be greatly reduced to avoid damage to the glass). The detected CARS intensity as a function of position  $z$  generated in a glass slide of thickness  $\Delta z$  is approximately

$$I_4^{\text{glass}}(z) \propto |\nu|^2 |(E_L^2 E_S^*)_z|^2 \Delta z^2 , \quad (5.1)$$

where  $(E_L^2 E_S^*)_z$  is the product of the input laser fields at position  $z$ . In the gaseous experiment the signal is generated from the entire

region and is given by

$$I_4^{\text{gas}} \propto | \int x (E_L^2 E_S^*)_z dz |^2 \\ (5.2)$$

$$\approx | \sum_z x (E_L^2 E_S^*)_z \Delta z |^2 .$$

where the integration and summation are over the entire interaction region. Equations (5.1) and (5.2) can be combined to yield

$$I_4^{\text{gas}} \propto [ \sum_z (I_4^{\text{glass}}(z))^{1/2} ]^2 .$$

The best estimate of the interaction length, therefore, is given not by the distribution of  $I_4^{\text{glass}}$  with longitudinal position  $z$ , but by the distribution of  $(I_4^{\text{glass}})^{1/2}$  with  $z$ . Failure to recognize this point results in an underestimate of the interaction length. The above analysis yields an interaction length of 2.5 to 3.0 mm for the geometry used in this work.

#### 5.1.6 CARS Signal Magnitude

In order to make an estimate of the magnitude of the scattered CARS power, it was necessary to make an absolute calibration of the response of the OMA to incident light. This was accomplished by using a photodiode of known responsivity at 532 nm to determine the average energy in a series of greatly attenuated pulses from the YAG laser. This number for the average energy was then used in conjunction with the integrated area of the laser line detected with the

OMA to determine a calibration factor; for the scan format used in most of this work, the calibration factor was  $\sim 22$  photons/count, where 1 count corresponds to the least significant bit of the OMA's analog-to-digital converter.

Spectra of room temperature and pressure  $N_2$  could be recorded with good signal/noise with a total laser energy at 532 nm of 20 mJ/pulse and a total broad-band dye laser energy of 1.0 mJ/pulse. Application of the calibration factor of 22 photons/count to the strongest rotational line ( $J = 10$ ) in a typical spectrum yields a total signal at the detector of  $\sim 10^6$  photons for the single line.

The signal expected from an individual CARS line can be easily calculated using Eqs. (1.18) and (1.8). The following values are appropriate to the above experimental conditions:

$$\left( \frac{d\sigma}{d\Omega} \right)_{rot} \sim 10 \left( \frac{d\sigma}{d\Omega} \right)_Q = 3.8 \times 10^{-30} \text{ cm}^2/\text{mol} - \text{sr}$$

$$\Delta = .033 \quad (J = 10)$$

$$\Gamma = .038 \text{ cm}^{-1}$$

$$N = 2.4 \times 10^{19} \text{ mol/cm}^3$$

$$L = 1.5 \text{ mm}$$

$$I_L = 10 \text{ mJ}/10 \text{ nsec}/\pi(100 \mu\text{m})^2$$

$$I_S = 1 \text{ mJ}/10 \text{ nsec}/\pi(100 \mu\text{m})^2/150 \text{ cm}^{-1} \text{ bandwidth.}$$

Because the signal from only a single line is desired, the integration over  $\omega_A$  can be performed analytically to yield

$$\int \left| \frac{1}{\omega_J - (\omega_A - \omega_L) - i\Gamma_J} \right|^2 d\omega_A = \frac{\pi}{\Gamma_J},$$

if interferences with  $\chi_{NR}$  and other rotational lines are neglected.

This calculation yields a scattered signal from the  $J = 10$  line of  $\sim 10^9$  photons. This must be multiplied by a factor of  $\sim .15$  to account for the throughput of the optics and spectrograph in order to obtain an estimate of  $\sim 2 \times 10^8$  photons at the detector. This estimate is 200 times greater than the observed signal, but discrepancies on this order are common in pulsed CARS experiments due to the nonlinear nature of the mixing process and to the non-ideal temporal and spatial properties of the laser beams.

#### 5.1.7 Discussion

The experimental results presented in Section 5.1 indicate that the broad-band, single-pulse CARS technique is capable of accurate measurement of the rotational temperature of  $N_2$  gas at room temperature and below. Because of the broad-band approach, discussion is made of the novel usage of a resonant reference cell to normalize the wavelength dependent dye laser intensity and of the problems associated with the OMA. The good agreement between the thermocouple and CARS temperatures shown in Fig. 5.9 suggests that the theory used in calculating the integrated intensity distributions is adequate for this application and indicates that the change in  $J$ -dependence of the rotational line-widths with temperature does not represent a significant source of error. It should be possible, therefore, to extend this technique to the measurement of rotational temperature in other molecules, since the theory used in analyzing the data in the current work is not unique.

to N<sub>2</sub>. It should also be a straightforward matter to extend the temperature range over which this technique is applied to both colder and warmer temperatures, although the analysis will have to be slightly modified in the latter case to include the effects of the rotational-vibrational interaction and the contribution of the rotational hot bands.

A natural extension of this work would be to the simultaneous measurement of pressure as well as temperature in the scattering medium. Just as the temperature of the sample gas is deduced by comparing the spectral features of the sample and reference spectra, the sample gas pressure can be deduced by comparing the intensities of the two spectra. Unfortunately, the sample gas pressure cannot be obtained directly from the ratio of the signal intensities, because the overall amplitude of a rotational CARS spectrum depends strongly on temperature as well as on pressure. The temperature dependence comes about through three terms in  $\chi^{(3)}$ : the molecular density, which increases with decreasing temperature (at constant pressure); the Raman linewidths, which increase with decreasing temperature; and the population difference factor, which increases with decreasing temperature due to the condensation of the rotational population into the low J levels. The overall effect is an increase in the magnitude of the CARS signal with decreasing temperature; for example, the integral of the strongest rotational line at 150 K (J=6) is 10.7 times greater than that of the strongest line at 300 K (J=10). This presents a problem for the determination of temperature and pressure from a single pulse because it is necessary to know the gas temperature in order to obtain the pressure, but we have seen that accurate temperature fits require knowledge of the pressure. One possible solution to this

dilemma is to solve for the temperature and pressure by an iterative technique in which an initial estimate is made for the temperature, assuming a pressure of 1 atm. A pressure based on this temperature can then be deduced and used to refine the temperature fit, which will allow further refinement of the pressure estimate. An analysis of this type could be applied to the spectra recorded in this work to yield time-resolved measurements of pressure and temperature with good spatial resolution and perhaps even to multipoint determination.

### 5.2 Rotational and Vibrational CARS Measurements of N<sub>2</sub> in a Flame

Coherent anti-Stokes Raman scattering (CARS) has been used extensively as a diagnostic technique for temperature measurement in combustion systems (Regnier and Taran, 1973; Stenhouse et al., 1979; Rahn et al., 1979; Hall and Eckbreth, 1981; Eckbreth and Schreiber, 1981). The relative intensities of the vibrational-rotational bands of N<sub>2</sub> gas provide a sensitive temperature probe at flame temperatures. Pure rotational CARS is superior to vibrational CARS for thermometry of N<sub>2</sub> gas at room temperature and below, since the spectra are easily resolvable in contrast to the congestion of the rotational lines in the vibrational bands of the Q-branch spectra. Furthermore, the peak third-order susceptibility for rotational CARS is larger than that for vibrational CARS (Fenner et al., 1973; Penney et al., 1974; Kondilenko et al., 1980). However, at higher temperatures, rotational CARS signal intensities are reduced substantially as the population difference factor between the initial and final states for the CARS process approaches zero. In order for this population difference to become significant, the initial states need to be of high  $\sigma$ , and thus are less populated. This small population difference at higher temperatures has led most

workers to assume that pure rotational CARS has much smaller signal strengths relative to vibrational CARS for systems at flame temperatures. We investigated this assumption by comparing, under similar conditions in the same laboratory, the rotational and vibrational CARS techniques for the determination of the  $N_2$  temperature in a flame around 1600–1900 K.

The flame was generated with a flat-flame burner and a premixed flow of  $CH_4$  and air was used. The thermocouple was fabricated from a 0.05 mm diameter Pt and Pt-13%Rh wire yielding a junction bead diameter of 0.15 mm (Farrow et al., 1982). As with the room and low temperature CARS experiments the second harmonic (532 nm) of a Nd:YAG laser was used as the monochromatic pump radiation. For the rotational CARS, the third harmonic of Nd:YAG (355 nm) was used to pump a coumarin 540A broadband dye laser (532–542 nm). The frequency selection element for this dye laser configuration was an angle-tuned dielectric mirror coated for total reflection at 532 nm, 45° incidence and s-polarization. This element provided a very smooth tuning curve and allowed lasing at the red edge of the gain curve, a characteristic the original element did not possess. For the vibrational CARS, a portion of the second harmonic of Nd:YAG (532 nm) was used to pump a broadband rhodamine 610 broadband dye laser (600–610 nm). The dye laser consisted of a transversely pumped oscillator and amplifier, with frequency selection achieved by angle-tuning the original dielectric filter placed in the oscillator cavity.

The small-angle three-dimensional phase-matching geometry was used for both the rotational and vibrational CARS. The spectrograph used for this work, as well as for the remainder of the experiments

presented in this report, was a 0.5 m spectrograph with vertical slits and a 2400 line/mm holographically ruled grating. A reference cell of Ar at 9.5 atm was used to generate a nonresonant CARS signal which essentially mimicked the spectral intensity fluctuations of the coumarin and rhodamine dye laser, and which occurred in the rotational and vibrational-rotational CARS spectrum, respectively. This reference signal was imaged on the lower portion of the spectrometer slits. The CARS of N<sub>2</sub> and the reference were detected simultaneously on spatially distinct portions of the SIT vidicon. The overall spectral resolution of the spectrograph and vidicon system was 2.7 cm<sup>-1</sup>. The flame and reference signals were corrected individually for the vidicon background and for the overall system response. The corrected flame signal was normalized by the corrected nonresonant Ar reference signal.

A typical vibrational CARS spectrum is presented in Fig. 5.12, with the experimental and the calculated spectra represented by the solid and dashed lines, respectively. For the vibrational CARS spectra, the calculated best least-squares fit temperature of 7 spectra was 1841 K and the radiation-corrected thermocouple measurement was 1865 K. The uncertainty in the vibrational CARS deduced temperature is ~3%. The vibrational temperatures were determined by Dr. Roger L. Farrow of Sandia National Laboratories, Livermore, California. These temperatures were deduced from nonlinear least squares fits of theoretical to experimental spectra. The theoretical spectra were obtained by calculating the complex Raman susceptibility, adding the appropriate nonresonant susceptibility and convoluting the resulting squared modulus with an instrumental lineshape function. These calculations are described more fully elsewhere (Farrow et al., 1982).

ORIGINAL PAGE IS  
OF POOR QUALITY

CARS INTENSITY

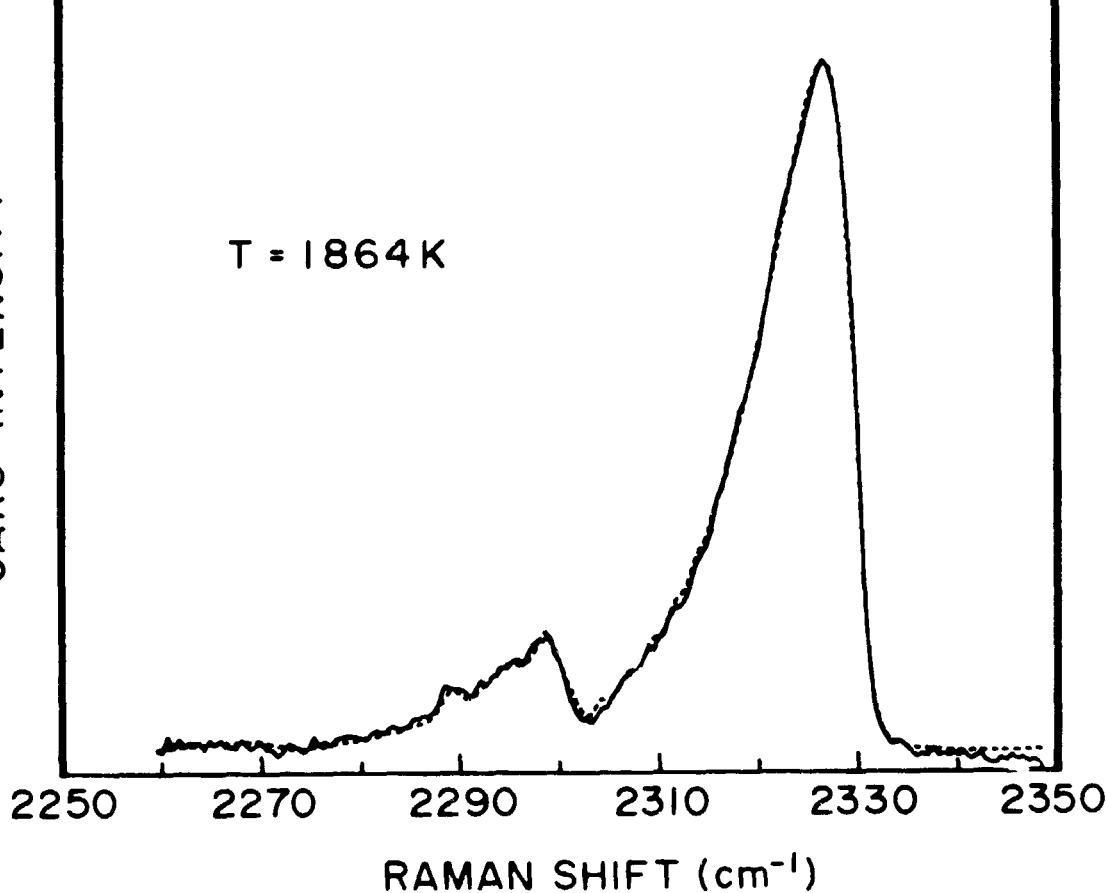


Fig. 5.12. Vibrational CARS spectra of the  $\text{N}_2$  Q-branch, where the solid line is the experimental spectrum and the dashed line is the theoretical spectrum. The thermocouple temperature was 1865 K and the best least-squares fit CARS temperature was 1864 K.

A typical pure rotational CARS spectrum of N<sub>2</sub> in a flame is presented in Fig. 5.13. The experimental spectrum is shown in Fig. 5.13(a) and a calculated spectrum, chosen for best visual fit, is shown in Fig. 5.13(b). The maximum intensity is for around J = 24. The method of determining the N<sub>2</sub> temperature from the spectral intensity distribution is different for the two CARS techniques. The approach taken to deduce the rotational temperature is to calculate the relative integrated peak area of all the J peaks over a sufficiently wide range of temperature and then to determine the least squares difference between the experimental and the theoretical integrated intensity of all the J peaks. This analysis would be similar to that described for the rotational CARS of room temperature and cold N<sub>2</sub> gas except that the influence of hot bands should be taken into account in calculating the intensity distribution of the J peaks. We are currently working on the calculation of the theoretical intensity distribution for temperatures up to 2000 K.

The higher efficiency of the second-harmonic/rhodamine dye laser system relative to the third-harmonic/coumarin dye laser system has been cited as a primary reason for choosing vibrational CARS over rotational CARS (Hall and Eckbreth, 1981). For the vibrational CARS, the total pump energy ( $\omega_L + \omega'_L$ ) was 120 mJ and the energy of the broadband rhodamine dye laser  $\langle \omega_S \rangle$  was 3.0 mJ/pulse. For the rotational CARS, the total pump energy was only 100 mJ, since portions of the fundamental and second harmonic were converted to the third harmonic in order to pump the coumarin dye laser. The broadband coumarin dye laser energy was 2.6 mJ/pulse. Since the magnitude of the CARS signal is proportional to the triple intensity product,  $I(\omega_L)I(\omega'_L)I(\omega_S)$ , for our experimental

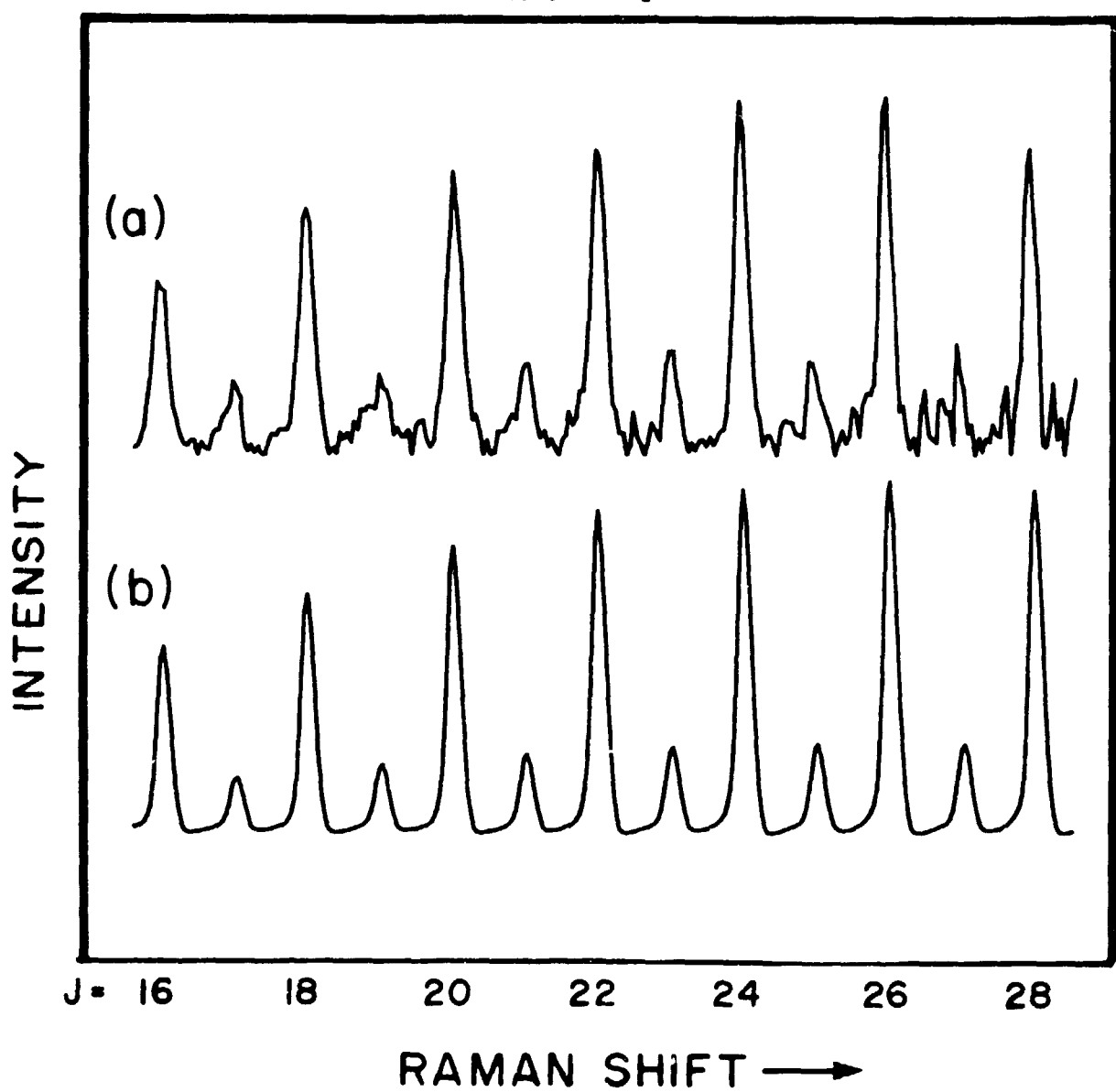


Fig. 5.13. Typical pure rotational spectrum of  $\text{N}_2$  gas in a flame.  
(a) Experimental spectrum and (b) calculated spectrum chosen for best visual fit.

situation, the vibrational CARS signal had an input intensity advantage of  $\sim 1.5X$ , all other factors being equal.

The relative signal strengths for vibrational and rotational CARS have been calculated by Hall and Eckbreth (1981). Assuming the same triple intensity product, with the spectral linewidth equal to  $0.8 \text{ cm}^{-1}$  at  $\omega_L$  and  $\omega'_L$  and equal to  $150 \text{ cm}^{-1}$  for  $\langle\omega_S\rangle$ , the ratio of vibrational CARS intensity to rotational CARS intensity was calculated. At  $T = 300 \text{ K}$ ,  $I_{\text{vib}}/I_{\text{rot}} = 1.25$  and at  $T = 1800 \text{ K}$ ,  $I_{\text{vib}}/I_{\text{rot}} = 2.5$ . Our measurement of relative signal strengths did not support this estimation. We measured signal strength for both the rotational and vibrational CARS by introducing calibrated neutral density filters into the CARS beam until their signals were indistinguishable from the vidicon readout noise. The measured rotational and vibrational CARS peak signal strengths under the same flame conditions ( $\sim 1800 \text{ K}$ ) were nearly the same, although the rotational CARS seemed somewhat stronger. Since the triple intensity product for vibrational CARS was  $\sim 1.5X$  of that for the rotational CARS, we conclude that the intensity ratio should be  $I_{\text{vib}}/I_{\text{rot}} < 1$ . That is, for the same intensity product, the peak  $I_{\text{rot}}$  is 1-2X more intense than  $I_{\text{vib}}$  even at 1800 K.

The sensitivity of the rotational and vibrational CARS spectra to temperature changes must be considered in addition to total signal intensity. Rotational CARS has the advantage of not requiring higher spectral resolution than  $\sim 3 \text{ cm}^{-1}$  since the peaks are adequately separated and only the integrated peak area for each J is required. The vibrational CARS procedure requires the fitting of the lineshape and higher resolution does improve the accuracy of the temperature deductions (Klick et al., 1981).

The main sources of inaccuracy encountered with rotational CARS measurements are associated with the broadband dye laser. The first is the decreased output of the coumarin dye laser relative to that of the rhodamine laser, and particularly the necessity to pump the coumarin dye with the third harmonic, which decreases the second-harmonic intensity which is used for the two pump beams. The second disadvantage is that any spectral structure in the dye laser output tends to influence the intensities of the isolated, relatively narrow rotational lines ( $\text{FWHM} \sim 2 \text{ cm}^{-1}$ ) much more critically than those of the broader vibrational band. Because of distortions in the optical system (spectrograph and vidicon) it is not possible to obtain an accurate correspondence between the signal and reference channels with respect to spectral frequency. This difficulty was minimized by imaging the sample and reference signal on adjacent portions of the vidicon for which the spatial distortion was minimal. Even so, for the rotational spectrum, the peaks are on the order of a few channels wide, so even a single channel mismatch creates a significant error in the integrated area for various J modes.

Nevertheless, in spite of several disadvantages associated with rotational CARS, it is still a viable technique for the measurement of flame temperatures. If the difficulties with the normalization could be solved adequately, rotational CARS would be particularly advantageous for systems requiring the measurement of a range of temperatures (77 K-1900 K) with the same experimental apparatus.

### 5.3 Simultaneous Observations of CSRS and CARS

Coherent anti-Stokes Raman spectroscopy (CARS) and coherent Stokes Raman spectroscopy (CSRS) are closely related nonlinear optical processes. The form of the third-order susceptibility ( $\chi^3$ ) for CARS and CSRS differs

when the excited electronic states are nearly resonant with the photon energy of either the pump wave or the probe wave. Depending on the  $\chi^3$  for the nonresonant process, different line shapes for the CSRS and CARS spectra can result. In fact, such line shape behavior can be used to probe the dipole matrix elements between the ground state and a particular excited state and to elucidate the characteristics of the  $\chi^3$  near electronic resonance conditions (Oudar and Shen, 1980; Carreira et al., 1978; Igarashi et al., 1980; Dutta and Spiro, 1978).

When the energies of the excited electronic states are far removed from the photon energies of any of the input beams, the CSRS and CARS processes depend on molecular parameters in precisely the same way (Druet and Taran, 1981). Consequently, the CSRS and CARS spectra contain identical information about the rotational and/or vibrational-rotational levels, their linewidths and the population difference factors between the initial and final levels. The CARS technique is generally preferred because of its excellent rejection of unwanted fluorescence and because it is more convenient to produce a Stokes, rather than an anti-Stokes, probe beam since a red-shifted dye laser can be pumped with the same radiation that provides the pump beam.

We simultaneously observed the CARS and CSRS of the rotational levels of air and of  $N_2$  by using broadband generation and detection. Previously, spectra of pure rotational CARS and/or CSRS have been obtained sequentially by scanning the frequency of the probe radiation. The probe radiation was provided by a broadband dye laser with a spectral output which spans the Stokes and anti-Stokes regions. The CSRS and CARS signals were dispersed by a spectrograph and detected simultaneously by the OMA. The small-angle three-dimensional phase-matching geometry was used ( $\alpha = 1.5^\circ$  and  $\beta \approx \gamma \approx 1.5^\circ$ ;

for the small shifts and angles involved, these angles are essentially equal). This configuration provided spatial resolution at the interaction region and spatial separation of the CSRS and CARS beams from the input beams. For large Raman shifts, the three beam angles must be adjusted so that the phase-matching condition is satisfied either for optimum Stokes production for the CSRS process or for optimum anti-Stokes production for the CARS process. However, for small Raman shifts such as those encountered in pure rotational CSRS and CARS from N<sub>2</sub> and O<sub>2</sub>, the phase-matching condition can be nearly satisfied for both CSRS and CARS processes.

Essentially the same experimental arrangement was used as in the previous CARS work. The coumarin 500 dye laser was tuned so that the broadband radiation ( $\sim 200 \text{ cm}^{-1}$ ) was centered at  $\omega_L$ , i.e., the dye laser output provided both the broadband probe Stokes radiation,  $\langle\omega_S\rangle$ , and the anti-Stokes radiation,  $\langle\omega_A\rangle$ . This particular phase-matching configuration provided adequate spatial separation of the broadband signals generated at  $\langle\omega_{\text{CSRS}}\rangle$  and  $\langle\omega_{\text{CARS}}\rangle$  from the three input beams  $\omega_L$ ,  $\omega'_L$ , and  $\langle\omega_{S+A}\rangle$ . The relative directions of these beams,  $\vec{k}_L$ ,  $\vec{k}'_L$ , and  $\vec{k}_A = \vec{k}_S$  are shown in Fig. 5.14. The spectrally dispersed CARS and CSRS signals were detected simultaneously by the OMA. A small rectangular mask was inserted at the exit focal plane of the spectrograph in order to physically block the stray radiation at  $\omega_L$ . The stray radiation at  $\langle\omega_A\rangle$  and at  $\langle\omega_S\rangle$  was much weaker than either the stray pump radiation or the CSRS and CARS signals. Thus, the three-dimensional geometry employed and the insertion of the mask provided sufficient rejection of unwanted radiation such that the CSRS and CARS signals could be observed simultaneously with the same detector, even though the stray pump radiation was not totally suppressed.

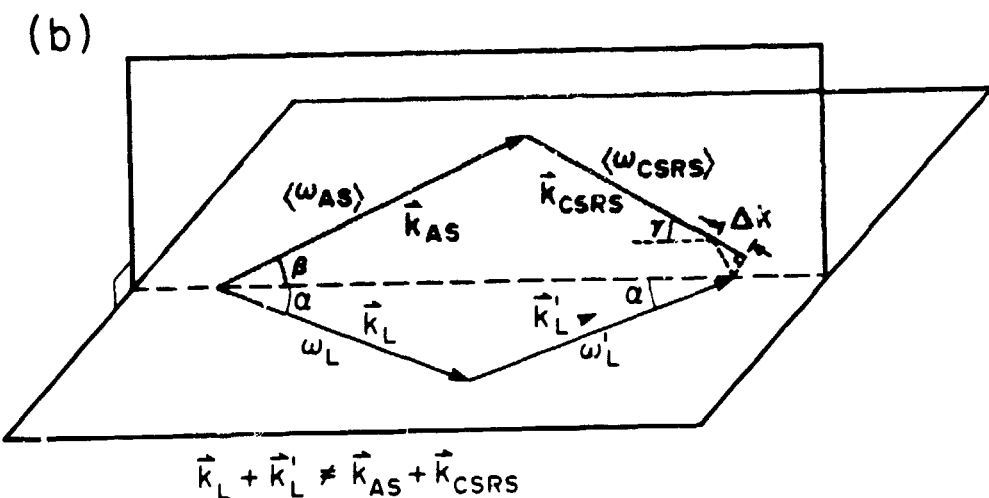
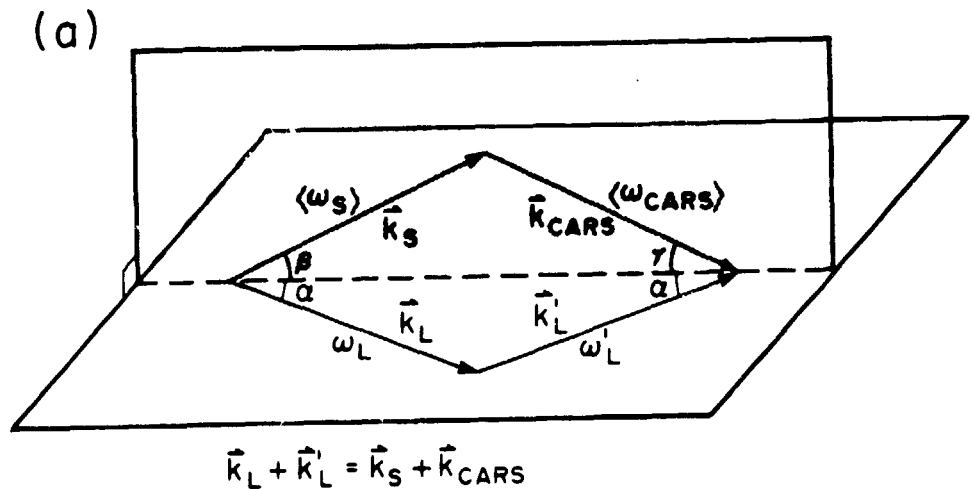
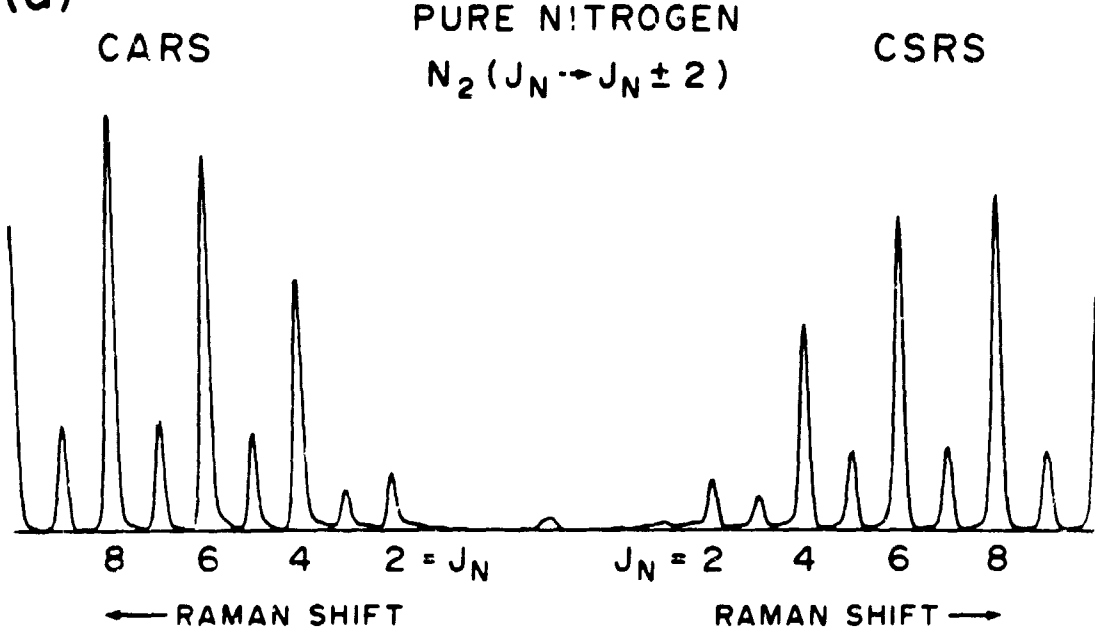


Fig. 5.14. (a) Three-dimensional phase-matching configuration for CARS process and (b) corresponding phase-matching for the CSRS process. The phase-mismatch for the CSRS process is indicated by  $\Delta k$ .

The simultaneous CSRS and CARS spectra of room temperature air and  $N_2$  are shown in Figs. 5.15(a) and (b), respectively. These spectra were corrected for the vidicon background but were not normalized with respect to the variation of the dye laser intensity with frequency. The CSRS and CARS spectra are essentially mirror images. The three input beams were aligned to optimize the CARS process [see Fig. 5.14(a)]. The slight variations in the intensity ratios of the CSRS and CARS peaks are due to the spectral structures inherent in the broadband dye laser which do not appear to average to a smooth distribution even after many pulses are accumulated on the vidicon target.

The magnitude of the phase mismatch  $\Delta k$  depends on the phase-matching angles  $\alpha$  and  $\beta$  selected for the three input beams, as well as on the frequency of the Raman shift,  $\omega_R$ . Figure 5.16 illustrates the dependence of the CSRS coherence length ( $l_{coh} = \pi/\Delta k$ ) on the phase-matching angles when the CSRS signal is detected at  $\gamma$ , the optimum angle for the CARS signal. It is convenient to compare the coherence length for the CSRS signal to the interaction length ( $l_{int}$ ) defined as the region in which the three input beams overlap. If all three beams have a diameter,  $d$ , then  $l_{int}$  can be approximated by  $d/\sin 2\alpha$ . As long as  $l_{coh} > l_{int}$ , then the CSRS signal should be nearly the same strength as the CARS signal, since the latter also is limited by  $l_{int}$ . Note that for large  $\omega_R$  (e.g., the vibrational frequencies of  $N_2$ ,  $O_2$ , or  $H_2$ )  $l_{coh}$  rapidly approaches  $l_{int}$  even for small-angle phase-matching configurations. For large  $\omega_R$ ,  $l_{coh} \rightarrow l_{int}$  when  $\alpha$  and  $\beta$  are greater than  $5^\circ$ . Consequently, a small-angle geometry is required for the simultaneous generation of CSRS and CARS for vibrational shifts. In practice, it would be difficult to generate the broadband Stokes and anti-Stokes probe radiation simultaneously.

(a)



(b)

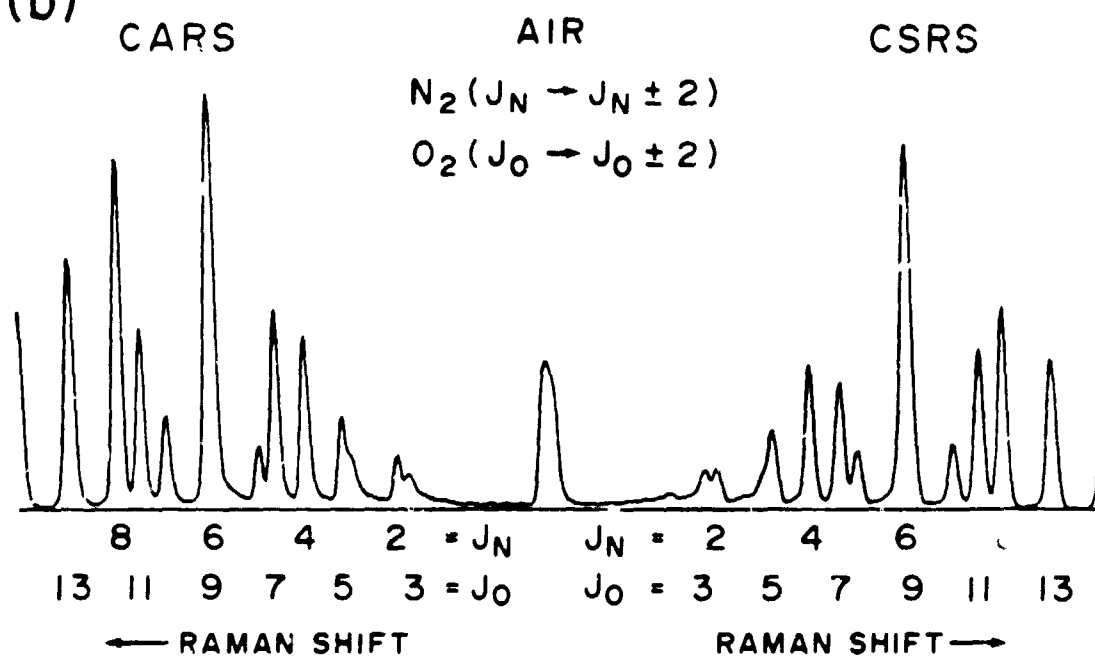


Fig. 5.15. Simultaneously observed experimental rotational CSRS and CARS spectrum (a) of  $N_2$  gas and (b) of air.

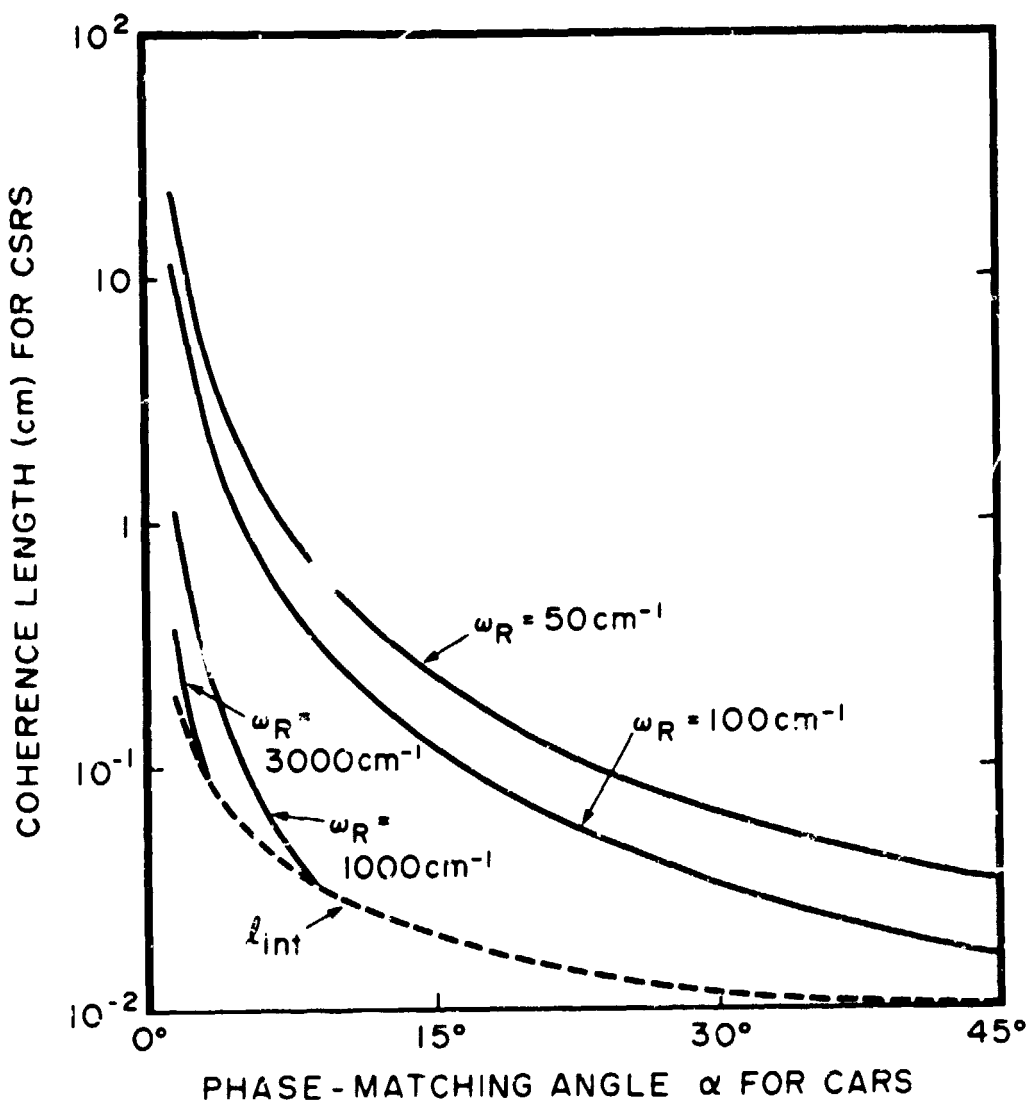


Fig. 5.16. Coherence length for the CSRS process as a function of the phase-matching angle  $\alpha$  for the CARS process for various Raman frequencies. The interaction length as a function of  $\alpha$  is indicated by the dashed line.

In addition, the simultaneous observation with a single detector is problematic because of the large spectral range spanned in the vibrational case. However, it is easy to generate and observe both CSRS and CARS for the rotational shifts in molecules like N<sub>2</sub> and O<sub>2</sub> since  $\omega_R$  is small, even for rotational shifts from J = 0 to 15. Although the above discussion assumes a dispersionless medium, similar conclusions can be reached for the simultaneous generation of CSRS and CARS for liquid and solid media possessing small  $\omega_R$ .

The small-angle phase-matching configuration used in this experiment is sufficient to exclude the detection of signals generated from stimulated Raman gain (Owyoung, 1978) since the output beams are not traveling in the same direction as the input probe beams. The inadvertent detection of stimulated Raman scattering due to the intense pump beam is also excluded since the CSRS and CARS signals disappear when the weaker  $\langle\omega_{S+A}\rangle$  probe beam is blocked.

Simultaneous measurement of nonresonant CSRS and CARS does not provide new information regarding the molecular system. However, similar experiments under resonant conditions may provide a means of investigating the possible interaction of the CSRS and CARS processes in driving the rotational levels.

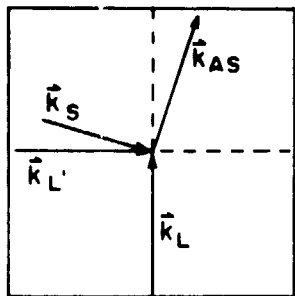
## 6. PHASE-MATCHING FOR MULTIPONT CARS

The determination of instantaneous multipoint scalar parameters (temperature and/or density) in a turbulent flow has been one of the goals of this research. In particular, we have investigated the feasibility of using CARS to obtain instantaneous temperature and concentration measurements from many spatially resolved points along a line intersecting the flow. In an essentially dispersionless medium like a dilute gas, there are various configurations which satisfy the phase-matching conditions discussed in Sections 1.1.1 and 2. There are several criteria to consider in choosing the optimal geometry: 1) the energy density of the input beams in the interaction region; 2) the spatial resolution of each volume element; 3) the spatial separation of the anti-Stokes beam from the input beams; and 4) the coherence length for the frequency shifts of the rotational lines involved. In order to obtain spectral information from points along a line, the input beams must intersect in an elongated cylindrical volume such that there are several well-defined volume elements. Our goal was to have 10-20 resolvable volume elements with dimensions approximately 0.1 mm x 0.1 mm x 0.1 mm.

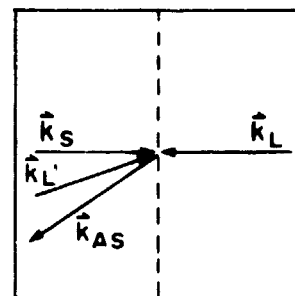
### 6.1 Comparison of Various Multipoint Geometries

The phase-matching schemes considered are shown in Fig. 6.1. Since the intersection of the beams occurs along a line, one or more of the input beams must be focused into a sheet of radiation using a cylindrical lens. The configuration shown in Fig. 6.1(c) is the same as the small-angle geometry used for the single point experiments. This has the disadvantage of requiring that all three input beams be focused into

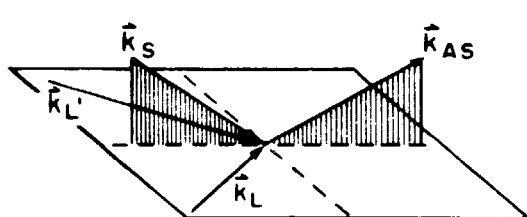
(a) planar large-angle



(b) planar counter-propagating



(c) folded small-angle



(d) folded large-angle

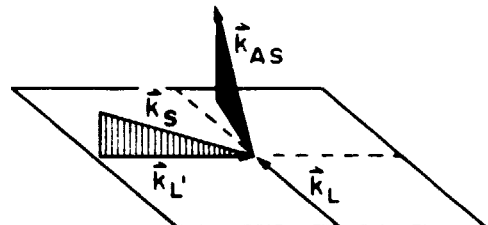


Fig. 6.1. Various phase-matching geometries for spatially-resolved multipoint CARS. The incoming pump beams are represented by  $\vec{k}_L$  and  $\vec{k}_{L'}$ . The Stokes beam is represented by  $\vec{k}_S$  and the generated anti-Stokes beam is represented by  $\vec{k}_{AS}$ .

sheets of radiation. This substantially decreases the available energy density in the interaction region. In addition, this geometry has very poor spatial resolution. The configuration shown in Fig. 6.1(a) is a planar, two-dimensional geometry. The spatial resolution for this configuration is essentially optimal, since the sheet of pump radiation,  $\vec{k}_L$ , is nearly perpendicular to both  $\vec{k}'_L$  and  $\vec{k}_S$ . This arrangement requires only two of the input beams,  $\vec{k}_L$  and  $\vec{k}'_L$ , to be focused into a sheet. The spatial discrimination of  $\vec{k}_A$  from  $\vec{k}_L$  is adequate for the relatively large frequency shifts which occur in vibrational CARS (Murphy et al., 1979). However, in rotational CARS, where the shifts are small, the direction of  $\vec{k}_A$  is almost the same as that of  $\vec{k}_L$  and adequate spatial discrimination is not possible. A counter-propagating configuration, shown in Fig. 6.1(b), has the advantage of only requiring one of the pump beams to be focused into a sheet of radiation, considerably increasing the available energy density in the interaction region. This advantage is offset by very poor spatial resolution. The large-angle nonplanar three-dimensional geometry shown in Fig. 6.1(d) is the arrangement that was chosen for this work. This geometry, where  $\vec{k}_L$  is exactly perpendicular to  $\vec{k}'_L$  and  $\vec{k}_S$ , has the optimum spatial resolution. Initially, it was thought that two beams ( $\vec{k}_L$  and  $\vec{k}_S$ ) would have to be formed into sheets. It was determined that only  $\vec{k}_L$  needed to be focused into a sheet and that  $\vec{k}_S$  and  $\vec{k}'_L$  could be focused to a line with spherical lenses. The angle  $\delta$  between  $\vec{k}_S$  and  $\vec{k}'_L$  was small enough that there was sufficient overlap of these beams in the cylindrical volume defined by their intersection with the perpendicular sheet formed by  $\vec{k}_L$ . The anticipated difficulties with this configuration were the intensity of the CARS signal due to the extremely small interaction region (about 30X less than in the

ORIGINAL PAGE IS  
OF POOR QUALITY

small-angle single-point geometry) and the problems of achieving the necessary overlap and proper alignment of the three input beams.

### 6.2 Sensitivity of Phase-matching Angles

For the large-angle three-dimensional phase-matching geometry chosen, the selection of the angle  $\alpha$  as  $90^\circ$  uniquely determines the remainder of the angles for a given frequency shift. It follows from the phase-matching condition that

$$\cos \delta = \frac{\vec{k}_L - 2\omega_R}{\vec{k}'_L} \quad \delta = 5.671$$

$$\sin \gamma = \frac{\vec{k}'_L \sin \delta}{\vec{k}_S} \quad \gamma = 5.616$$

$$\sin \varepsilon = \frac{\vec{k}_L - \vec{k}'_L \cos \delta}{\vec{k}_S \cos \gamma} \quad \varepsilon = 0.558$$

where  $\omega_R = 91.5 \text{ cm}^{-1}$  is the frequency shift of the maximum J number ( $J = 10$ ) at room temperature.

The precision of the optical alignment is extremely critical to the success of these noncollinear CARS experiments. This is particularly true in the large-angle case where the interaction region is small. It was felt that it would be useful to know which of the angular adjustments were the most sensitive with respect to the phase mismatch  $\Delta k$  and to the coherence length,  $l_{coh} = \pi/\Delta k$ . These quantities were calculated for  $\vec{k}'_L$  for angular displacements in the  $yz$  plane and in the  $xy$  plane (see Fig. 6.2). An angular displacement of  $\pm 0.5^\circ$  in the  $yz$  plane (i.e., nearly perpendicular to the direction of  $\vec{k}_S$ ) gives  $\Delta k = 16 \text{ cm}^{-1}$  and  $l_{coh} = 0.20 \text{ cm}$ .

ORIGINAL DRAWING  
OF POOR QUALITY

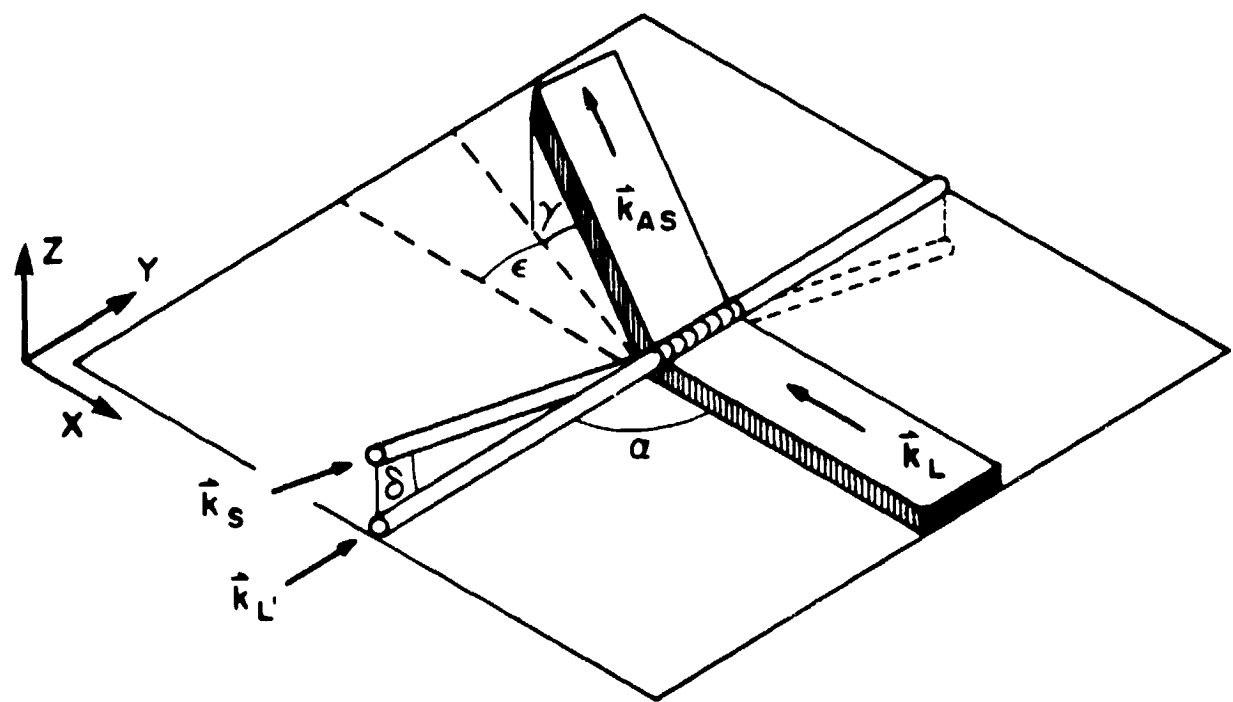


Fig. 6.2. Folded large-angle phase-matching geometry for multipoint CARS. The interaction region is depicted as several spatially-resolved cylindrical volume elements.

An angular displacement of  $\pm 0.5^\circ$  in the xy plane (i.e., nearly parallel to the direction of  $\vec{k}_S$ ) gives  $\Delta k = 160 \text{ cm}^{-1}$  and  $l_{\text{coh}} = 0.02 \text{ cm}$ . The latter adjustment is 10X more critical than the former. To optimize the overlap of the input beams, it is clear that, given a choice, it would be more advantageous to change  $\vec{k}'_L$  in a direction perpendicular to  $\vec{k}_S$  rather than parallel to  $\vec{k}_S$ .

In order to determine the required precision of the optical alignment, the phase-matching angles were calculated for the optimization of different rotational peaks. The results are presented in Table 6.1.

Table 6.1

<u>J</u>	<u><math>\omega_R (\text{cm}^{-1})</math></u>	<u><math>\delta (\text{°})</math></u>	<u><math>\gamma (\text{°})</math></u>	<u><math>\varepsilon (\text{°})</math></u>
8	75.6	5.15	5.11	0.46
9	83.6	5.42	5.67	5.92
10	91.5	5.67	5.62	0.56
11	99.5	5.92	5.85	0.61
12	107.4	6.15	6.08	0.66

The fact that more than ten rotational lines can be seen simultaneously in this large-angle configuration implies that the angle  $\delta$  can vary by  $>\pm 1^\circ$ . This result suggests that the most critical parameter in the optical alignment is the overlap of the input beams, and that slight errors in the angles are permissible.

## 7. EXPERIMENTAL DESIGN AND IMPLEMENTATION OF MULTIPOINT CARS

Many of the factors involved in executing a multipoint CARS experiment are identical to those described for the single-point CARS work. Only the factors that differ will be discussed in this section.

### 7.1 Modification of Dye Laser

The broadband dye laser used for the single-point CARS experiments, described in Section 3.1, was also used in the multipoint experiments. In order to increase the efficiency of the dye laser, the design was modified in several respects. A preamplifier stage was added with the pump energy partitioned such that the oscillator was pumped by 10%, the preamplifier was pumped by 18%, and the final amplifier was pumped by the remaining 72%. The oscillator and the preamplifier stages shared the same dye flow system, with the concentration optimized for the oscillator. The output coupler was changed from a 4% reflecting wedge to a 10% reflecting wedge and the rear mirror was coated to have maximum reflectivity at the dye laser wavelength. In addition, all of the dye laser optics were AR-coated. The dye cells were changed from 2 cm pathlength glass cells to 1 cm fused silica cells in order to optimize pumping efficiency. The increase in dye laser energy was approximately 40%, corresponding to 14 mJ/pulse with 110 mJ of third-harmonic pump energy.

### 7.2 Optical Arrangement and Alignment

The optical arrangement for the multipoint CARS is shown in Fig. 7.1. In order to achieve the correct angular alignment of the input beams, the relative spacing necessary for a given focal length lens was determined. Then the appropriate targets and masks were designed and

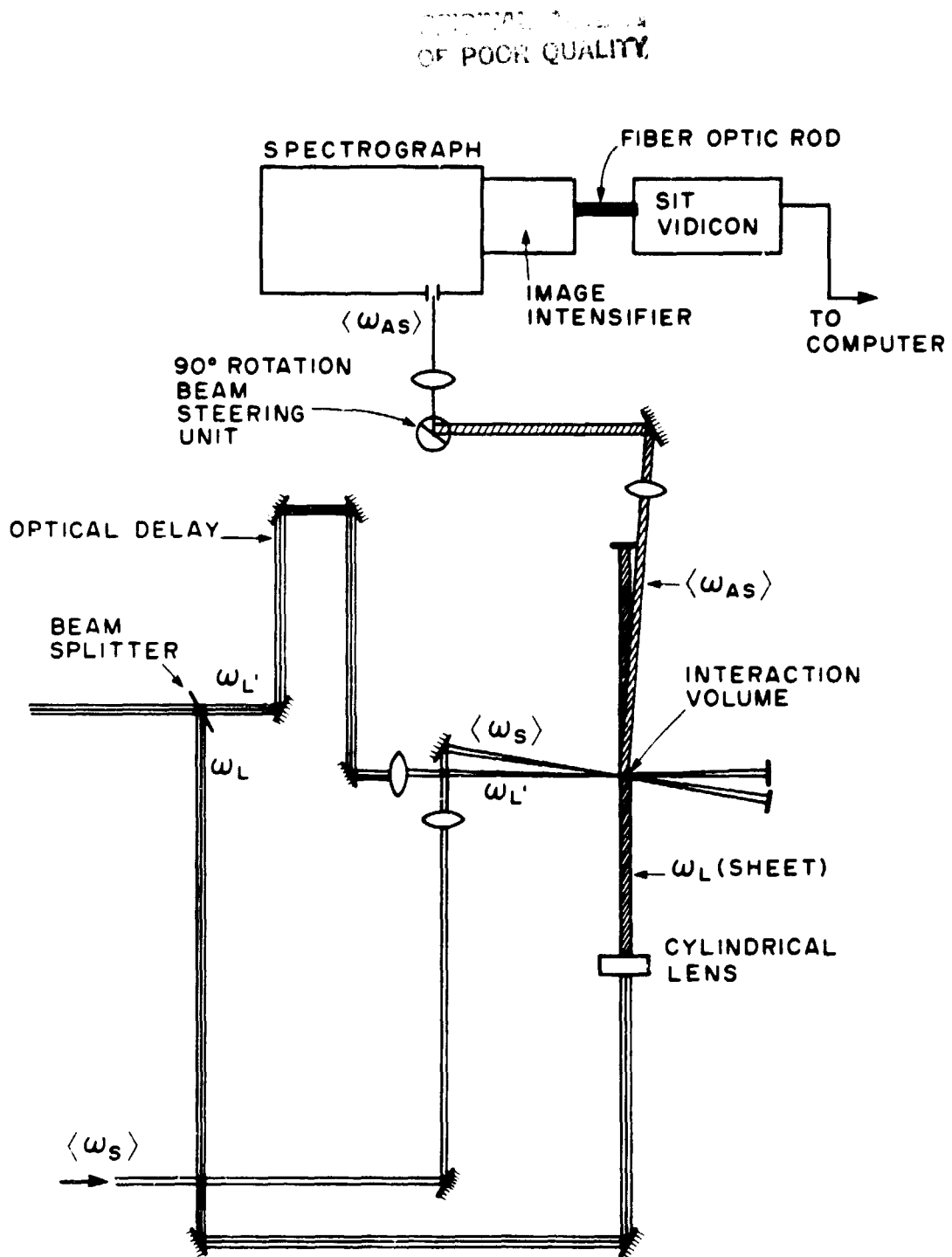


Fig. 7.1. Schematic diagram of the experimental arrangement for large-angle three-dimensional (folded) multipoint CARS.

fabricated from aluminum. The parallel input beams were aligned with the masks and targets, and then the lenses were inserted. The dye laser beam and one of the pump beams were focused with the same 30 cm spherical lens. The other pump beam was focused with a spherical lens during the initial alignment with the masks and targets. This lens was replaced with a 20 cm cylindrical lens for the final alignment. It was necessary to have an optical delay in one leg of the pump beam in order to have the three beams arrive simultaneously at the interaction region. The path of the CARS beam was mimicked by using a HeNe laser, which was then imaged onto the slit of the spectrograph. The precision of the alignment of the input beams in this manner was not adequate to obtain a detectable CARS signal. A fine adjustment to the overlap of the beams was performed by using a microscope objective (10X) to view the interaction region. After this adjustment at low powers, the laser intensity was increased and single-shot burn patterns were made on transparent tape in order to confirm complete overlap of the three input beams. After this final adjustment, it was possible to obtain a detectable CARS signal. In most cases, very little improvement (< 2X) in the signal was achieved by tweaking up the detected signal. Most often, these adjustments would degrade, rather than increase, the signal. This was in sharp contrast to the small-angle single-point geometry, where substantial improvements (> 10X) were achieved by optimizing the alignment after the signal was initially obtained. It is clear that the most critical factor is the overlap of the input beams at their focal points, and that slight deviations in the phase-matching angle are tolerable. This finding was consistent with the phase-mismatch calculations, which also suggested that the overlap was the most critical

factor. The optics required realignment each day and, occasionally, twice each day. It was often possible to regain the signal by only correcting the overlap; however, the signal level tended to be lower and eventually it was necessary to realign the entire system.

### 7.3 Multichannel Detection System

The detection system consisted of a 0.5 m spectrograph with vertical slits and a 2400 groove/mm holographically ruled grating. Initially, the input window of the SIT vidicon was positioned at the exit focal plane of the spectrograph. The position was optimized for the maximum spectral resolution. Due to the spectrograph astigmatism, this resulted in an elongated image which was defocused in the vertical dimension. For the single-point CARS work this presented no problems since the scanned area of the vidicon could be adjusted to include all of the detected signal. However, for the multipoint CARS it was necessary to have good resolution in both the horizontal (i.e., spectral resolution) and vertical (i.e., spatial resolution) dimensions. The placement of a suitable cylindrical lens (30 cm focal length for our system) between the final spectrograph mirror and the exit plane brought the image into focus for both dimensions. The spatial resolution of this system corresponded to 0.1 mm in the interaction region.

Spatially and spectrally resolved multipoint CARS spectra of N<sub>2</sub> were obtained with this experimental arrangement. However, the signal strength was quite low and required the accumulation of a great many laser shots to acquire a spectrum which had reasonable signal-to-noise. In order to obtain single-shot data it was necessary to increase the magnitude of the CARS signal. With the optimization of our Nd:YAG laser performance and the modifications on the dye laser, we had nearly the maximum input

energy that could be expected from our equipment. The optical arrangement had been optimized with respect to temporal and spatial overlap and energy density in the interaction region. We decided to investigate the possibility of amplifying the CARS signal with an image intensifier.

### 7.3.1 Image Intensifier

In order to increase the detected signal level, a 40 mm first-generation image intensifier was used in conjunction with the vidicon. The image intensifier is a vacuum tube with a self-contained high voltage power supply. It consists of an S-20 photocathode, an electron focusing arrangement and a P-20 phosphor, which emits green light. The intensifier is rated as having a white light gain of approximately 80. The image intensifier was coupled to the vidicon with a fiber optic rod (10 cm x 1.7 cm diam). This image intensifier/SIT vidicon system, shown in Fig. 7.2, will be referred to as the II-SIT detector and the unintensified SIT vidicon will be referred to as the SIT detector for the sake of brevity. The optical surfaces of the II-SIT system were index matched with glycerin, which has an index of refraction close to that of glass and which has the advantage of being water soluble and easily removed. The alignment of the image intensifier, the fiber optic rod and the vidicon is somewhat tedious, since all three pieces must have the coupled surfaces parallel to each other. This parallel alignment was accomplished by using a HeNe beam reflected from the surfaces. The parallel surfaces were brought together by using good translation stages. This method of using a fiber optic rod to couple the image intensifier with the vidicon was selected because the amount of light loss is lower than would occur if lenses were used. The fiber optic coupler was fabricated to be long enough so that the vidicon could be used in a temperature cooled mode

ORIGINAL IMAGE  
OF POOR QUALITY

## II-SIT SYSTEM

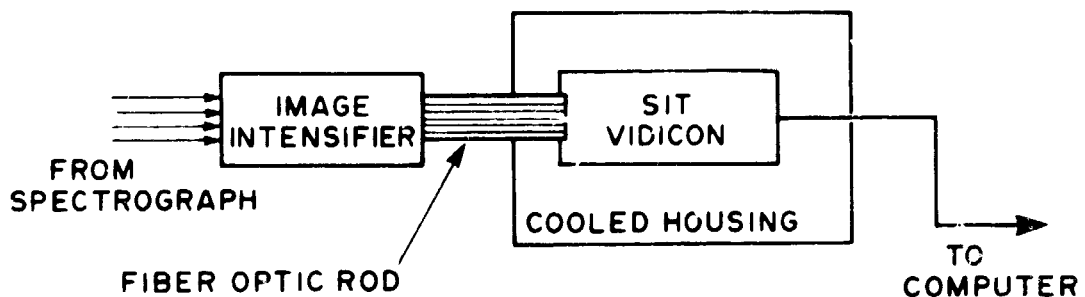


Fig. 7.2. Schematic diagram of II-SIT detector system.

while the image intensifier remained at room temperature. This is important since the lifetime of the phosphor increases dramatically at lower temperatures, causing an unacceptable lag time in the amplified signal.

### 7.3.2 Characterization of the SIT and II-SIT Detectors

Before using the II-SIT, we thought it would be useful to characterize this detection system and to compare it to the SIT with respect to gain and dynamic range. Some preliminary work in our laboratory had indicated that these characteristics were different for a pulsed signal than for a cw signal, so it was decided that the systems should be investigated using the pulsed second-harmonic radiation from the Nd:YAG laser. The 532 nm radiation was defocused with a negative spherical lens and diffused with a series of ground glass slides. This radiation was stopped down with an aperture and focused onto the slit of the spectrograph with a 10 cm lens. The intensity of this light was adjusted to a reproducible baseline level; this was the maximum light level detected. The absolute value of the light intensity was not determined. The intensity was variably attenuated with a series of calibrated neutral density filters. The illumination of the vidicon was quite uniform and a standard scanning format was used to read off the signal. The size of the scanned area was 100 × 100 pixels. The single pulse signals were reread 20 times in order to insure linearity. The value of each different intensity level is the average of 20-50 separate pulses, with more pulses being averaged for the lower light intensities.

The gain achieved with the II-SIT, relative to the SIT, is demonstrated in Fig. 7.3. This is a log-log plot of detected signal level as a function of incident laser intensity for both systems. The curves cover the complete dynamic range of each detection system. It can be

ORIGINAL PAGE IS  
OF POOR QUALITY

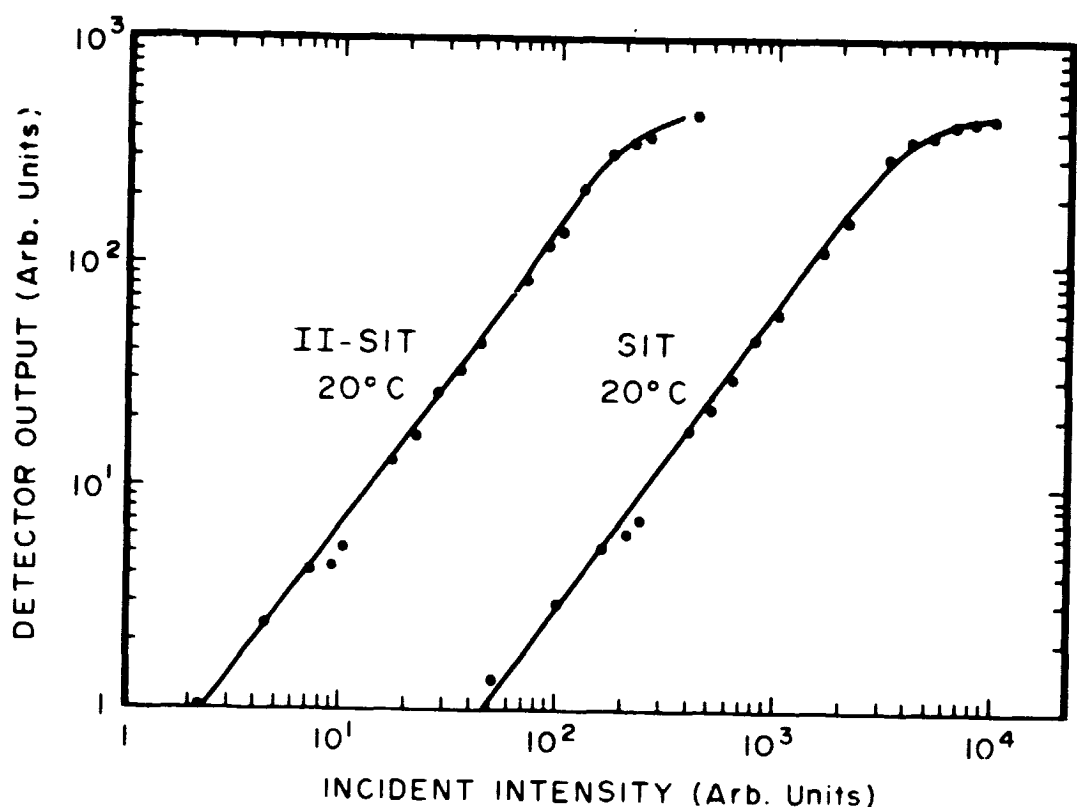


Fig. 7.3. Log-log plot of detector output as a function of incident light intensity for the SIT and II-SIT detectors at 20°C.

seen that the II-SIT is at its maximum incident light level in the linear range just as the SIT approaches its minimum detectable light level. In the linear regions of the two curves, the gain is  $\sim$ 50. The similar slope of the two curves indicates that the SIT and the II-SIT have a comparable dynamic range. The characteristic sigmoidal shape of both systems is seen clearly in the analogous linear plots in Figs. 7.4 and 7.5. At the low end of the dynamic range, an increase in the incident intensity does not result in a corresponding increase in the signal detected. At the high end of the dynamic range the detector shows saturation behavior.

We investigated the possibility of improving our detectability and increasing signal-to-noise by cooling the SIT vidicon while keeping the image intensifier at room temperature. We repeated the measurements for both the SIT and II-SIT at 20°C, 0°C, and -20°C. The curves showed no striking temperature dependence. We also performed a number of measurements of signal-to-noise at a constant incident intensity in the linear regimes of the detectors. The standard deviation of the shot-to-shot fluctuations was calculated for the SIT and II-SIT at -20°C, -10°C, 0°C, 10°C, and 20°C. The standard deviation also showed no significant temperature dependence. As a result of this findings, we proceeded with the multipoint CARS experiment using the uncooled II-SIT. By using the II-SIT, along with improvements in the dye laser and optical alignment, we were able to generate a multipoint CARS spectrum in a single laser pulse.

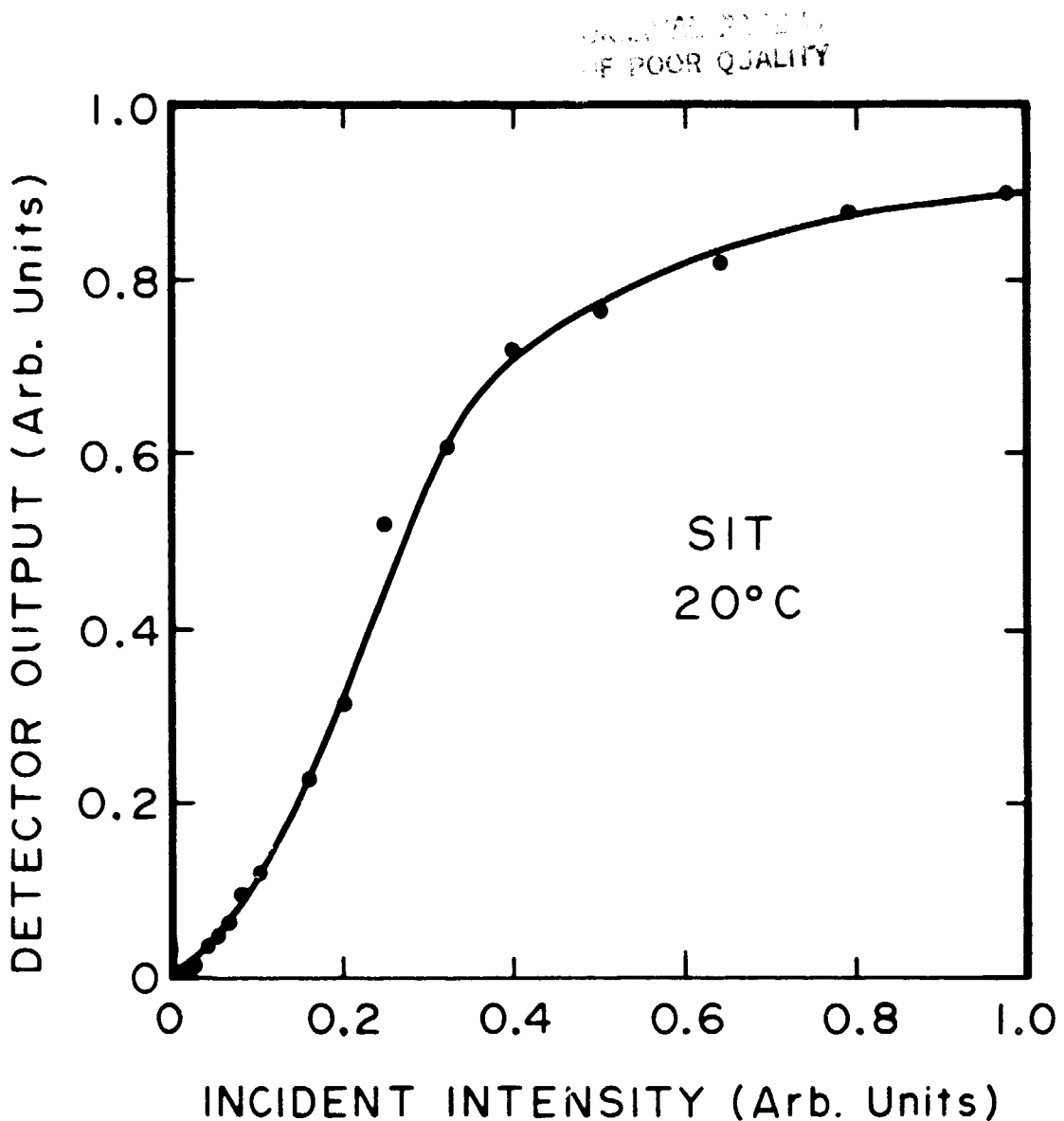


Fig. 7.4. Linear plot of detector output as a function of incident light intensity for the SIT detector at 20°C.

ORIGINAL PAGE IS  
OF POOR QUALITY

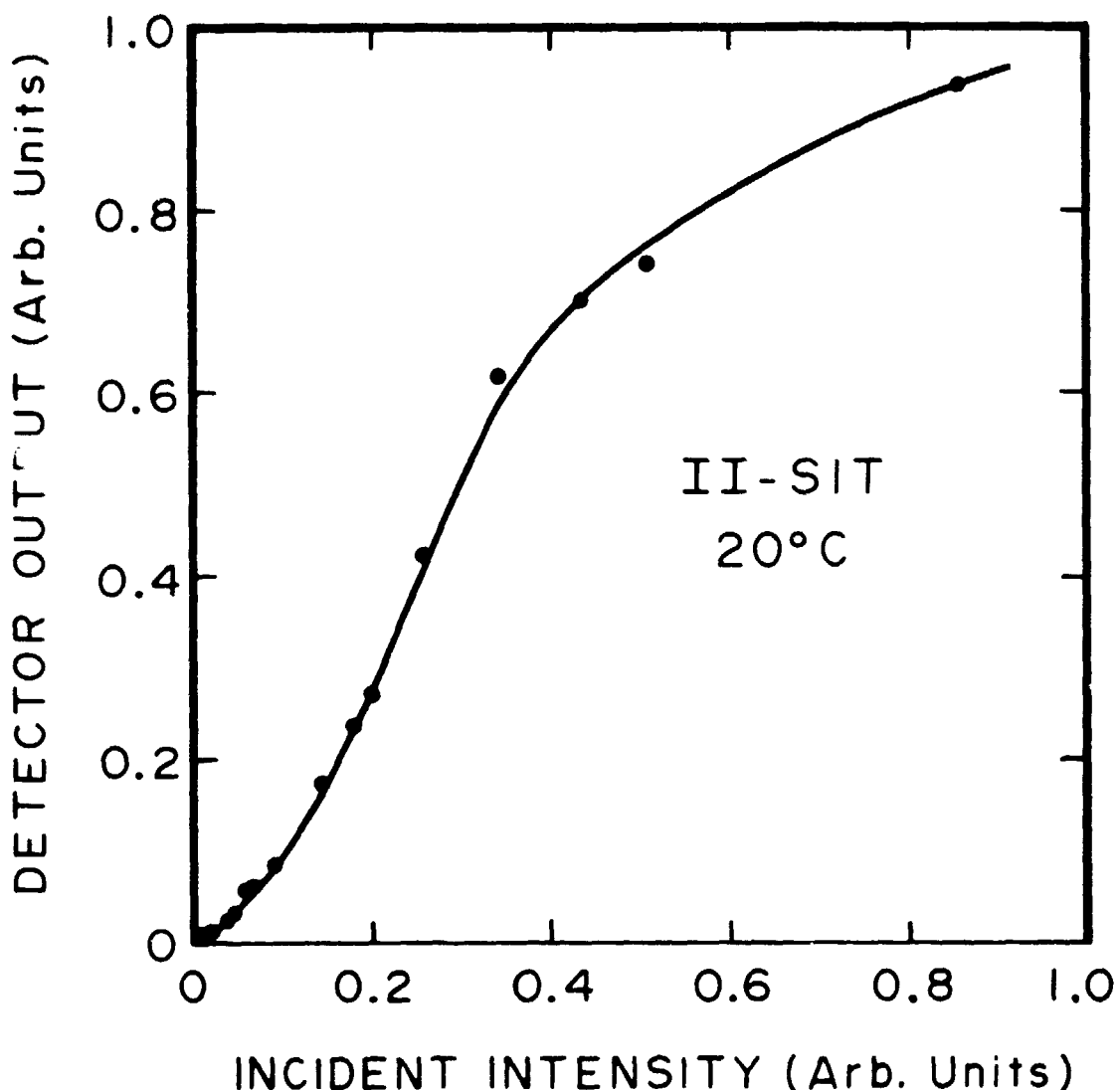


Fig. 7.5. Linear plot of detector output as a function of incident light intensity for the II-SIT detector at 20°C.

#### 7.4 Normalization Considerations

The most difficult problem which remains for the instantaneous multipoint determination of scalar parameters like temperature and concentration is normalization of the signal. This also presented difficulty in the single-point CARS measurements, but the problem is even more complex for multipoint CARS.

The multipoint CARS signal is generated with the line oriented horizontally (see Fig. 6.2). The slits of the spectrograph are vertical, requiring the rotation of the CARS signal by 90°. With this spectrograph, the scan format is rotated by 90° relative to that used in the room and low temperature single-point work. The channels, corresponding to spectral dispersion, increase (1-499) horizontally from left to right. The tracks, corresponding to the spatial dimension, increase (1-499) from bottom to top. When the signal is imaged on the vidicon, it should appear as an evenly spaced series of vertical lines, with each line representing a rotational peak in the spectrum. For the II-SIT system, low channel numbers correspond to the red (low J numbers) and high channel numbers correspond to the blue (high J numbers). The vertical dimension corresponds to different spatial volume elements, or points, along the line from which the CARS signal is generated. Ideally, the lines should be the same length and should begin and end in the same track numbers. Initially, when the CARS signal was imaged in the vidicon, the vertical lines began in different tracks, with the entire series slanting up toward the blue end. The degree of this distortion was highly dependent upon the way in which the signal was directed to the slits (e.g., slightly moving a turning mirror could change the angle of the slant dramatically). This was due to the fact that the CARS signal was already

somewhat dispersed (in the vertical dimension) when it was imaged on the spectrograph slits. Changing the rotating optic from a Dove prism to a beam-steering unit improved this significantly, as did aligning the tilt of the lenses exactly perpendicular to the beam axis. In addition, the lines were not all the same length, but tended to become shorter from one end to the other. This may have been partially due to the fan-shaped astigmatism in the spectrograph. These difficulties were adequately resolved for the purposes of demonstrating the occurrence of different species along the interaction line. However, these distortions would have to be reduced further to obtain reliable quantitative results.

In addition, the pincushion distortion in the vidicon affects the interpretation of the spectral and spatial data. This distortion causes a straight line of light imaged on the vidicon to appear curved. This curvature is most severe at the edges, so that a grid imaged on the vidicon would have the appearance of a pincushion. Unfortunately, the distortion is not symmetric, so that the correct spatial correspondence of the input and output has to be determined for each portion of the vidicon. For the single-point CARS, this was not a problem because of the normalization procedure chosen. For the CARS in a flame, limited portions of the vidicon were used so that the sample and nonresonant reference could be imaged on adjacent portions that had the least degree of distortion. These alternative approaches are not possible for the multipoint CARS since the full two-dimensional capabilities of the vidicon are required. A complete mapping of the spatial characteristics of the vidicon and a method of correcting the data would be necessary to achieve accurate information. A two-dimensional photodiode array would solve this difficulty, as well as eliminate the problem of signal lag discussed in Section 3.

We considered the use of a small-angle three-dimensional single-point reference with the large-angle multipoint CARS experiment. We anticipate two primary difficulties with this approach. First, the single-point reference scheme would not compensate for the effect of either permanent or fluctuating spatial inhomogeneities in the sheet of pump radiation. Second, because the intensity of the generated CARS signal depends on the extent to which phase-matching is achieved, the differences in coherence length and interaction volume for the two configurations could differentially affect the outlying rotational peaks for which the mismatch is the greatest. The influence of this mismatch is much more significant for the large-angle geometry than for the small-angle geometry. A multipoint reference could be used, however, space requirements present a problem. The multipoint CARS experiment with no reference requires almost all of the available space on a 4 X 8 ft. optical table. In addition, the number of precision mounts and high-power optics needed to include a multipoint reference is virtually doubled.

## 8. EXPERIMENTAL RESULTS FOR SINGLE-SHOT MULTIPOINT CARS

The multipoint CARS spectra presented in the following sections were obtained using the large-angle three-dimensional phase-matching geometry described in Section 6 and the II-SIT/OMA detection system described in Section 7.

### 8.1 Spatial Resolution

The size of the interaction region observed in multipoint CARS depends on a number of characteristics of the input beams: (1) the beam diameters in the interaction region, (2) the extent of overlap in the interaction region, (3) the overall beam energies in the interaction region, and (4) the degree to which phase-matching has been achieved. Since it is difficult to precisely control all of these parameters, the observed interaction region varies somewhat. However, a fairly reliable estimate of the interaction region can be made for the present system.

Laser burn patterns indicate that the spherically focused Stokes and pump beam diameters are  $\sim 0.1$  mm and the cylindrically focused pump beam diameter is  $\sim 0.1$  mm  $\times$  2 mm. The beam profiles also were measured at lower energies by using a 512 element photodiode array. The interaction region for the large-angle three-dimensional geometry is a cylindrical volume approximately 0.1 mm in diameter and 2mm in length (see Fig. 6.2). This estimate is confirmed by the results obtained from the image size of the multipoint CARS signal on the vidicon. The CARS signal was demagnified by 5X using the focusing optics and 0.8X by the image intensifier for a combined demagnification on the face of the vidicon of approximately 4X. Consequently, an image that has a height of one 0.025 mm pixel should correspond to 0.1 mm in the interaction

region. It was found that the multipoint CARS image was 20 pixels high corresponding to an interaction  $\sim$ 2 mm in length. This result is consistent with the length of the interaction region determined by direct measurement of the input beam dimensions.

The scan format used for the multipoint spectra divided the image on the vidicon into 20 separate tracks of data, so that 20 individual spectra are contained in each multipoint spectrum. Each track corresponds to one pixel or 0.1 mm, so that all 20 tracks represent 2 mm. A multipoint CARS spectrum of  $N_2$  is shown in Fig. 8.1. As can be seen in the spectrum, the CARS signal extends over all of the tracks. The first and last tracks of data frequently have an unacceptable level of noise resulting from the way in which the signal is read off the vidicon. For this reason, most of the multipoint spectra shown have only 17-18 tracks of data plotted, although all 20 tracks were recorded. Consequently, at least two additional tracks should be scanned and subsequently discarded in the analysis of the data. Because of the beam profile of the sheet of pump radiation and because of the diminished overlap at the edges, the intensity of the CARS signal tends to decrease at the outlying tracks. This is not a problem per se for temperature determination since the relative distribution of the rotational lines is unchanged by the total decrease in intensity. For concentration measurements, the overall decrease in intensity has to be taken into account.

## 8.2 Single Species Multipoint CARS

The spectrum shown in Fig. 8.1 was obtained by passing a flow of room temperature  $N_2$  gas vertically through the interaction region and recording the results of a single laser shot. The asymmetric spike in the spectrum is caused by electrical interference from the pulsed laser.

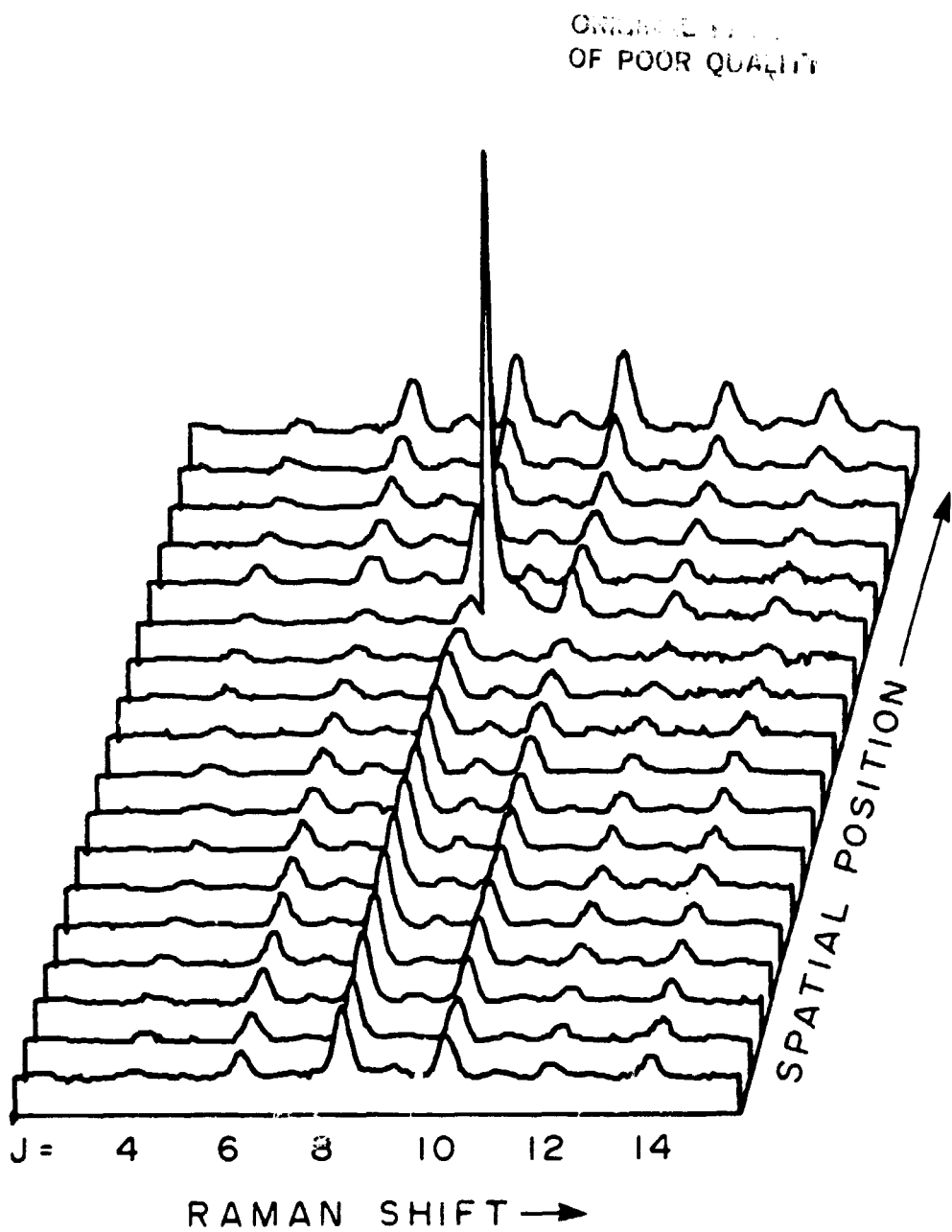


Fig. 8.1. Single-shot multipoint rotational CARS spectrum of room temperature  $N_2$ . The spatial resolution is 0.1 mm (1 pixel/track).

An example of a multishot spectrum of  $N_2$  is shown in Fig. 8.2, where there are a number of spikes caused by multiple laser pulses. This particular spectrum had a different scan format than usual in that each track represents 2 pixels, and hence  $\sim 0.2$  mm, in the interaction region. This spectrum clearly shows the decrease in the signal intensity at the edges of the interaction region, which is located mainly in the middle 10 tracks. As can be seen in comparing the two multipoint spectra, the overall signal-to-noise is substantially better in the multishot spectrum than in the single-shot spectrum.

The single-shot multipoint spectrum of  $O_2$  using the original scan format (i.e., 1 pixel/track) is presented in Fig. 8.3. The signal-to-noise in this spectrum is better than that in the single-shot  $N_2$  spectrum because the rotational Raman cross section for  $O_2$  is almost 3X greater than the cross section for  $N_2$  (Penney et al., 1974). A small nozzle was used to produce this flow, so the  $O_2$  concentration is greater in the center tracks. This is in contrast to Fig. 8.1 where a diffuse flow of  $N_2$  was used, so that the region of gas flow was much larger than the interaction volume probed.

### 8.3 Different Species Multipoint CARS

Different species were introduced simultaneously into the interaction region in order to determine the ability of the multipoint CARS technique to spatially resolve different volume elements along a line. This was accomplished by using a coflowing jet configuration consisting of a 1 mm diam nozzle surrounded by a coaxial honeycomb. This jet was positioned so that the nozzle gas was discharged into the center of the interaction region. The spectrum of the nozzle gas is expected to occur primarily in the central 10 tracks (corresponding to  $\sim 1$  mm in the interaction

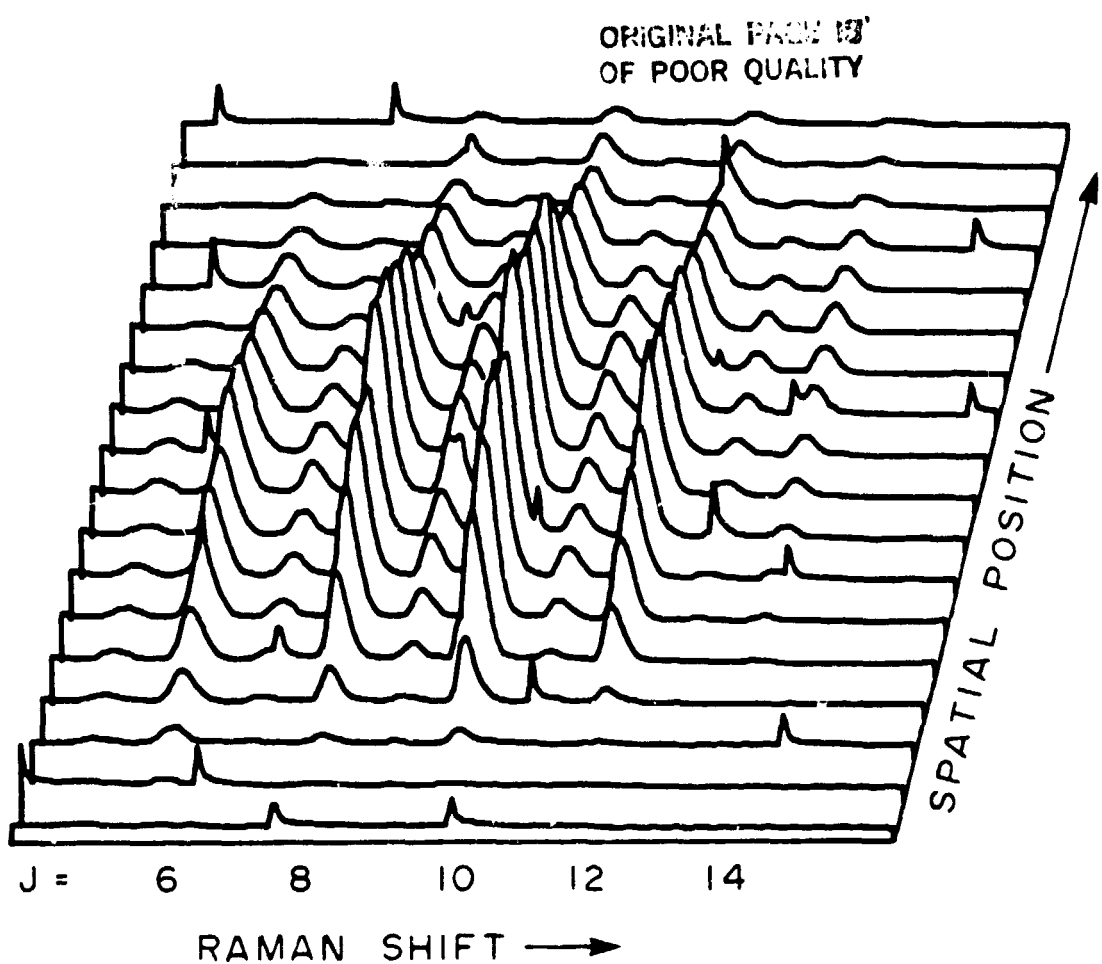


Fig. 8.2. Multishot multipoint rotational CARS spectrum of room temperature  $N_2$ . Spatial resolution is 0.2 mm (2 pixels/track). Asymmetric spikes are caused by multiple laser pulses.

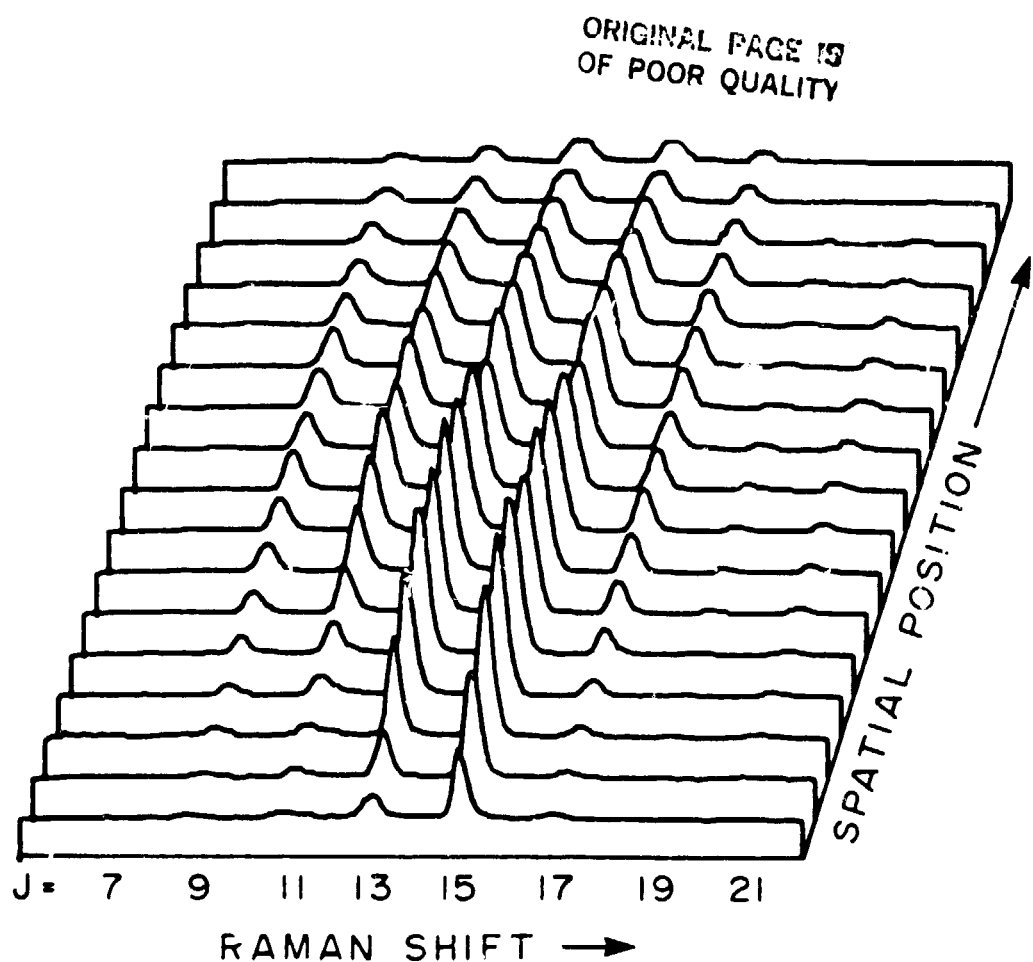


Fig. 8.3. Single-shot multipoint rotational CARS spectrum of room temperature  $O_2$ . Spatial resolution is 0.1 mm (1 pixel/track).

region). The spectrum of the coflowing gas should appear in the outermost tracks at either end. Several combinations of nozzle and coflowing gases were examined:  $N_2$  and  $O_2$ , which have a rotational spectrum occurring in the same frequency range, and Ar and  $CCl_2F_2$  (Freon-12) which have no spectrum in this range.

Fig. 8.4(a) shows the single-shot spectrum with  $N_2$  as the nozzle gas and Ar as the coflowing gas (i.e., Ar- $N_2$ -Ar). As expected, the  $N_2$  spectrum is primarily in the central tracks, indicating that the CARS signal is being generated from the 1 mm diam jet of  $N_2$  and the spatial integrity of the signal is preserved throughout the detection system. The reverse configuration,  $N_2$ -Ar- $N_2$ , with Ar as the nozzle gas is shown in Fig. 8.4(b). The central tracks show no spectrum while the intensity of the  $N_2$  spectrum gradually increases toward both ends.

The effect of a significant density gradient on the multipoint CARS spectrum was investigated by using the coflowing jet configuration with  $N_2$  and freon. The molecular weight of freon is  $\sim 4X$  that of  $N_2$ , while the weights of Ar and  $N_2$  are similar. It was thought that the density gradient might induce "phase-front" distortions in the input beams, leading to a greater phase-mismatch and a consequent reduction in the generated CARS signal. The freon- $N_2$ -freon spectrum and the complementary  $N_2$ -freon- $N_2$  spectrum are shown in Fig. 8.5. In Figs. 8.4(b) and 8.5(b) the topmost tracks correspond to the region of  $N_2$  which occurs before the input beams have passed through either the Ar jet or the freon jet. Although the relative intensities of the top and bottom tracks change from shot to shot, there is no consistent pattern of the lower tracks showing less intensity than the upper tracks. Similar results were found with  $O_2$ -freon- $O_2$ , shown in Fig. 8.6. We conclude that a density

ORIGINAL PAGE IS  
OF POOR QUALITY

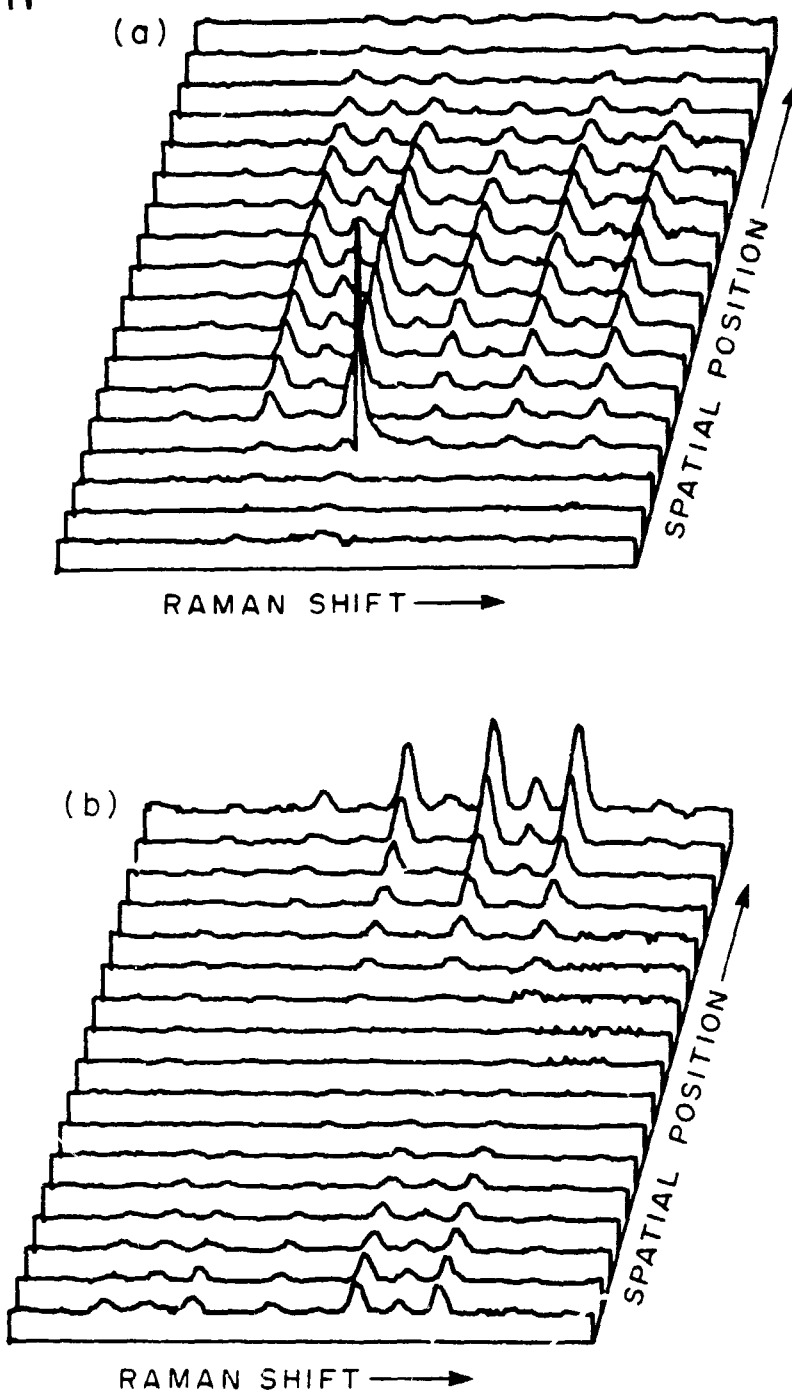


Fig. 8.4. Single-shot multipoint rotational CARS spectrum of (a) Ar-N<sub>2</sub>-Ar and (b) N<sub>2</sub>-Ar-N<sub>2</sub>. Spatial resolution is 0.1 mm.

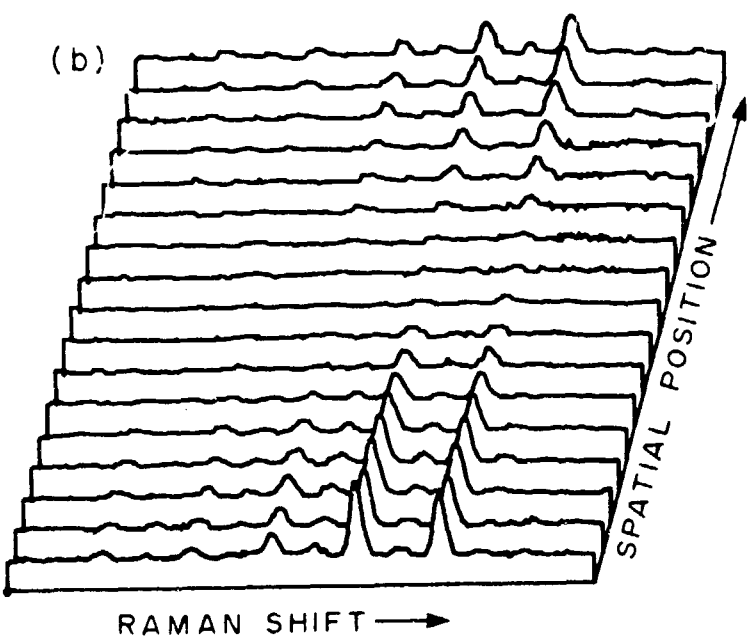
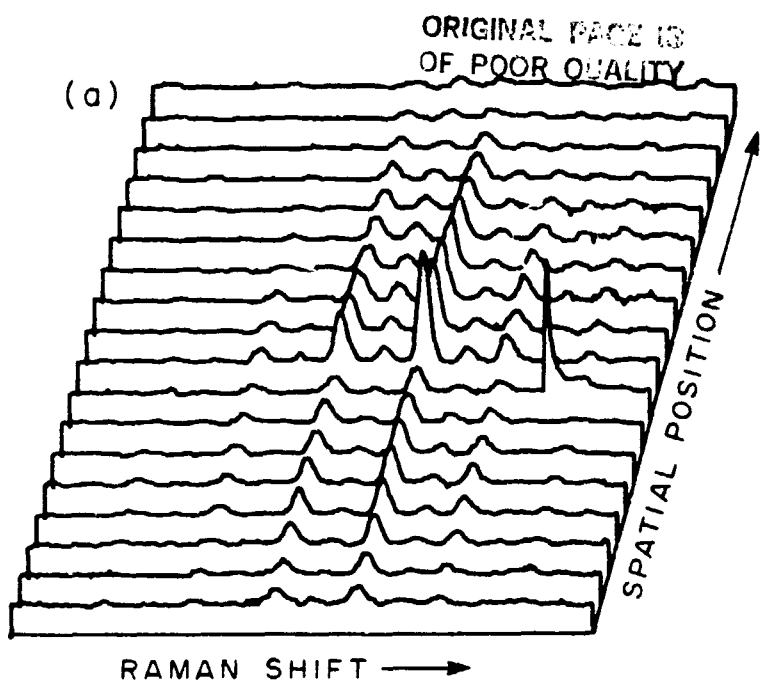


Fig. 8.5. Single-shot multipoint rotational CARS spectrum of (a) freon-N<sub>2</sub>-freon and (b) N<sub>2</sub>-freon-N<sub>2</sub>. Spatial resolution is 0.1 mm.

ORIGINAL PAGE IS  
OF POOR QUALITY

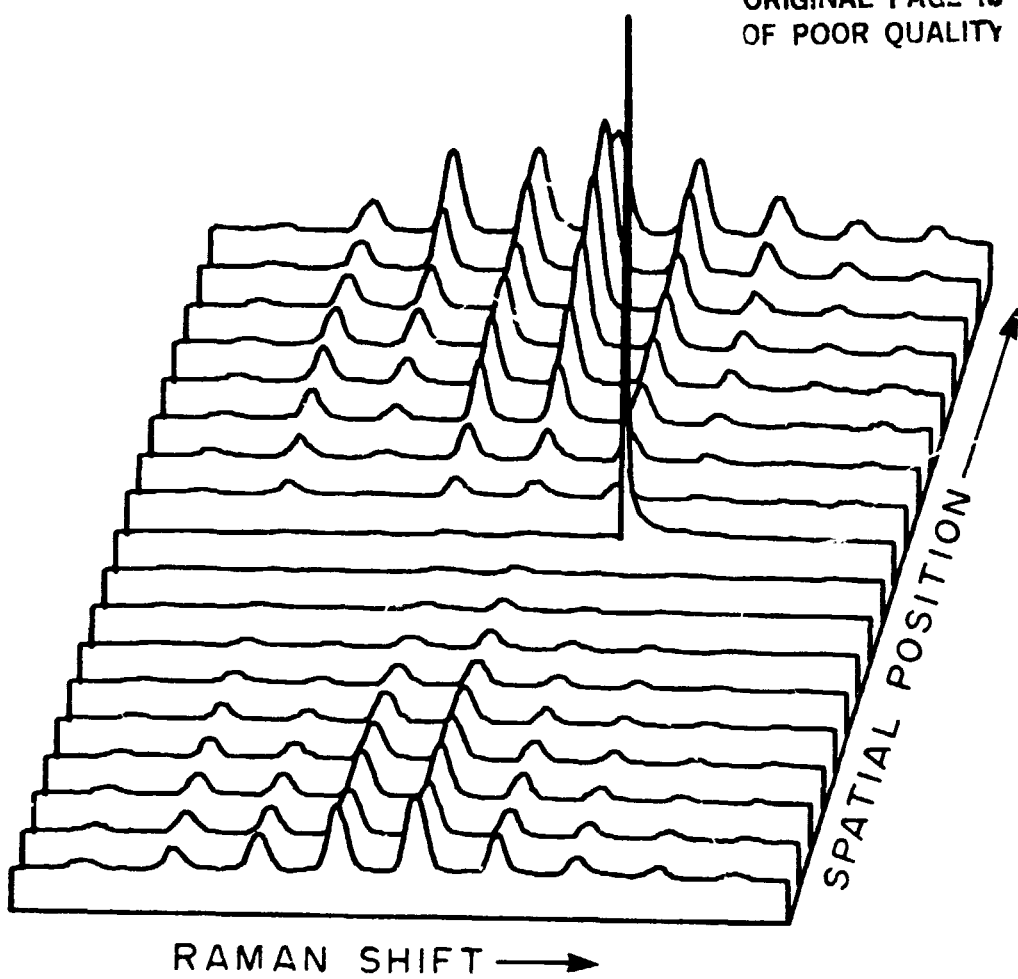


Fig. 8.6. Single-shot multipoint rotational CARS spectrum of O<sub>2</sub>-freon-O<sub>2</sub>.

gradient of this magnitude does not adversely affect the phase-matching in the multipoint CARS.

The final set of two species CARS experiments was done with  $N_2$  and  $O_2$  flowing from adjacent nozzles approximately 1 mm in diameter. The  $N_2-O_2$  spectrum is shown in Fig. 8.7(a). This spectrum used a scan format of 2 pixels/track so that the entire 20 tracks (18 are shown) represent ~4 mm in the sample region. There is no signal in the outer tracks since they represent regions outside the interaction volume. The  $O_2$  spectrum can be seen in the upper central tracks and the  $N_2$  spectrum is in the lower central tracks, with mixing clearly occurring for the tracks in between. The lower tracks (~1.), are expanded ~3X in Fig. 8.7(b), making the amplitude of the  $N_2$  comparable to that of the  $O_2$  peaks in Fig. 8.7(a). This is consistent with the fact that the Raman cross section for  $O_2$  is ~3X that for  $N_2$ .

#### 8.4 Different Temperature Multipoint CARS

The feasibility of using single-shot CARS for the instantaneous temperature determination of several volume elements along a line has been one of the goals of this research. The multipoint CARS of  $N_2$  at two different temperatures was obtained by using the coflowing jet configuration described in the previous section, with cold  $N_2$  as the nozzle gas and hot  $N_2$  as the coflowing gas. For the nozzle gas,  $N_2$  was cooled by flowing it through copper tubing immersed in liquid  $N_2$ . For the coflowing gas,  $N_2$  was heated by flowing it through copper tubing wrapped with heating tape. This was not an ideal arrangement since the jet apparatus was fabricated from metal, so that it was not possible to maintain a large temperature differential between the two gases. The visual difference between rotational spectrum is difficult to determine

ORIGINAL PAGE IS  
OF POOR QUALITY

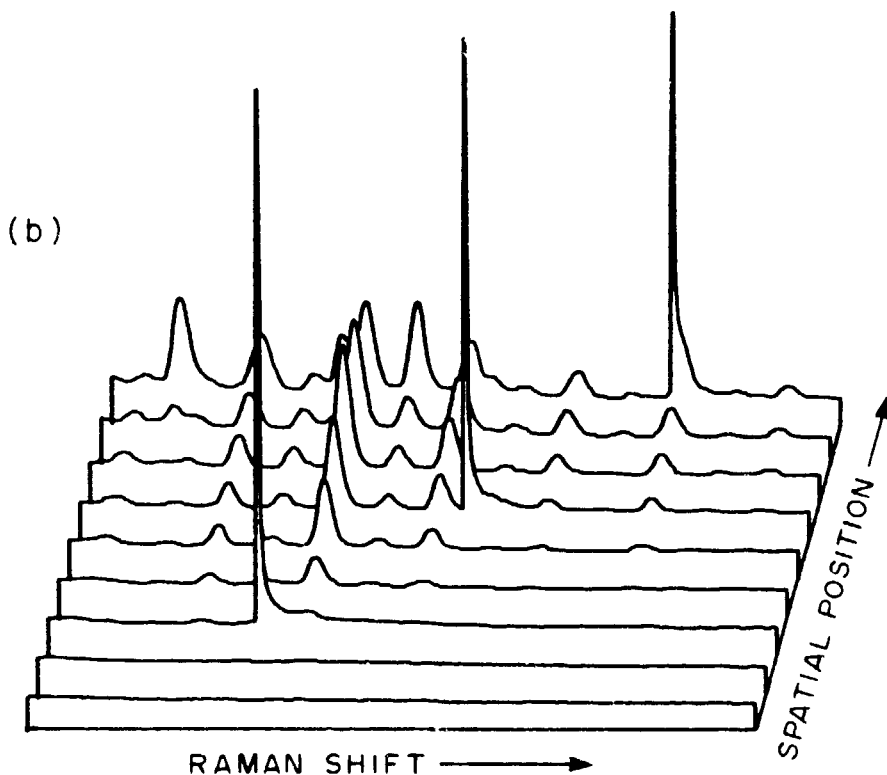
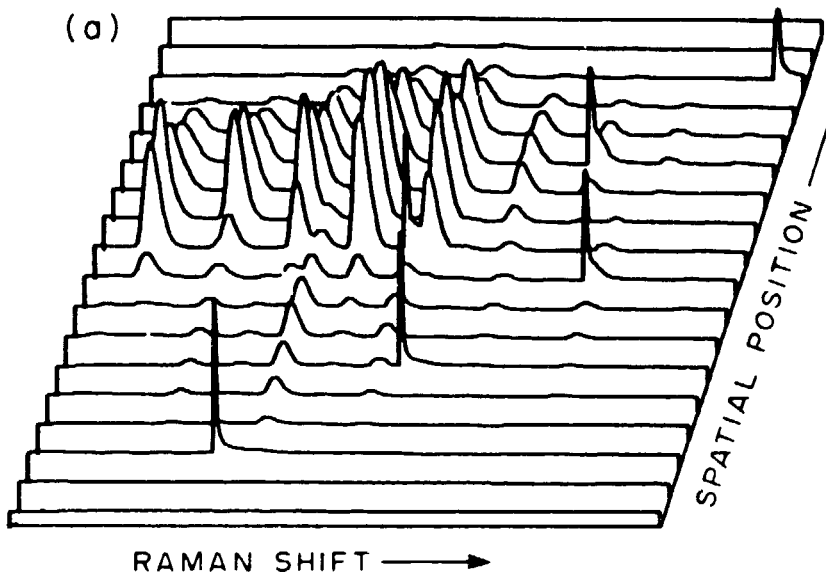


Fig. 8.7. Multishot multipoint rotational CARS spectrum of (a)  $N_2-O_2$  (18 tracks) with  $N_2$  in the lower central tracks and  $O_2$  in the upper central tracks. Spatial resolution is 0.2 mm. (b) The lower 9 tracks (mostly  $N_2$ ) expanded ~3X.

for temperatures that differ by less than 100-200 K. This difficulty is compounded in an unnormalized spectrum where both systematic and shot-to-shot intensity differences in the input beams influence the intensity distribution in the rotational lines tremendously. As demonstrated in the single-point CARS experiments, it is essential to have a reference leg to normalize a single-shot spectrum in order to even estimate a temperature.

With these considerations in mind, we wanted to demonstrate the multipoint single-shot CARS of N<sub>2</sub> at different temperatures. The hot N<sub>2</sub> gas flowing through the nozzle (no cold N<sub>2</sub>) is shown in Fig. 8.8(b). The cold N<sub>2</sub> flowing through the nozzle (no hot N<sub>2</sub>) is shown in Fig. 8.8(a). The differences in these unnormalized spectra are not particularly striking, but it can be seen that the spectrum of the hot N<sub>2</sub> is somewhat shifted to higher J numbers (larger Raman shift) as expected. The combination spectrum, with cold N<sub>2</sub> as the nozzle gas and hot N<sub>2</sub> as the coflowing gas is shown in Fig. 8.9. Although the spectrum is quite noisy and the signal in the outer tracks is relatively weak, it can be seen that the spectra for these outer tracks is shifted to higher J numbers relative to the spectra for the central tracks, indicating that the surrounding N<sub>2</sub> has a higher temperature than the nozzle gas. The relative spectral shift can be seen more clearly in Fig. 8.10, where successive tracks are aligned vertically. The spectrum of the warmer gas is also less intense because of the decrease in both the number density and the population difference factor. It is clear that normalization by a reference and a more substantial temperature gradient would produce a more dramatic multipoint single-shot CARS spectrum.

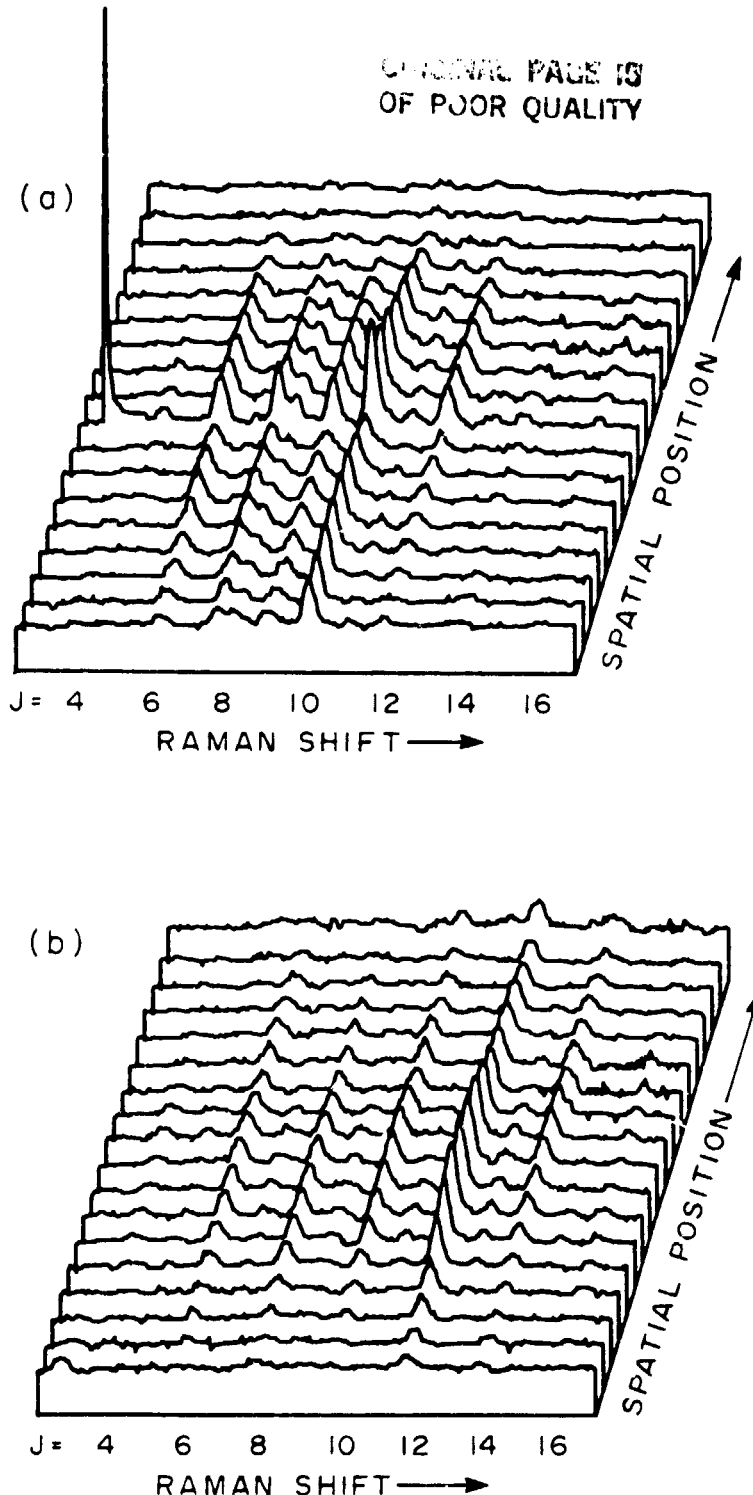


Fig. 8.8. Single-shot multipoint rotational CARS spectrum of (a) cold  $N_2$  and (b) hot  $N_2$ . Spatial resolution is 0.1 mm. Note that the intensity distribution in the hot  $N_2$  spectrum is shifted to higher J numbers (greater Raman shift).

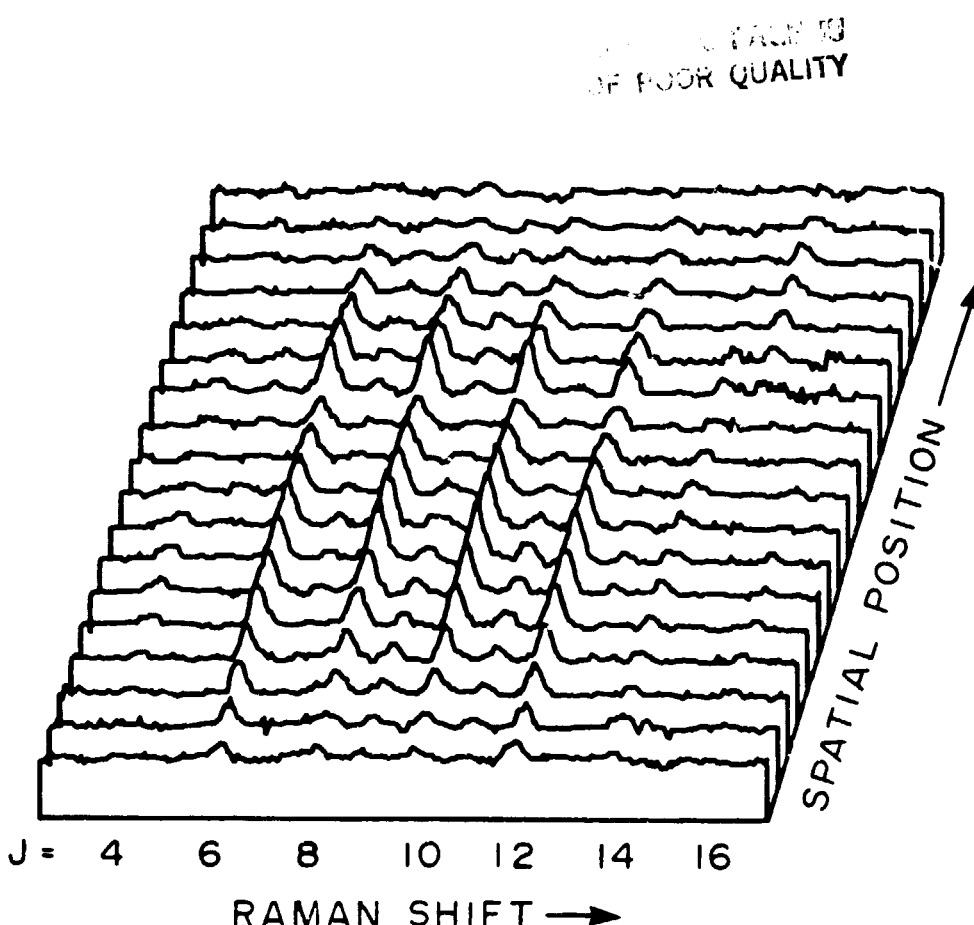


Fig. 8.9. Single-shot multipoint rotational CARS spectrum of hot N<sub>2</sub>-cold N<sub>2</sub>-hot N<sub>2</sub>. The intensity distribution in the outer tracks is slightly shifted to higher J numbers (greater Raman shift). Spatial resolution is 0.1 mm.

ORIGINAL PAGE IS  
OF POOR QUALITY

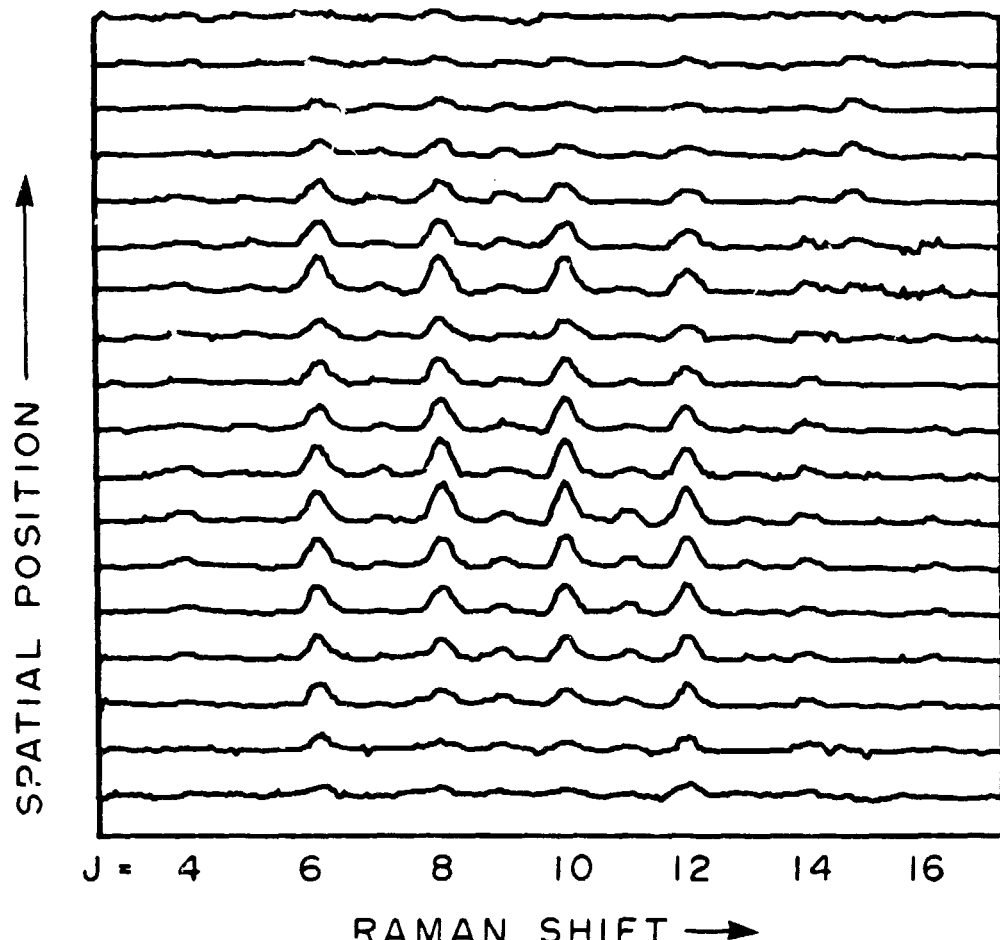


Fig. 8.10. Single-shot multipoint rotational CARS spectrum of hot N<sub>2</sub>-cold N<sub>2</sub>-hot N<sub>2</sub>. This is the same spectrum as shown in Fig. 8.9, but plotted with the peaks aligned vertically.

## 9. CONCLUSION

One of the initial objectives of this research was to investigate the use of CARS as a diagnostic technique for the determination of rotational temperatures. The results of the single-point experiments, presented in Section 5.1, indicate that CARS provides a means of accurately measuring the rotational temperature of  $N_2$  at room temperature and below. The good agreement between the CARS temperature and the thermocouple temperature suggests that the theory used to calculate the integrated intensity distributions is adequate for this application. The normalization of the single-shot spectrum was accomplished by using an identical reference at known temperature and pressure. However, this normalization scheme is applicable only when there is sufficient overlap of the sample and reference spectral distributions (i.e., when the temperature difference between the two systems is not too great). The most significant errors in the single-point measurements were introduced by the SIT vidicon detector. Many of these difficulties could be circumvented by the use of an improved detector such as an intensified photodiode array. The simultaneous determination of temperature and pressure, discussed in Section 5.1.7, requires the use of an iterative procedure because of the dependence of the signal amplitude on both temperature and pressure.

Although pure rotational CARS has been recognized as a means of temperature determination for temperatures below 1000 K, it has been assumed that rotational CARS has much smaller signal strengths than vibrational CARS at flame temperatures. We determined the relative signal strengths from  $N_2$  in a flame for the two techniques and found that the peak rotational CARS intensity was 1-2X the peak vibrational CARS intensity. The primary difficulty with the rotational CARS measurement was the

necessity of normalizing by a nonresonant reference. Because the flame temperatures are much higher (1600-1900 K) the sample spectrum cannot be normalized by an identical reference at room temperature. Nevertheless, if the problems associated with normalization are solved, pure rotational CARS is a viable technique for measuring temperatures in flames, and would be particularly advantageous for systems requiring the measurement of a large range of temperatures (77-1900 K) with the same experimental apparatus.

The ultimate objective of this research was to investigate the feasibility of using rotational CARS to determine instantaneous temperature and concentration from many spatially resolved points along a line intersecting a turbulent flow. The initial obstacle was the relatively small signal generated in the large-angle, three-dimensional phase-matching configuration. The interaction volume was  $\sim$ 30X less than that for the small-angle configuration, resulting in proportionately less generated signal in the large-angle case. In addition, one of the three input beams was focused to a sheet, rather than to a point, leading to a decrease in energy density of  $\sim$ 20X.

The multipoint CARS signal intensity was too weak to permit the acquisition of a multipoint spectrum in a single laser shot. Modifications in the dye laser provided a 40% increase in output energy. Refinements in the optical alignment procedure and optimization of the optical arrangement also led to increased CARS intensity. The most significant improvement in the experimental design was the addition of an image intensifier to the existing detection system. The new detection system, referred to as the II-SIT, consists of an image intensifier tube coupled to the SIT vidicon with a specially fabricated fiber optic rod. The response

characteristics of the SIT and of the II-SIT were investigated at different detector temperatures. For the detection of pulsed signals, there was no improvement in signal-to-noise at lower detector temperatures. The overall gain in signal intensity with the II-SIT was  $\sim$ 50.

With the resulting increase in magnitude of the CARS signal it was possible to obtain a multipoint spectrum, consisting of 20 spatially-resolved volume elements ( $0.1\text{ mm} \times 0.1\text{ mm} \times 0.1\text{ mm}$ ), in a single 10 ns laser shot. The CARS signal generated from  $\text{N}_2$  or  $\text{O}_2$  under these conditions is certainly intense enough to permit the determination of scalar parameters (temperature and/or concentration) in a turbulent flow. The spatial resolution with respect to position along the multipoint line is quite good; for the present system it is  $\sim$ 0.1 mm and could be improved with different imaging optics. The multipoint CARS experiments vividly demonstrate the presence or absence of different species at specified positions in the interaction volume, as was shown with the coflowing jet configuration using various combinations of  $\text{N}_2$ ,  $\text{O}_2$ , Ar, and freon. The greatest difficulty to overcome is the normalization of the single-shot multipoint spectrum. It is not clear that a single-point reference would provide accurate normalization of a multipoint sample. Even a multipoint reference, which would increase substantially the complexity of the experiment, may not compensate adequately for spatial inhomogeneities in the input beams.

The multipoint CARS technique has the potential for investigating more than 20 volume elements along a line. A more powerful laser could not improve the present experiment substantially since the present energy density is close to the breakdown level of the sample gases. However, more energetic input beams could be spread over a larger distance to

permit the acquisition of a greater number of volume elements. Since the two spherically focused beams (the Stokes beam and one of the pump beams) cross at a finite angle, at large distances it would become necessary to focus one of these with a cylindrical lens. The interaction volume would be determined by the intersection of one line and two sheets of radiation.

It is clear that the multipoint CARS technique can provide instantaneous, spatially-resolved information regarding scalar parameters in turbulent flows. At this point this information is qualitative, and at best, semiquantitative. If the difficulties associated with normalization of the signal and with distortions introduced by the detector can be surmounted, the multipoint CARS technique has the potential of acquiring single-shot spatially-resolved quantitative information as we

## LIST OF SYMBOLS

$A_J$	normalized integrated area of $J^{\text{th}}$ Raman line
$\alpha$	phase-matching angle
$\vec{\alpha}$	polarizability tensor
$\alpha_{ij}$	molecular electronic polarizability
$\partial\alpha/\partial q$	change in polarizability with nuclear coordinate
$\beta$	phase-matching angle
$\chi^{(1)}$	$i^{\text{th}}$ order susceptibility tensor of rank $(i + 1)$ .
$\chi^{(3)}$	third-order nonlinear susceptibility
$\chi_{\text{NR}}^{(3)}$	nonresonant $\chi^{(3)}$
$\chi_{\text{RAM}}^{(3)}$	Raman resonant $\chi^{(3)}$
$D$	degeneracy factor equal to 6, 3, or 1
$\Delta$	population difference factor
$\delta$	phase-matching angle
$\vec{E}(\vec{r}, t)$	electric field
$\epsilon(T)$	sum of squares error parameter for distributions of $A_J$
$F_J(P, T)$	ratio of CARS intensity of the sample and reference for the $J^{\text{th}}$ Raman line
$g_J$	nuclear spin weighting factor for $J^{\text{th}}$ Raman line
$\Gamma$	damping term; corresponding to $1/T$
$\Gamma_J$	Raman linewidth for $J^{\text{th}}$ line
$\Gamma_\ell$	laser linewidth
$\vec{k}_1, \vec{k}_2, \vec{k}_3, \vec{k}_4$	wave vector of indicated light wave
$\vec{k}_A, \vec{k}_{AS}$	wave vector of anti-Stokes radiation

LIST OF SYMBOLS (cont'd):

$\vec{k}_L$ , $\vec{k}'_L$	wave vector of pump radiation
$\vec{k}_S$	wave vector of Stokes radiation
$\Delta\vec{k}$	wave vector indicating phase-mismatch
$\vec{\chi}$	vector defining path of signal propagation
$l_{coh}$	coherence length
$l_{int}$	interaction length
$\mu$	mistuning frequency
N	molecular density
$n_i$	refractive index at $\lambda_i$
$\gamma$	phase-matching angle
$\gamma$	anisotropy of the molecular polarizability
$I(\omega)$	intensity at frequency $\omega$
$I_A(\omega_L + \theta)$	CARS intensity
$I_L(\omega_L)$	pump laser intensity
$I_S(\omega_L - \theta)$	Stokes laser intensity
$I_A^J(\omega_A)$	CARS power for the $J^{th}$ Raman line
J	rotational line representing $J \rightarrow J \pm 2$ transition
$\omega_1, \omega_2, \omega_3, \omega_4$	frequency of indicated light wave
$\omega_A, \omega_{AS}$	frequency of anti-Stokes radiation
$\omega_L, \omega'_L$	frequency of pump laser radiation
$\omega_R$	frequency of Raman shift
$\omega_S$	frequency of Stokes radiation
$\omega_{rov}$	transition frequency between rovibrational states
$\langle \omega_{AS} \rangle$	broadband anti-Stokes radiation
$\langle \omega_S \rangle$	broadband Stokes radiation

LIST OF SYMBOLS (cont'd):

$\vec{p}$	microscopic induced polarization
$\vec{P}(\vec{r}, t)$	macroscopic induced polarization
$p^{(3)}$	third-order polarization
$q$	normal coordinate for nuclear motion
$\partial\sigma/\partial\Omega$	Raman scattering cross section
$\theta$	frequency of Raman shift

## REFERENCES

- H.C. Anderson and B.S. Hudson, "Coherent Anti-Stokes Raman Scattering," Molecular Spectroscopy, Vol. 5, R.F. Barrow, D.A. Long, and J. Sheridan, eds. (The Chemical Society, London, 1978) p. 142.
- B. Attal, M. Pealat, and J.P. Taran, "CARS Diagnostics of Combustion," presented at the 18th Aerospace Sciences Meeting, Pasadena, 1980.
- J.J. Barrett, "Generation of Coherent Anti-Stokes Rotational Raman Radiation in Hydrogen Gas," Appl. Phys. Lett. 29, 722 (1976).
- I.R. Beattie, T.R. Gilson, and D.A. Greenhalgh, "Low Frequency Coherent Anti-Stokes Raman Spectroscopy of Air," Nature 276, 378 (1978).
- N. Bloembergen, Nonlinear Optics (W.A. Benjamin, Inc., New York, 1965).
- J.P. Boquillon and R. Bregier, "High-Resolution Coherent Stokes Raman Spectroscopy of the  $\nu_1$  and  $\nu_3$  Bands of Methane," Appl. Phys. 18, 195 (1979).
- L.A. Carreira, L.P. Goss, and T.B. Malloy, Jr., "Preresonance Enhancement of the Coherent Anti-Stokes Raman Spectra of Fluorescent Compounds," J. Chem. Phys. 69, 355 (1978).
- M.H. Crowell and E.F. Labuda, "The Silicon-Diode-Array Camera Tube," Photoelectronic Imaging Devices, Vol. 2, L.M. Biberman and S. Nudelman, eds. (Plenum Press, New York, 1971).
- S.A.J. Druet and J.-P.E. Taran, "CARS Spectroscopy," Progress in Quantum Electronics, Vol. 7, T.S. Moss and S. Stenholm, eds. (Pergamon, New York, 1981) p. 1.

- P.K. Dutta and T.G. Spiro, "Resonance CARS Line Shapes: Excited State Parameters for Flavin Adenine Dinucleotide," *J. Chem. Phys.* 69, 3119 (1978).
- A.C. Eckbreth, "BOXCARS: Crossed-Beam Phase-Matched CARS Generation in Gases," *Appl. Phys. Lett.* 32, 421 (1978).
- A.C. Eckbreth, R.J. Hall, and J.A. Shirley, "Investigations of Coherent Anti-Stokes Raman Spectroscopy (CARS) for Combustion Diagnostics," presented at the 17th Aerospace Sciences Meeting, New Orleans, 1979,
- A.C. Eckbreth and P.W. Schreiber, "Coherent Anti-Stokes Raman Spectroscopy (CARS): Application to Combustion and Gas Phase Diagnostics," Chemical Applications of Nonlinear Raman Spectroscopy, A.B. Harvey, ed. (Academic Press, New York, 1981).
- R.L. Farrow, P.L. Mattern, and L.A. Rahn, "Comparison between CARS and Corrected Thermocouple Temperature Measurements in a Diffusion Flame," *Appl. Opt.* 21, 3119 (1982).
- W.R. Fenner, H.A. Hyatt, J.M. Kellam, and S.P.S. Porto, "Raman Cross Section of some Simple Gases," *J. Opt. Soc. Am.* 63, 73 (1973).
- J.A. Giordmaine and W. Kaiser, "Light Scattering by Coherently Driven Lattice Vibrations," *Phys. Rev.* 144, 676 (1966).
- L.P. Goss, J.W. Fleming, and A.B. Harvey, "Pure Rotational Coherent Anti-Stokes Raman Scattering of Simple Gases," *Opt. Lett.* 5, 345 (1980).
- R.J. Hall and A.C. Eckbreth, "Coherent Anti-Stokes Raman Spectroscopy (CARS): Application to Combustion Diagnostics," Laser Applications, Vol. 5, R.F. Erf, ed. (Academic Press, New York, 1981).

- R.J. Hall, "Pressure-Broadened Linewidths for N<sub>2</sub> CARS Thermometry," Appl. Spectrosc. 34, 700 (1980).
- R. Igarashi, Y. Adachi, and S. Maeda, "Resonance CARS and CSRS Line Shapes of Ni(II)-Octaethylporphyrin," J. Chem. Phys. 72, 4308 (1980).
- T.C. James and W. Klemperer, "Line Intensities in the Raman Effect of <sup>1</sup>Σ Diatomic Molecules," J. Chem. Phys. 31, 130 (1959).
- K.S. Jammu, G.E. St. John, and H.L. Welsh, "Pressure-Broadening of the Rotational Raman Lines of some Simple Gases," Can. J. Phys. 44, 797 (1966).
- D. Klick, K.A. Marko, and L. Rimai, "Temperature and Concentration Measurements by CARS Spectroscopy in a Firing Single-Cylinder Engine," SAE Paper 810227, February 1981.
- I.I. Kondilenko, P.A. Koroktov, V.A. Klimenko, and N.G. Golubeva, "Absolute Raman Scattering Cross Sections of the Rotational Lines of Nitrogen and Oxygen," Opt. Spectrosc. 48, 411 (1980).
- Laser Raman Gas Diagnostics, M. Lapp and C.M. Penney, eds. (Plenum Press, New York, 1974).
- M. Maier, "Applications of Stimulated Raman Scattering," Appl. Phys. 11, 209 (1976).
- P.D. Maker and R.W. Terhune, "Study of Optical Effects Due to an Induced Polarization Third Order in the Electric Field Strength," Phys. Rev. 137, A801 (1965).
- D.V. Murphy and R.K. Chang, "Single-Pulse Broadband Rotational Coherent Anti-Stokes Raman Scattering Thermometry of Cold N<sub>2</sub> Gas," Opt. Lett. 6, 233 (1981).

- J.W. Nibler and G.V. Knighten, "Coherent Anti-Stokes Raman Spectroscopy," Raman Spectroscopy of Gases and Liquids, A. Weber, ed. (Springer-Verlag, Berlin, 1979).
- J.L. Oudar, R.W. Smith, and Y.R. Shen, "Polarization-Sensitive Coherent Anti-Stokes Raman Spectroscopy," Appl. Phys. Lett. 34, 758 (1979).
- J.-L. Oudar and Y.R. Shen, "Nonlinear Spectroscopy by Multiresonant Four-Wave Mixing," Phys. Rev. A 22, 1141 (1980).
- A. Owyong, "Coherent Raman Gain Spectroscopy Using cw Laser Sources," IEEE J. Quantum Electron. QE-14, 192 (1978).
- C.M. Penney, R.L. St. Peters, and M. Lapp, "Absolute Rotational Raman Cross Sections for N<sub>2</sub>, O<sub>2</sub>, and CO<sub>2</sub>," J. Opt. Soc. Am. 64, 712 (1974).
- Y. Prior, "Three-Dimensional Phase Matching in Four-Wave Mixing," Appl. Opt. 19, 1741 (1980).
- W.G. Rado, "The Nonlinear Third-Order Dielectric Susceptibility Coefficients of Gases and Optical Third-Harmonic Generation," Appl. Phys. Lett. 11, 123 (1967).
- L.A. Rahn, L.J. Zych, and P.L. Mattern, "Background-Free CARS Studies of Carbon Monoxide in a Flame," Opt. Commun. 30, 249 (1979).
- L.A. Rahn, A. Owyong, M.E. Coltrin, and M.L. Koszykowski, "The J Dependence of Nitrogen 'Q' Branch Linewidths," Proceedings of the 7th International Conference on Raman Spectroscopy, Ottawa, 1980.
- P.R. Regnier and J.-P.E. Taran, "On the Possibility of Measuring Gas Concentrations by Stimulated Anti-Stokes Scattering," Appl. Phys. Lett. 23, 240 (1973).
- W.B. Roh, P.W. Schreiber, and J.-P.E. Taran, "Single-Pulse Coherent Anti-Stokes Raman Scattering," Appl. Phys. Lett. 29, 174 (1976).

- R.L. St. Peters, "Augmented Coherent Anti-Stokes Raman Spectroscopy Linewidth Parameter from Laser-Mode Structure," *Opt. Lett.* 4, 401 (1979).
- R.L. St. Peters, "Gas Diagnostic Measurements by Coherent Anti-Stokes Raman Spectroscopy: Feasibility Calculations for Water Vapor in Combustion Systems," Final Report, Aeronautical Systems Division, Air Force Systems Command, Contract No. F33615-77-C-3112, 1980.
- J.A. Shirley, R.J. Hall, and A.C. Eckbreth, "Folded BOXCARS for Rotational Raman Studies," *Opt. Lett.* 5, 380 (1980).
- I.A. Stenhouse, D.R. Williams, J.B. Cole, and M.D. Swords, "CARS Measurements in an Internal Combustion Engine," *Appl. Opt.* 18, 3819 (1979).
- W.M. Tolles, J.W. Nibler, J.R. McDonald, and A.B. Harvey, "A Review of the Theory and Application of Coherent Anti-Stokes Raman Spectroscopy (CARS)," *Appl. Spectrosc.* 31, 253 (1977).
- A. Weber, "High Resolution Raman Studies of Gases," The Raman Effect, Vol. 2, A. Anderson, ed. (Marcel Dekker, Inc., New York, 1973).
- M.A. Yuratich, "Effects of Laser Linewidth on Coherent Anti-Stokes Raman Spectroscopy," *Mol. Phys.* 38, 625 (1979).